1-1-2011

Laser shadowgraphy measurement of abrasive particle mass, size and velocity distributions through micro-masks used in abrasive jet micro-machining

Damon Dehnadfar
Ryerson University

LASER SHADOWGRAPHY MEASUREMENT OF ABRASIVE PARTICLE MASS, SIZE AND VELOCITY DISTRIBUTIONS THROUGH MICRO-MASKS USED IN ABRASIVE JET MICRO-MACHINING

By

Damon Dehnadfar, B. Eng.

Tehran Azad University, Iran, 2004

A thesis

Presented to Ryerson University

In partial fulfillment of the requirements for the degree of

Master of Applied Science

In the program of

Mechanical Engineering

Toronto, Ontario, Canada, 2011

AUTHOR'S DECLARATION

I hereby declare that I am the sole author of this thesis

I authorize Ryerson University to lend this thesis to other institutions or individuals for the purpose of scholarly research.

I further authorize Ryerson University to reproduce this thesis by photocopying or by other means, in total or in part, at the request of other institutions or individuals for the purpose of scholarly research.

ABSTRACT

LASER SHADOWGRAPHY MEASUREMENT OF ABRASIVE PARTICLE MASS, SIZE AND VELOCITY DISTRIBUTIONS THROUGH MICRO-MASKS USED IN ABRASIVE JET MICRO-MACHINING

Master of Applied Science, Mechanical Engineering, 2011, Damon Dehnadfar

Ryerson University

In abrasive jet micromachining (AJM), a jet of particles is passed through narrow mask openings in order to define the features to be micro-machined. The size and shape of the micro-machined features depends on the distribution of the particle velocity and mass flux through the mask openings. In this work, a high speed laser shadowgraphy technique was used to demonstrate experimentally, for the first time, the significant effect of the mask opening size and powder shape and size on the resulting distribution of particle mass flux and velocity through the mask opening. In particular, it was found that the velocity through the mask was approximately constant, but different in magnitude than the velocity in the free jet incident to the mask. The measured mass flux distributions were in excellent agreement with a previously developed analytical model, thus directly confirming its validity. Additional measurements also showed that an existing numerical model could be used to predict the velocity distribution in free jets of spherical particles, and, if a modification to the particle drag coefficient is made, in free jets of angular particles. The direct experimental verification of these models allow for their use in surface evolution models that can predict the evolving shape of features micro-machined using AJM.

ACKNOWLEDGEMENTS

Foremost, I would like to express my sincere gratitude to my supervisors Dr. M. Papini and Dr. J. Friedman for the continuous support of my graduate study and research, for their guidance, motivation and immense knowledge.

Beside my supervisors, I owe my sincere gratitude to Chao Ma for his technical support and Joseph Amankrah for manufacturing parts of an important apparatus during the completion of the project.

Last but not the least, I would like to thank my parents, Maryam and Parviz, for supporting me spiritually throughout my life. My special gratitude is due to my sister, Damineh, for her support and friendship and encouragement.

I owe my loving thanks to my wife, Marjan, for her unconditional love and support. Without her encouragement and understanding, it would have been impossible for me to finish this work.

I gratefully acknowledge the financial support of the Natural Sciences and Engineering Research Council of Canada, (NSERC), and the Canada Research Chairs Program (CRC).

Damon Dehnadfar

TABLE OF CONTENTS

AUTHOR'S DECLARATION ii

ABSTRACT iii

ACKNOWLEDGEMENTS iv

TABLE OF CONTENTS v

LIST OF FIGURES viii

LIST OF TABLES xiii

NOMENCLATURE xiv

CHAPTER 1 1

Introduction 1

1.1 Motivation 1

1.2 Thesis Objective 3

CHAPTER 2 4

Literature review 4

2.1 Theoretical study of important parameters in abrasive jet machining 4

2.1.1 Effect of particle size in AJM 4

2.1.2 Effect of particle shape in AJM 5

2.1.3 Effect of nozzle geometry on velocity profile of free jet 7

2.2 Particle spatial distribution in jet 8

2.3 Particle velocity and its effect on erosion 11

2.3.1 Particle velocity distribution in jet 12

2.4 Effect of mask edge on the surface profile of features machined using AJM 17

2.5 Introduction to different methods of measuring the particle size distribution 19

2.5.1 Laser diffraction 20

2.5.2 Measurement using Image Analysis 21

2.6 Introduction to different methods of measuring the particle velocity 22

2.6.1 Double disc technique of Ruff and Ives 22

2.6.2 Laser Doppler Velocimetery (LDV) 24

2.6.3 Phase-Doppler Particle Analyzer (PDPA) 25

2.6.4 Particle Image Velocimeter (PIV) 26

2.6.5 Particle Tracking Velocimetery (PTV) 27

2.6.6 Shadow Imaging 28

CHAPTER 3 30

Experiments 30

3.1 Experimental Apparatus 30

3.2 Measurement of powder velocity, spatial and size distribution using 34

CHAPTER 4 40

Measurement of particle spatial, velocity and size distributions 40

4.1 Velocity distribution of abrasive particles 40

4.1.1 Velocity in Free Jet Incident to Mask and Comparison to Model of Li et al. [5] 40

4.1.2 Particle velocity distribution through the mask opening 49

4.2. Particle size distribution in the free jet 55

4.3 Particle size distribution within the mask opening 59

4.4 Particle mass distribution within the mask opening 65

4.4.1 Measured values 65

4.4.2 Comparison to model of Ghobeity et al. [6] 72

4.5 Limitations on applicability of results 74

CHAPTER 5 76

Summary, Contributions and Recommendations for Future Work 76

5.1 Summary and contributions 76

5.2 Recommendations for future work 78

Appendix A 80

Appendix B 93

Appendix C 94

References 100

LIST OF FIGURES

Figure 1.1: Schematic of AJM through the mask plates, showing the mask opening width, W, and the standoff distance from the nozzle tip, h. The relative size of W compared to h has been greatly exaggerated for clarity……………………………………………………………………………….….…2

Figure 2.1: Relative particle velocity versus relative particle size………………………….…………...5

Figure 2.2: Spatial distribution of abrasive particles with the standoff distance, h, from the substrate………………………………………………………………………………………….……..…..8

Figure 2.3: Definition of the parameters used by Ciampini et al. [19] to characterize spatial distribution of particles in a plane perpendicular to the jet centerline……………………………………………….....10

Figure 2.4: Measured velocity distribution of 25µm Al_2O_3 from nozzle axis at 200 kPa, 20mm from nozzle exit [3]……………………………………………………………………………………….......13

Figure 2.5: Structure of abrasive-air jet flow in free jet………………………………………………...15

Figure 2.6: Particle diameter histogram for 25 µm aluminum oxide powder measured using shadowgraphy ……………………………………………………………………………….….....19

Figure 2.7: Schematic diagram of PIV experimental setup…………………………………….……26

Figure 3.1: Experimental apparatus………………………………………………………………….30

Figure 3.2: Schematic of the mask holder…………………………………………………….….…..33

Figure 3.3: Setup for shadowgraphy experiments through masks. Plane on which measurements were made is indicated. For the free jet experiments, the setup was identical, but without the mask plates……………………………………………………………………………………….....….35

Figure 3.4: Typical shadowgraphy pictures of particles in flight: (a) 50µm aluminum oxide particles and (b) 50µm glass beads…………………………………………………………………………..…….36

Figure 3.5: Illustration of interrogation window for determination of particle velocities…………….…..37

Figure 4.1: Plot of 50 µm Glass Bead velocities across the jet at a 20 mm standoff from the nozzle tip. Star symbols indicate particle velocity measured using shadowgraphy. The dashed line indicates predicted velocity using original model of [5], and solid line indicates model of [5] incorporating eq. (4.1). The size of the averaging bins was 100 µm…………………………………………………………….….…41

Figure 4.2: Plot of 50 µm Chronital Stainless velocities across the jet at a 20 mm standoff from the nozzle tip. Star symbols indicate particle velocity measured using shadowgraphy. The dashed line indicates predicted velocity using original model of [5], and solid line indicates model of [5] incorporating eq. (4.1). The size of the averaging bins was 100 µm……………………………………………………...…42

Figure 4.3: Plot of velocities of 50 µm Crushed Glass (Experiment #3a) across the jet at a 20 mm standoff from the nozzle tip. Star symbols indicate particle velocity measured using shadowgraphy. The dashed line indicates predicted velocity using original model of [5], and solid line indicates model of [5] incorporating eq. (4.1). The size of the averaging bins was 100µm…………………………………………………………………………………………………..45

Figure 4.4: Plot of velocities of 50 µm Grittal Stainless Steels (Experiment #2a) across the jet at a 20 mm standoff from the nozzle tip. Star symbols indicate particle velocity measured using shadowgraphy. The dashed line indicates predicted velocity using original model of [5], and solid line indicates model of [5] incorporating eq. (4.1). The size of the averaging bins was 100µm………………………………...………………………………………………………..…..46

Figure 4.5: Plot of velocities of 50 µm Al_2O_3 (Experiment #6a) across the jet at a 20 mm standoff from the nozzle tip. Star symbols indicate particle velocity measured using shadowgraphy. The dashed line indicates predicted velocity using original model of [5], and solid line indicates model of [5] incorporating eq. (4.1). The size of the averaging bins was 100µm………………………………………………..……………………………………....47

Figure 4.6: Plot of velocities of 25 µm Al_2O_3 (Experiment #5a) across the jet at a 20 mm standoff from the nozzle tip. Star symbols indicate particle velocity measured using shadowgraphy. The dashed line indicates predicted velocity using original model of [5], and solid line indicates model of [5] incorporating eq. (4.1). The size of the averaging bins was 100µm…….………………………………………………………………………………….……48

Figure 4.7: Measured velocity distributions of 50 µm Chronital Stainless Steels in 500 µm Opening (Experiment #1b). A zero position indicates the center of the mask opening (Fig. 4.14). Error bars represent the sample standard deviations in a bin of 10 µm width……………………….……………50

Figure 4.8: Measured velocity distributions of 50 µm Grittal Stainless Steels in 500 µm Opening (Experiment #2b). A zero position indicates the center of the mask opening (Fig. 4.14). Error bars represent the sample standard deviations in a bin of 10 µm width……………………………………..51

Figure 4.9: Measured velocity distributions of 50 µm Glass bead in 600 µm Opening (Experiment #4b). A zero position indicates the center of the mask opening (Fig. 4.14). Error bars represent the sample standard deviations in a bin of 10 µm width…………………………………………………...…..52

Figure 4.10: Measured velocity distributions of 25 µm Aluminum Oxide in 500 µm Opening (Experiment #5b). A zero position indicates the center of the mask opening (Fig. 4.14). Error bars represent the sample standard deviations in a bin of 10 µm width…………………………………………………...53

Figure 4.11: Particle velocity vectors inside the mask opening showing that most of particles ricocheting from the mask edge have a much lower velocity than those passing straight through the mask. Experiment #5b with 100 images processed for clarity…………………………………………………………...54

Figure 4.12: Particle size distribution of spherical particles incident to the mask opening for (a) 50 µm glass beads; (b) 50 µm stainless steel beads; (c) 35 µm glass beads. X symbols indicate shadowgraphy measurements, and solid lines indicate least square best fits to a normal distribution. The size of the averaging bins was 2.5 µm…………………………………………………………………...……57

Figure 4.13: Equivalent spherical radius distribution of angular particles incident to the mask opening for: (a) 50 µm crushed glass; (b) 50 µm stainless steel grit ; (c) 25 µm aluminum oxide. X symbols indicate shadowgraphy measurements, and solid lines indicate least square best fits to a log-normal distribution. The size of the averaging bins was 2.5 µm……………………………………………………….….58

Figure 4.14: Schematic showing that smaller particles (*r1*) can pass closer to the mask edge than larger ones (*r2*)…………………………………………………………………………….……………..59

Figure 4.15: Particle size distribution measured in the mask for 50 µm Spherical Stainless Steels (Experiment #1b)..60

Figure 4.16: Particle size distribution measured in the mask for 50 µm Grittal Stainless Steels (Experiment #2b)...60

Figure 4.17: Particle size distribution measured in the mask for 50 µm Crushed Glass (Experiment #3b)...61

Figure 4.18: Particle size distribution measured in the mask for 50 µm Glass Bead (Experiment #4b)...61

Figure 4.19: Particle size distribution measured in the mask for 35 µm Glass Bead (Experiment #4c)...62

Figure 4.20: Particle size distribution measured in the mask for 25 µm Al_2O_3 (Experiment #5b)...62

Figure 4.21: Normalized particle size distribution inside the mask opening using 50µm spherical and non-spherical stainless steels. The plot symbols are the measured quantities. Only half the symmetrical mask opening width is shown. A zero position indicates the center of the mask opening (Fig. 4.14). Error bars represent the sample standard deviations……………………………………………………….……63

Figure 4.22: Normalized particle size distribution inside the mask opening using 50μm spherical and non-spherical Glass media. The plot symbols are the measured quantities. Only half the symmetrical mask opening width is shown. A zero position indicates the center of the mask opening (Fig. 4.14). Error bars represent the sample standard deviations……………………………………………………………….…64

Figure 4.23: Particle mass distribution inside the mask opening, using 50 μm glass beads. Lines are the predictions of eq. (5.2), using the normal size distributions in Fig. 4.12. The plot symbols are the measured quantities. Only half the symmetrical mask opening width is shown. A zero position indicates the center of the mask opening (Fig. 4.14). Error bars represent the sample standard deviations………………………………………………………………………….……………………66

Figure 4.24: Particle mass distribution inside the mask opening, using 50μm stainless steel beads. Lines are the predictions of eq. (5.2), using the normal size distributions in Fig. 4.12. The plot symbols are the measured quantities. Only half the symmetrical mask opening width is shown. A zero position indicates the center of the mask opening (Fig. 4.14). Error bars represent the sample standard deviations……………………………………………………………………………………………….67

Figure 4.25: Particle mass distribution inside the mask opening, using 35 μm glass beads. Lines are the predictions of eq. (5.2), using the normal size distributions in Fig. 4.12. The plot symbols are the measured quantities. Only half the symmetrical mask opening width is shown. A zero position indicates the center of the mask opening (Fig. 4.14). Error bars represent the sample standard deviations…………………………………………………………………………….……………68

Figure 4.26: Particle mass distribution inside the mask opening using 50 μm crushed glass. Lines are the predictions of eq. (5.2), using the log-normal size distributions in Fig. 4.13. The plot symbols are the measured quantities. Only half the symmetrical mask opening width is shown. A zero position indicates the center of the mask opening (Fig. 4.14). Error bars represent the sample standard deviations…………………………………………………………………………….………69

Figure 4.27: Particle mass distribution inside the mask opening using 50μm stainless steel grit. Lines are the predictions of eq. (5.2), using the log-normal size distributions in Fig. 4.13. The plot symbols are the measured quantities. Only half the symmetrical mask opening width is shown. A zero position indicates the center of the mask opening (Fig. 4.14). Error bars represent the sample standard deviations…………………………………………………………………………...…..70

Figure 4.28: Particle mass distribution inside the mask opening using 25μm aluminum oxide. Lines are the predictions of eq. (5.2), using the log-normal size distributions in Fig. 4.13. The plot symbols are the measured quantities. Only half the symmetrical mask opening width is shown. A zero position indicates the center of the mask opening (Fig. 4.14). Error bars represent the sample standard deviations…………………………………………………………………………..………...71

Figure A 1: Material safety data sheets (MSDS) for Aluminum Oxide type of A, SB, J, N and V provided by Comco Inc. typically used for 25μm Al_2O_3 80

Figure A 2: Material Material safety data sheets (MSDS) for Aluminum Oxide type of C or S provided by Comco Inc. Typically used for 50µm Al_2O_3 …………………...81

Figure A 3: Material safety data sheets (MSDS) for glass beads provided by Comco Inc……………….82

Figure A 4: Material safety data sheets (MSDS) for crushed glass provided by Comco Inc……………..83

Figure A 5: Material safety data sheets (MSDS) for Chronital stainless steels provided by Vulkan Blast Shot Technology……………………………………………………………………………………..84

Figure A 6 (continued): Material safety data sheets (MSDS) for Chronital stainless steels provided by Vulkan Blast Shot Technology………………………………………………………………….…...85

Figure A 7 (continued): Material safety data sheets (MSDS) for Chronital stainless steels provided by Vulkan Blast Shot Technology…………………………………………………………………….....86

Figure A 8 (continued): Material safety data sheets (MSDS) for Chronital stainless steels provided by Vulkan Blast Shot Technology…………………………………………………………………………87

Figure A 9 (continued): Material safety data sheets (MSDS) for Chronital stainless steels provided by Vulkan Blast Shot Technology…………………………………………………………………….....88

Figure A 10: Material safety data sheets (MSDS) for Grittal stainless steels provided by Vulkan Blast Shot Technology……………………………………………………………………………………..89

Figure A 11 (continued): Material safety data sheets (MSDS) for Grittal stainless steels provided by Vulkan Blast Shot Technology…………………………………………………………………………90

Figure A 12 (continued): Material safety data sheets (MSDS) for Grittal stainless steels provided by Vulkan Blast Shot Technology…………………………………………………………………….....91

Figure A 13 (continued): Material safety data sheets (MSDS) for Grittal stainless steels provided by Vulkan Blast Shot Technology…………………………………………………………………………92

LIST OF TABLES

Table 2.1: Effect of particle shape on mass loss. The erosion tests were carried out on 1018 steel. The erodent particles were spherical glass beads and angular SiC of four different diameter ranges between 250 and 600µm. The particle velocities were 20 and 60 m/s [10]……………….6

Table 2.2: Measured variation of particle velocity (extrapolated to nozzle tip) and gas velocity in a commercial erosion apparatus at different pressures [23]……………………………………...23

Table 3.1: Physical properties of abrasive particles. * Estimated………………………………..31

Table 3.2: Process parameters for measurements on free jets…………………………………...31

Table 3.3: Process parameters for measurements in mask openings…………………………….32

Table B 1: Lens performance specification for 12X Zoom used in shadowgraphy provided by Navitar Inc…………………………………………………………………………………….93

NOMENCLATURE

The definition of symbols in alphabetical order:

Symbol	Name	Unit
A_p	Particle surface area	[μm^2]
A_s	Surface area of a sphere with the same volume as the particle	[μm^2]
C_D	Particle drag coefficient	[non-dimensional]
d_N	Inner duameter of nozzle	[μm]
d_P	Mean particle diameter	[μm]
E	Erosion rate	[g/g], [-]
h	Standoff distance from the nozzle tip	[mm]
k	Velocity component	[non-dimensional]
l	Particle's major (longest) axis	[μm]
L	Separation distance	[mm]
L_N	Nozzle length	[mm]
L_s	Length of discretizing nozzle segment	[μm]
$M^*(r)$	Normalized distribution mass of particles through the mask opening	[non-dimensional]
n	Velocity exponent	[non-dimensional]
$P(r)$	Probability density function	[μm^{-1}]
r	Radial distance from the nozzle ceterline	[mm]
r_n	Nozzle radius	[μm]
R	Radius of the jet	[mm]
Re	Particle relative Reynolds number	[non-dimensional]
s	Axial ratio of the longest to the shortest axis of a particle *(l/t)*	[non-dimensional]
S	Linear displacement	[mm]
t	Particle's minor (shortest) axis	[μm]
U	Average particle velocity	[m/s]
v	Disk rotational velocity	[Rads/Sec]

V	Particle velocity	[m/s]
V_0	Maximum velocity of the incoming particle	[m/s]
V_1	Velocity at the periphery of the jet	[m/s]
Vr	Incoming particle velocity at any radial position of the jet	[m/s]
vp	Particle velocity at (x, y) position from the nozzle tip	[m/s]
vp_0	Particle velocity at the nozzle center line	[m/s]
vp_1	Particle velocity at the end point of the ith segment of the nozzle	[m/s]
$v_{A\text{-}x}$	Centre line velocity of air flow at an axial distance x from nozzle exit	[m/s]
vpi_{-1}	Particle velocity at the start point of the ith segment of the nozzle	[m/s]
W	Mask opening width	[μm]
x	Distance from nozzle exit in jet flow direction	[mm]
θ_A	Divergence angle of the nozzle	[Degrees], [Radians]
θ_p	Expansion angle of abrasive air jet flow	[Degrees], [Radians]
$\theta(r)$	Angle of exit with respect to the nozzle centerline	[Degrees], [Radians]
ρ_A	Air density at nozzle cross section	[$kg.m^{-3}$]
ρ_p	Density of abrasive particle	[$kg.m^{-3}$]
μ	Air viscosity at room temperature	[$kg.m^{-1}s^{-1}$]
β	Experimentally determined jet focus coefficient	[non-dimensional]
φ	Particle sphericity	[non-dimensional]
ψ	Angle with a uniform random number on the interval (0, 2π]	[Radians]

CHAPTER 1

Introduction

1.1. Motivation

Abrasive jet micromachining (AJM) utilizes a jet of high speed particles to mechanically etch features such as micro-channels and micro-holes into glass, metal or polymeric substrates for use in micro-fluidic, micro-electromechanical (MEMS), and opto-electronic device fabrication. The jet of high speed impacting particles is usually passed through very narrow openings in a patterned erosion-resistant micro-mask which protects the substrate against particle impacts, thus defining the features to be machined (Fig. 1.1). The presence of the mask introduces a 'mask edge' effect, i.e., a disturbance to the incoming particle mass flux that depends on the particle size distribution, since progressively smaller particles can pass through the mask opening as its edge is approached. The disturbance in flux and the distribution of particle velocities across the mask opening affect the size and shape of features machined using AJM; they are thus required as an input for analytical and computer models capable of predicting surface profile evolution [1-4].

There are very few previous studies of the velocity, size, and particle spatial distributions in free abrasive jets typical of those used in AJM, and there are no previous studies that measure these distributions through a narrow mask opening. Therefore, in order to predict the shape of the micro profiles, a clear understanding of the relationship between these parameters is required and this forms the objectives of this thesis.

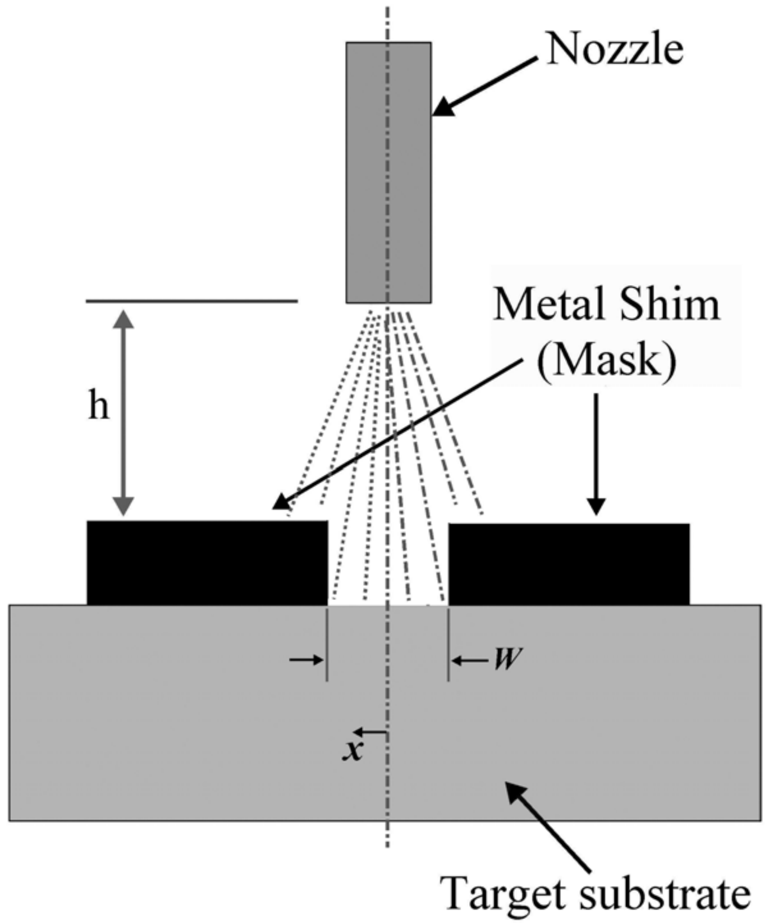

Figure 1.1: Schematic of AJM through the mask plates, showing the mask opening width, W, and the standoff distance from the nozzle tip, h. The relative size of W compared to h has been greatly exaggerated for clarity.

1.2. Thesis Objective

The objectives of the thesis are to:

- Determine the particle size, velocity and spatial distributions in the free jet incident to the mask opening. The effect of particle mean diameter, shape and drag coefficient on velocity will also be determined.

- Determine the effect of the mask edge on the particle velocity, size and mass distribution through the mask opening by changing important parameters such as particle size, shape and mask opening width.

- Evaluate the existing model of Ref. [5] for prediction of the particle velocities in free jets, and verify the fit of the experimental data with the analytical model prediction of Ref. [6] for the masked case.

CHAPTER 2

Literature Review

2.1 Theoretical study of important parameters in abrasive jet machining

Most erosion models assume that plastic deformation and target material removal occur due to the energy transferred by the mass and velocity of the particles. The more massive the particles, the higher the kinetic energy they carry, assuming an equal density and velocity. Therefore, the effects of specific parameters such as particle size, particle shape, nozzle geometry, different air pressures and flow rates on the velocity profile of the free jet are important to study.

2.1.1 Effect of particle size in AJM

One of the most important parameters in AJM processing technology is particle size. Many researchers reported that the erosion rate decreases sharply with decreasing particle size, and it may even become zero at some non zero threshold particle size. For instance, Dundar et al. [7] reported a significant change in the amount of superficial damage as the particle size decreases. They showed that increasing the particle size from 2 to 25 μm results in a significant increase in kinetic energy of about 2000 times. The corresponding increase in damage associated with the plastic deformation of the substrate falls with decreasing particle size. Moreover, the particle size distribution has a large impact on the particle velocities in AJM. In general, the particle velocity decreases with increasing particle size for a given air flow rate [8]. The rate of decrease was found to depend on the abilities of particles to rearrange within the flow, which, in turn, depends on the particle’s shape.

Prochasca et al. [8] analyzed the velocities of different sized particles within debris flows and reported that their velocities depended on the ability of individual particles to rearrange. Particle velocities decreased with increasing particle size as shown in Fig. 2.1[8].

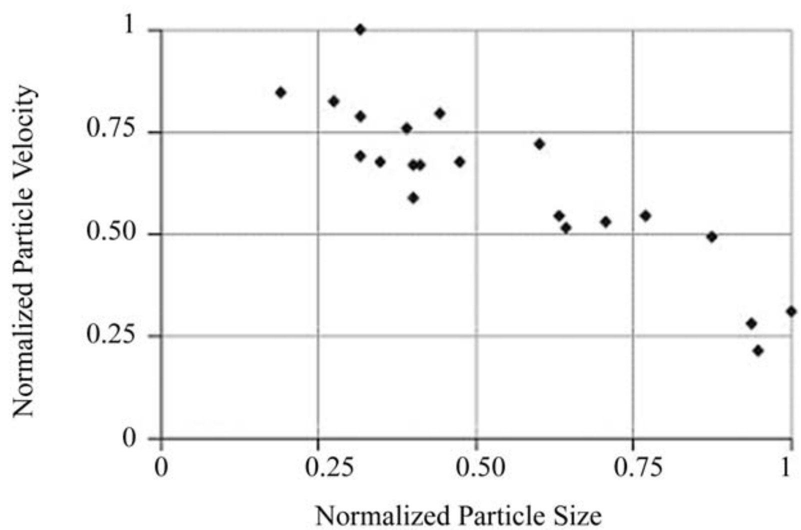

Figure 2.1: Normalized particle velocity versus normalized particle size [8]

2.1.2 Effect of particle shape in AJM

Most of the previous development of analytical models focused on particles with a spherical shape [5, 9]. However, it has been found experimentally that there is a large difference in the measured erosion rates between angular and spherical particles having a similar particle size. For example, Liebhard and Levy [10] studied the effect of the erodent particle shape on the mass loss for four different diameter ranges of both spherical and angular particles. The results showed that the shape of particles is a major factor in establishing their ability to erode materials. As shown in Table 2.1, angular particles of the same particle size ranges generally are more erosive than spherical particles.

Particle size (μm)	Feed rate (g min^{-1})	Mass loss (mg)			
		20 m s^{-1}		60 m s^{-1}	
		Spherical	Angular	Spherical	Angular
250–355	6.0	0.2	1.6	3.0	28.0
250–355	0.6	0.2	2.0	4.5	32.7
495–600	6.0	0.1	–	1.2	–
495–600	2.5	–	2.0	–	42.4

Table 2.1: Effect of particle shape on mass loss. The erosion tests were carried out on 1018 steel. The erodent particles were spherical glass beads and angular SiC of four different diameter ranges between 250 and 600μm. The particle velocities were 20 and 60 m/s [10]

Furthermore, many researchers have investigated the influence of particle shape on the drag coefficient and, consequently, the velocity evolution of particles in the air jet flow. There are many equations in the literature relating the drag coefficient C_D to the Reynolds number Re of spherical particles, e.g., Clift et al. [11], Khan and Richardson [12], and Haider [13]. However, not many generalized expressions for C_D vs. Re are available for non-spherical particles. Haider and Levenspiel [14] developed and presented such a correlation for non-spherical particles utilizing the concept of particle sphericity ϕ to account for particle shape. Equation (4.1) will demonstrate the relation between these parameters.

2.1.3 Effect of nozzle geometry on velocity profile of free jet

Various experimental results in the literature have described significant differences in the erosion rates of the same sample materials tested under nominally identical conditions in different apparatuses. In 1986, Ruff [15] found that the nozzle geometry affects the erosion conditions in the apparatus. Moreover, according to ASTM G-76 standard [16] the inner diameter of the nozzle needs to be measured periodically, and the nozzle should be replaced before the diameter has enlarged by 10%. The experimental investigation of Lapides and Levy [17] on the erosion of ductile metal samples showed that using an internally rough, rather than smooth–bored, nozzle in the test results in a smaller diameter of the primary eroded area on the substrate, all other conditions being the same. Shipway and Hutchings [18] also carried out a detailed examination of the influence of nozzle bore roughness on the erosion test conditions and noted that a rough nozzle bore is associated with a lower erodent velocity and a greater spread of velocities. They also found that the effects of nozzle geometry and internal roughness are more prominent for spherical particles than for angular particles, and it was proposed that this was due to differences in rebound behavior for the two types of particle. It is thus important to control not only the geometry of the nozzles but also the internal roughness in gas blast type apparatuses used in erosion testing.

2.2 Particle spatial distribution in jet

In an abrasive jet, the size of a particular jet cross-section varies with the standoff distance, *h*, reaching its maximum at the target surface. The spatial distribution of particles depends on a wide range of parameters including: nozzle geometry, dimensions, roughness, and particle shape and properties. Ciampini et al. [19] assumed that the particles travel outward in straight lines from the nozzle. Equation 2.1 introduced by Ciampini et al. describes the spatial distribution of particles exiting the nozzle at a distance *r* from the centerline:

$$\theta_r = \theta_A \frac{r}{r_n} \tag{2.1}$$

where θ_r is the angle of exit with respect to the nozzle centerline (Fig. 2.2). This equation implies that particles at the nozzle centerline leave on a path along the normal to the radial axis of the jet periphery, and particles on the outer edge of the nozzle leave at an angle equal to the divergence angle of the nozzle, θ_A.

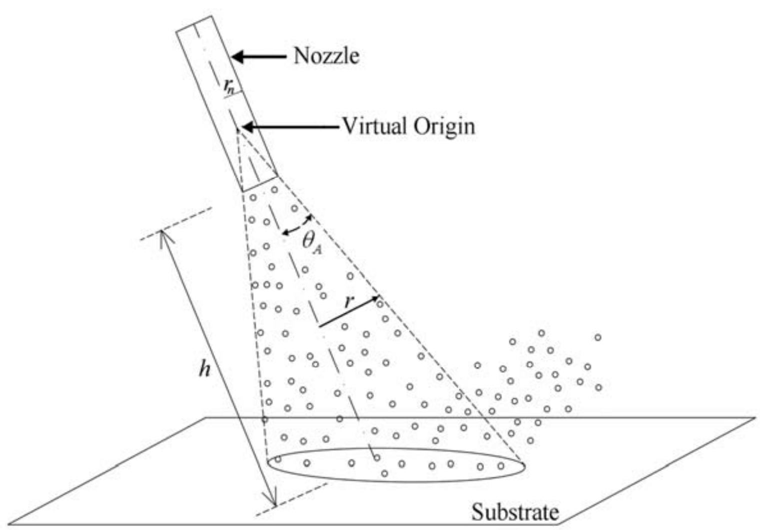

Figure 2.2: Spatial distribution of abrasive particles with the standoff distance, h, from the substrate.

Furthermore, Shipway and Hutchings [18] used rough nozzles in their erosion testing and reported that the particles were travelling at angles beyond a well-defined cone such as that shown in Fig. 2.2. However, it was also noted that the large majority of particles do travel within specific bounds of divergence for smooth nozzles. Thus, the simplified form of the stream divergence given in equation (2.1) may not be practical in all cases.

Li et al. [5] reported that the structure of the free particle flow is similar to the free pure air jet flow where there also exists a flow expansion. Apparently, the expansion angle θ_P of the particle flow is smaller than that of the air flow due to the larger density and momentum of the particles. Equation (2.2) presents the particle jet flow radius at an axial distance x with the expansion angle of particles assumed to be approximately $\theta_P = 7^{\circ}$ [5].

$$r_P = \frac{d_N}{2} + x \tan(\frac{\theta_P}{2}) \tag{2.2}$$

where:

θ_P : Expansion angle of abrasive particles in the air jet flow

d_N : Nozzle diameter

x: Distance from nozzle exit along the jet axis

The spatial distribution of particles within the jet emanating from a round nozzle was measured in Ref. [3], using a particle collection technique. In this technique, particles launched from the nozzle were collected at various radial distances, using a tungsten carbide cylinder connected to a nylon tube. Ghobeity et al. [3] compared two probability of particle mass flux distributions, the gamma and Weibull distributions, and chose the Weibull distribution function, *P(r)*, as the best fit to match the experimental data. It has been found that for the conditions encountered in AJM operations, the probability of a particle arriving at the target surface in a radial hoop between *r* and *r+dr* (Fig. 2.3) could be expressed as equation (2.3) with a scale parameter of $\frac{h}{\beta}$:

$$P(r)d_r = 2\left(\frac{\beta}{h}\right)^2 re^{-\left(\frac{\beta}{h}\right)^2 r^2} d_r \tag{2.3}$$

where *h is the s*tandoff distance from the nozzle tip and *β* is an experimentally determined jet focus coefficient.

In order to predict the surface evolution in AJM, Ciampini et al. [20] used the same probability distribution function of equation (2.3) in their simulation. The particles were considered in a plane which was perpendicular to the jet centerline and the angle *ψ* in Fig. 2.3 was assumed to be a uniform random number on the interval (0, 2*π*].

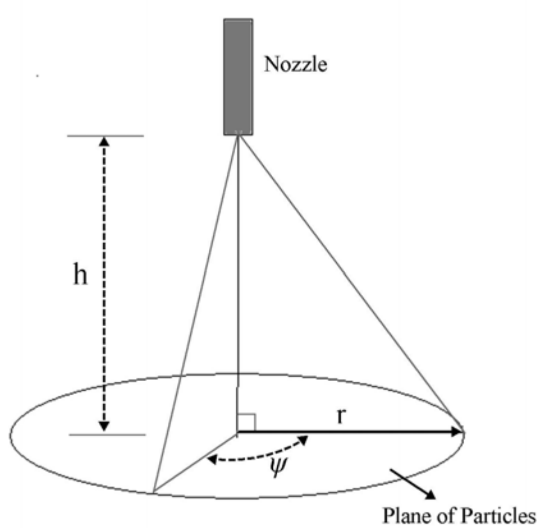

Figure 2.3: Definition of the parameters used by Ciampini et al. [20] to characterize spatial distribution of particles in a plane perpendicular to the jet centerline.

2.3 Particle velocity and its effect on erosion

Velocity is a critical test variable in erosion. It can easily overshadow changes in other variables such as target material, impact angle, etc. Most researchers use a power law to describe the effect of velocity on erosion rate, as follows

$$E = kV^n \tag{2.4}$$

where E is the erosion rate, V is the particle velocity, k is a constant, and n has values between 2 and 3.5 for metallic materials. Brittle materials tend to have a larger n range, from 2 to 6.5 [21]. Hence, the velocity exponent n was found to depend on the properties of the target material and the erodent particle, and it is usually governed by test conditions.

Balasubramaniam et al. [22] studied the effect of particle velocity in AJM. Comparison of the normalized erosion profiles for various jet centre line velocities showed that the particle velocity has a very strong influence on erosion rates of materials. For example, the normalized erosion profile at V_0 = 50 m/s appeared to be almost flat but it was much steeper at V_0 = 150 m/s. Therefore, the importance of an accurate knowledge of particle velocity is self evident.

2.3.1 Particle velocity distribution in jet

A considerable amount of experimental work to determine the particle velocities and distributions in particle-laden gas jets has been reported in the literature. For example, Stevenson and Hutchings [23] experimentally investigated the relationship between particle velocity and operating conditions in a gas blast system typically used in solid particle erosion testing. They employed two different methods to measure the exit velocities of the erodent particles: the double disc method of Ruff and Ives [24] and an opto-electronic method similar to that of Kosel and Anand [25]. Section 2.6 will discuss these different methods of measurement in detail. These studies, however, involved blasting on a larger scale, and there are relatively few studies of free jets for the relatively small nozzles, pressures and particles typically used in AJM systems.

Some researchers have shown that the particle velocity distribution across the jet is linear. For example, Ghobeity et al. [3] measured the velocity distribution of 25µm aluminum oxide across an abrasive jet using a round 0.76mm nozzle with the aid of a Phase-Doppler Particle Analyzer (PDPA) and inferred an approximately linearly decreasing velocity from the center to the periphery of the jet (Fig. 2.4).

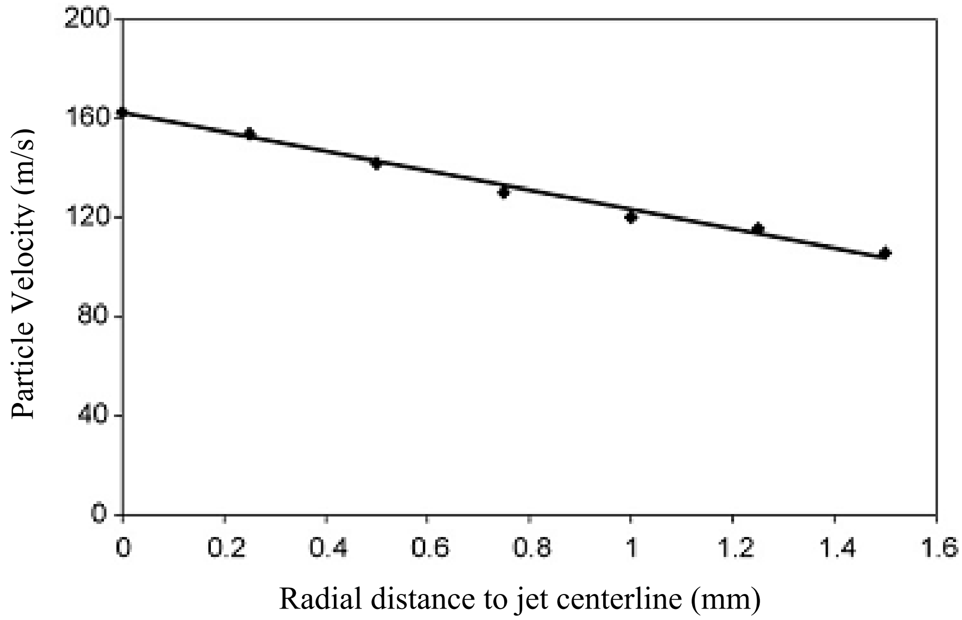

Figure 2.4: Measured velocity distribution of 25μm Al_2O_3 from nozzle axis at 200 kPa, 20mm from nozzle exit [3]

An earlier study by Balasubramania et al. [22] also showed a linear relation for velocity distribution of the particles as follows:

$$V_r = (V_1 - V_0)(r / R) + V_0 \qquad (2.5)$$

where:

V_0: the maximum velocity of the incoming particle

V_r: the velocity of the incoming particle at any radial position of the jet

V_1: the velocity at the periphery of the jet

R: the radius of the jet

r: The radius at any point with the jet

On the other hand, Burzynski and Papini [26] presented experimental techniques to measure the particle spatial and velocity distribution along the micro-abrasive jet and the result for velocity distribution demonstrated a linear or nonlinear velocity distribution depending on the particle type and the nozzle diameter. Achtsnick et al. [27] also developed a one dimensional isentropic flow model to calculate the particle exit velocity of each individual particle in the airflow for a converging cylindrical and a line shaped Laval-type nozzle. Particle velocity measurements using the particle image velocimetry (PIV) method showed a bell-shaped profile along the radial axis for the cylindrical nozzle. The velocity profile for the Laval nozzle showed a more uniform profile with a relatively flat bottom.

In the most recent work, Li et al. [5] developed a mathematical free jet model to determine the particle velocity at a given axial and radial location within an abrasive air jet flow typical of AJM. They found that their model had acceptable agreement with velocity measurements they performed using PIV. The model is such that the particle velocities at the nozzle exit are determined based on the nozzle length, particle mean diameter, particle density, air density and air flow velocity and particle drag coefficient. Fig. 2.5 showed the structure of abrasive-air jet flow in free jet. The distribution of particle velocities along the jet centerline downstream from the nozzle and the particle velocity profile at a jet cross-section were also modeled considering surrounding air entrainment and air-particle interaction.

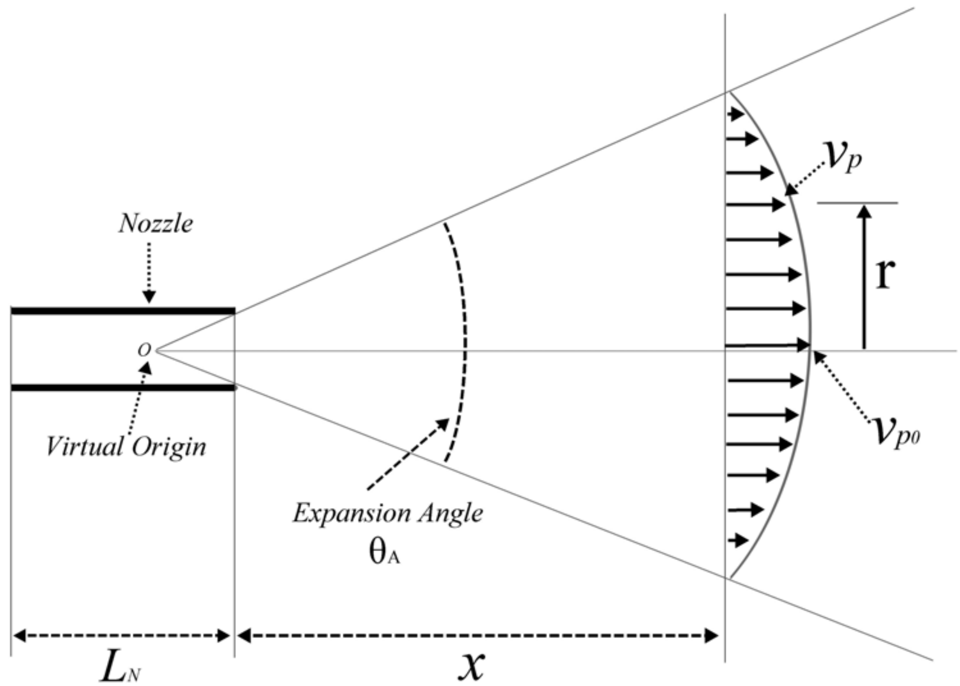

Figure 2.5: Structure of abrasive-air jet flow in free jet

In this model the axial distance from the nozzle exit downstream is separated into a series of identical segments with a length of L_S and the centerline particle velocity in the free jet was developed using

$$v_{Pi} = \left[v_{Pi-1}^2 \pm \frac{3}{2} \frac{L_S C_D \rho_A}{d_P \rho_P} \left(v_{A-x} - v_{Pi-1} \right)^2 \right]^{\frac{1}{2}} \qquad (2.6)$$

where:

v_{Pi} : Particle velocity at the end point of the ith segment of the nozzle

v_{Pi-1} : Particle velocity at the start point of the ith segment of the nozzle

L_s : Length of discretizing nozzle segment

C_D : Particle drag coefficient

ρ_A : Air density at nozzle cross section

d_P : Mean particle diameter

ρ_P : Density of abrasive particle

v_{A-x} : Centre line velocity of air flow at an axial distance x from nozzle exit

In order to use the equation (2.6), the velocity of air at the centerline of the free jet was compared with particle velocity at the same location of the ith segment. If the air velocity is greater than particle velocity, the air flow provides a dragging force to accelerate the particle. So, the positive sign is introduced in equation (2.6). However, the negative sign was used when the particle velocity became higher than the air velocity of the same segment.

Furthermore, Li et al. [5] also assumed a velocity distribution along the jet radial axis as

$$v_p = v_{p0} \exp\left[-\ln 2 \left(\frac{r}{\frac{d_N}{2} + 100 d_N \tan\frac{\theta_A}{2}} \right)^2 \right] \tag{2.7}$$

$$-r_P \le r \le r_P$$

where: $r_P = d_N / 2 + x \tan(\theta_P / 2)$

v_P : Particle velocity at (x, y) position from the nozzle tip

v_{P0}: Particle velocity at the nozzle center line with an axial distance x from nozzle exit

θ_P : Expansion angle of abrasive air jet flow

d_N : Nozzle diameter

x : Distance from nozzle exit in jet flow direction

The variation of particle flow velocity with radial distance, *r*, at different jet downstream sections can be calculated by using this method. Li et al.'s model predicts a Gaussian or bell shape velocity profile along the radial axis for different standoff distances from the nozzle tip, consistent with the model of [27].

2.4 *Effect of mask edge on the surface profile of features machined using AJM*

The size and shape of the micro-machined features depends on the distribution of the particle velocity and mass flux through the mask openings. However, the presence of the mask introduces a 'mask edge' effect. Several different approaches have been used to model this mask edge effect, but it has never been measured. For example, the analytical surface evolution model of ten Thjie Boonkkamp and Jansen [1] relates the instantaneous surface slope to the local brittle erosion rate through the normal velocity component. Their model approximates the disturbance to the incoming particle flux caused by particle collisions with the mask edge as a linear decrease in flux as the mask edge is approached. Slikkerveer and in't Veld [2] developed a similar surface evolution model but considered the particles to be infinitely small so that the mask edge effect was not considered. Ghobeity et al. [3] modified the model of ten Thjie Boonkkamp and Jansen [1], introducing a semi-empirical method that utilized the measurement of a shallow first pass profile to infer the mask edge effect. When incorporated in the surface evolution model of ten Thjie Boonkkamp and Jansen [1], this more accurate account of the decreased flux at the mask edge resulted in a better prediction of the etched feature depth and shape.

Ghobeity et al. [28] also developed a computer particle tracking simulation that modeled the ricochet and second strike of spherical particles off the edge of a hardened steel mask edge in order to estimate the effective particle mass flux through the mask opening. In a more recent work, Ghobeity et al. [6] developed an analytical model that was able to predict the mask edge effect as a function of particle size distribution (see Section 4.4.2). This model has also been recently adopted with good success by Burzynski and Papini [29] in their level-set based surface evolution model of AJM.

Yagyu and Tabata [30] developed a cellular automaton model for AJM that incorporated a mask. This model utilized a representation of particle flux that was similar to a continuum, rather than tracking individual particles, and therefore it could not model the effect of particle size distribution and particle-to-mask interaction effects. Ciampini et al. [20] presented an improved particle-tracking and cellular automaton-based approach that could simultaneously account for effects such as second-strike, spatial hindering, and particle size/edge effects. It provided greatly improved predictions of surface evolution, especially for high aspect ratio features.

2.5 Introduction to different methods of measuring the particle size distribution

The abrasive particles used in AJM are not all of the same size, and they usually vary in shape. Idealized solid particles have generally been described as spherical, rod or disk shaped. However, in order to simplify the measurement, the particles are usually assumed to be spherical [5, 6]. Since the particle size may vary over quite a wide range, it is normal to break the range up into different bin sizes, and measure the number of particles that are in each size bin to form a particle size distribution (PSD) that can be represented in the form of a histogram (Fig. 2.6).

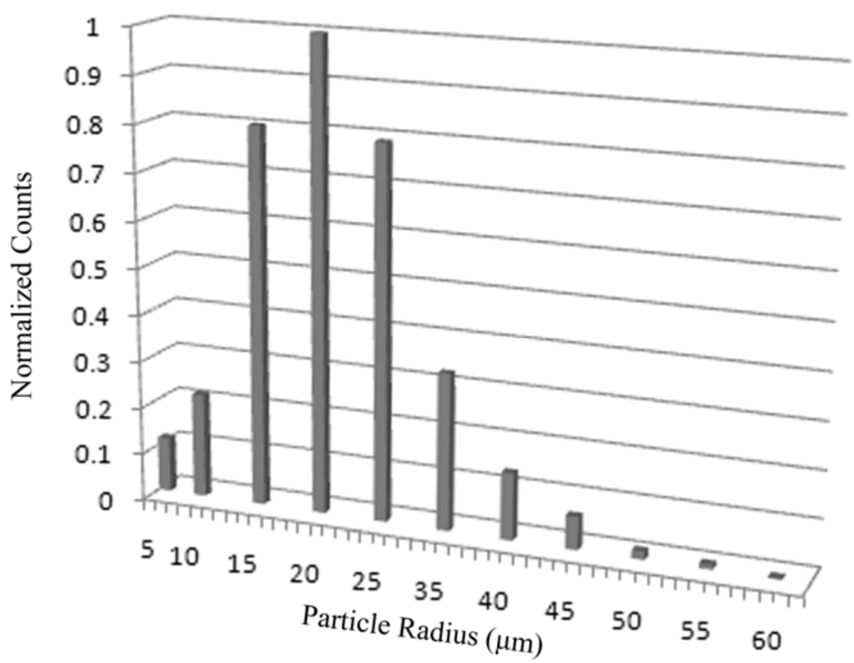

Figure 2.6: Particle diameter histogram for 25 μm aluminum oxide powder measured using shadowgraphy

Scientists and engineers have developed a number of different methods for particle size measurement in recent years, which will be now reviewed.

2.5.1 Laser diffraction

Laser diffraction is one of the most widely used techniques to analyze the particle sizes in many applications including manufacturing, quality control and product development. This method is a preferred method in industry since it can continuously measure a wide range of particle sizes. In this method, the particles passing through a laser beam scatter light at an angle that is correlated to their size. The laser diffraction particle size analyzer measures the particle sizes by multiple light detectors and the number of detectors increases the sensitivity and size limits of this method [31]. This method has been used by many researchers to investigate the size of particles having various shapes. Kippax [32] has reviewed some of the advantages of using laser diffraction for particle sizing including repeatability, ease of verification, and speed of measurement.

Traditional methods such as laser diffraction, although highly efficient, give limited information on particle shape. Image analysis may thus be a better tool for performing particle analysis.

2.5.2 Measurement using Image Analysis

In industry, it is sometimes necessary to also characterize particle shape in addition to particle size, to gain a better understanding of how shape can affect the various properties of a product. Visual inspection (microscopy or image analysis) is the most straightforward measurement technique and is increasingly being recognized as one of the most reliable techniques to characterize particle shape, size and volume distribution.

Visual-based systems use an automated image analysis solution that combines particle characterization software with an automated microscope and high resolution camera. Before the analysis begins, particles need to be placed on a motorized stage for inspection. To extract the needed data and related statistical results from the software, a pre-established or custom designed image analysis routine executes a list of procedures to the images. A standard routine includes three distinct categories of instructions: image acquisition, processing, and measurement [33].

The image analysis method can be combined with a scanning electron microscope (SEM) to perform small particle analysis. This method has been used in many works since it is an easy and straight forward measurement. For example, Ghobeity et al. [6] used a commercial optical particle sizing system to characterize the abrasive powders and measure important parameters such as particle mean size, standard deviation, aspect ratio and the equivalent spherical diameter. The size distribution results of their experiments confirmed the accuracy and repeatability of this method for various range of aluminum oxide sizes.

2.6 *Introduction to different methods of measuring the particle velocity*

Studies of erosive wear by solid particle impingement require a measurement of particle velocity and sometimes the angle of incidence. The most important methods used for particle velocimetry will now be reviewed.

2.6.1 *Double disc technique of Ruff and Ives*

In 1975, Ruff and Ives introduced a method to measure the particle velocity that consists of a pair of metal disks (A and B) mounted on an ordinary shaft and caused to rotate in front of the gas-particle jet. A single radial slot in disk B allows particles to pass through the opening and leave a mark on disk A. A pair of erosion scars is produced on disk A, one with the disks at a standstill and the other while the disks is rotating with a known and constant velocity [24].

Measurement of the angular displacement between those marks determines the time-of-flight of the particles as they cross the space between the disks. The average velocity over the distance can be determined using:

$$U = \frac{2\pi r v L}{S} \tag{2.8}$$

where L is the separation distance between two disks, U is the average particle velocity, v is the disk rotational velocity and S is a linear displacement of the two marks at a radius r from the disk center.

Ruff and Ives [24] applied this method of particle velocity measurement to three different erosion testing apparatus with satisfactory results. One of the apparatuses was a commercial air-abrasive jet device that feeds the abrasive particles through a flexible tube passing through a 0.5 mm nozzle diameter. They measured the particle velocity values from a particular nozzle design for different gas pressures at 3.5 cm standoff from the nozzle tip and reported the particle velocity increases by increasing the gas pressure. In addition, they repeated their measurements for different working distances at 310 kPa gas pressure and showed that the particle velocity decreases with increasing distance from the nozzle tip [24]. It was also noted by Ruff and Ives that the difference between the measured gas and particle velocities is about a factor of 3. Table 2.2 demonstrated the variance and changes in particle and gas velocities for three ranges of gas pressures. The particle velocity measurements using equation (2.8) were found to have a precision of about 10%.

Gas pressure (psig)	Gas pressure (kPa)	Gas velocity (m/s)	Particle velocity (m/s)
25	170	245	71
35	240	305	80
45	310	370	88

Table 2.2: Measured variation of particle velocity (extrapolated to nozzle tip) and gas velocity in a commercial erosion apparatus at different pressures [24]

2.6.2 Laser Doppler velocimetery (LDV)

A technique for obtaining spatial resolution within LDV measurement volumes was developed by Czarske [34] and subsequently improved by Czarske et al [35]. The LDV technique has the potential for a wide range of measurements at high spatial resolutions. This technique can be used to measure a given component of velocity by passing the particles through the intersection of two collimated and coherent laser beams [40]. The interference of two beams generates a set of straight fringes at the focal point of the laser beam. Thus, the particles passing through the fringes reflect light into a photo detector and, consequently, the velocity can be calculated from the frequency of signals receiving at the detector. Argon ion and helium-neon lasers are the most common light sources that can be used in LDV. To enhance the capabilities of LDV for multi-position measurements, sub-measurement volume position resolution techniques have been developed [34-39].It should be noted that velocity measurements using this method require other expensive equipment including a photo detector and an optical arrangement for laser beam splitting and focusing.

Lowe and Simpson [40] developed an advanced LDV measurement technique to determine the particle position and velocity within a turbulent flow. They extend the basic LDV method to obtain three dimensional particle velocities with respect to their position in the air flow. This new method of LDV enabled researchers to obtain better estimates of particle velocities near the boundary layer in a variety of flows with relatively high Reynolds numbers.

2.6.3 Phase-Doppler Particle Analyzer (PDPA)

The phase Doppler method is based on the principles of laser induced light scattering interferometry. Measurements are made at a small, non-intrusive optical probe volume defined by the intersection of two laser beams, similar to LDV. As a particle passes through the probe volume, the light is split from the beams and projected onto several detectors. The phase shift between the Doppler burst signals from different detectors is proportional to the size of the spherical particles. The phase Doppler particle analyzer (PDPA) method provides an accurate and reliable flow velocity and particle size data over a broad range of measurement situations.

In contrast to LDV, PDPA measurements are not based upon the scattered light intensity. The method thus does not suffer from typical errors of beam attenuation or deflection that can occur in higher dense particle flows. Moreover, Lee and Liu [41] noted that this method requires no calibration since the measurements are dependent only on the laser wavelength and optical configuration. However, the phase Droppler method is limited to spherical particles and it does not work for non-uniform geometries.

Ghobeity et al. [3] used the PDPA method to measure the particle velocity in a typical abrasive jet. The measurements made on particles passing through an ellipsoidal measurement volume and determined the actual particle velocities with components parallel and normal to the jet axis. The result of this measurements showed a linear velocity distribution across the jet and the comparison with the earlier measurement by Ref. [42] confirm the validity and reliability of the method.

2.6.4 Particle Image Velocimetery (PIV)

The development of particle Image Velocimetry (PIV)technique, which allows measurement of the velocity information of the whole flow field in fractions of a second, began in the 1980's. [43].

In a PIV system, a laser generates a thin light sheet inside the air-particle flow. With a pulsed laser, a high speed camera acquires two consecutive images of the particles in flight (Fig. 2.7). With the known laser pulse duration and the calibrated scaling factor of the camera, the particle velocity can be calculated by analyzing the pairs of images. The method has been used by many and has proven to give accurate measurements of particle velocity [5].

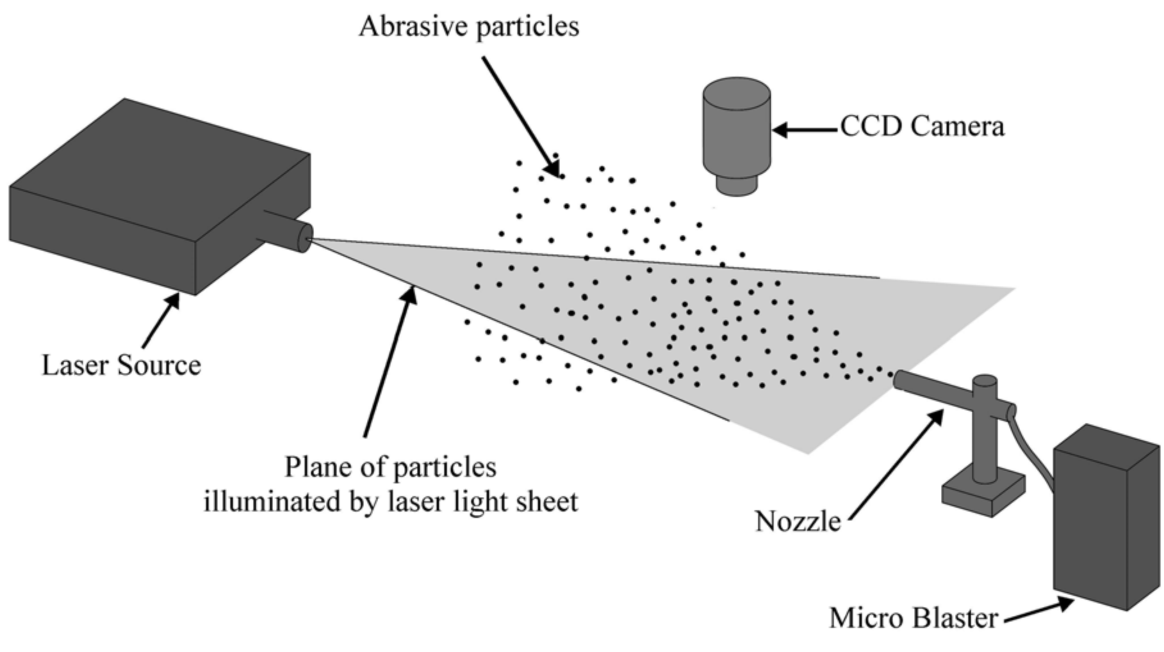

Figure 2.7: Schematic diagram of PIV experimental setup

For example, Li et al. [5] used the PIV method for two different nozzle sizes under different air pressures to compare their models with particle velocity measurements in the abrasive-air free jet experiments. They reported that the model predicted velocities and the corresponding experimental results are in good agreement with less than 4% average error. For instance, a statistical analysis showed that for a 0.36 mm nozzle, the average percentage deviation of the calculated velocity from the corresponding experimental data was 2.11% with a standard deviation of 3.62 m/s.

2.6.5 Particle Tracking Velocimetery (PTV)

Particle tracking velocimetry (PTV) is a direct descendent of flow visualization using tracer particles in fluid flows. Here, the particles are illuminated by two successive bursts of a laser beam, each particle producing two images on the same piece of film, similar to in the PIV method. However, PTV performs better than PIV when the particle density is relatively low in the flow, i.e., when the inter-particle distance is large compared to the displacement of the same particle between exposures. Under this condition, the probability that two neighboring images belong to the same particle is higher, and this will avoid any ambiguity on matching pairs of particles [44].

In contrast to PIV, PTV does not compute any vector in the empty space and the velocity vector is not computed unless a valid particle is located that area. Consequently, the uncertainty of the obtained particle velocity vector in the air jet flow by the PTV method is lower than for the PIV method.

Burzynski and Papini [26] also used the PTV method to assess the validity of their measurements, and it was reported that, for the majority of cases, their presented technique matched the PTV results quite well.

2.6.6 Shadow Imaging

Many industrial processes such as waste water treatment or electrochemical processes deal with gas bubbles. For the design and optimization of the equipment, it is important to study the influence of the gas bubbles on the fluid flow and mass transport in a quantitative way. A typical method for such measurements is backlighting or shadowgraphy where the bubble is illuminated by a diffuse light source and its shadow is imaged.

For instance, Sathe et al. [45] reported measurement of the shape, size, velocity and acceleration of bubbles using shadowgraphy. Measurements were performed in a narrow rectangular column at moderate gas hold-up (5%) with a wide variation of bubble sizes (0.1–15mm). Since the shadowgraphy technique is independent of the shape and material (either transparent or opaque), it can be also used to measure the particle size and velocity distribution in the abrasive jets used in AJM technology.

The technique is based on high resolution imaging with pulsed backlight illumination with a laser diffuser attached to the light source. Essentially, the particles in the focal plane block the light incident to the camera and thus appear dark against the light background of the source. Using a double-pulse light source and a double-frame camera, it is possible to evaluate the velocities of the individual particles. In contrast to PIV, the shadowgraphy method gives simultaneous information about particle velocity distribution and the particle size data [46].

The shadowgraphy method was used in this thesis to measure the particle size and velocity of various particles in a free jet and through masks used in AJM. Section 3.2 describes the utilized shadowgraphy setup in more in detail.

CHAPTER 3

Experiments

This chapter describes the experimental apparatus and methodology used to measure the velocity, spatial and size distribution of abrasive powders in both free jet and masked cases.

3.1. Experimental Apparatus

Shadowgraphy measurements of particle velocity, size, and spatial distribution were performed on both free jets and on particles passing through mask openings, using the setup shown in Fig. 3.1. All experiments were performed using an Accuflo (Comco Inc., Burbank, CA, USA) micro-abrasive blaster with a round 0.76 mm inner diameter nozzle (high performance nozzle MB1520-11, Comco Inc., Burbank, CA, USA), at various blasting pressures. For the free jet experiments, the measurements were taken at a 20 mm distance from the nozzle exit.

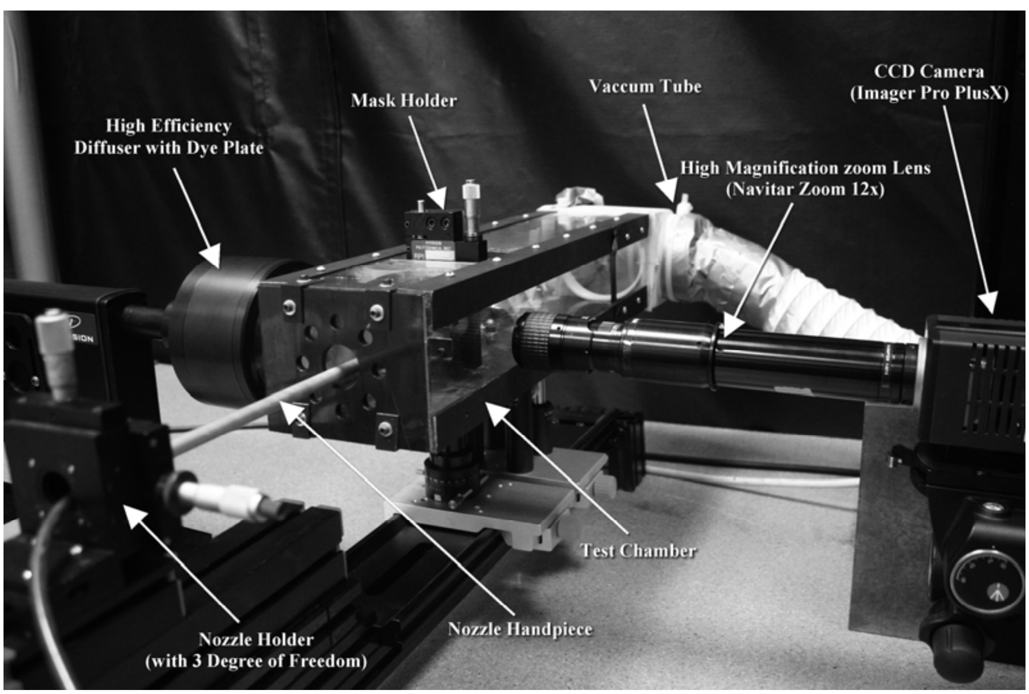

Figure 3.1: Experimental apparatus

A commercial optical particle sizing system (Clemex PS3 Research System, Clemex Technologies Inc., Longueuil, Quebec, Canada) was used to characterize the sphericity of the powders from shadowgraphy images. The properties of the utilized abrasive particles and the abrasive jet process parameters are provided in Tables 3.1, 3.2 and 3.3.

Material	**Manufacturer Name (Shape)**	**Average Sphericity**	**Manufacturer**	**Particle Size Quoted by Manufacturer (μm)**	**Average Particle Size(μm) Measured by Shadowgraphy**	**Density (kg m^{-3})**
Soda-Lime-Glass	Glass Bead (Spherical)	~1*	Comco Inc., USA	35	34	1600
				50	55	
Crushed Soda-Lime-Glass	Crushed Glass (Angular)	0.8	Comco Inc., USA	50	44	2500
Stainless Steels	Chronital Steel (Spherical)	~1*	Vulkan-INOX, Germany	50	54	7800
	Grittal Steels (Angular)	0.85		50	57	
Aluminum Oxide	Powder (Angular)	0.76	Comco Inc., USA	25	24	3800
		0.78		50	47	

Table 3.1: Physical properties of abrasive particles. * Estimated. (Appendix A)

Experiments	**#1a**	**#2a**	**#3a**	**#4a**	**#5a**	**#6a**
Abrasive Media	Stainless Steel		Soda-Lime Silica Glass	Glass Oxide	Aluminum Oxide	
Particle Shape	Spherical	Angular	Angular	Spherical	Angular	Angular
Abrasive Media nominal diameter as provided by manufacturer (μm)	50	50	50	50	25	50
Nozzle inner Diameter (mm)	0.76	0.76	0.76	0.76	0.76	0.76
Nozzle Length (mm)	10	10	10	10	10	10
Blasting Pressure (kPa)	300	300	250	250	300	300

Table 3.2: Process parameters for measurements on free jets

Experiments	**#1b**	**#2b**	**#3b**	**#4b**	**#4c**	**#5b**
Abrasive Media	Stainless Steel		Soda-Lime Silica Glass	Glass Oxide		Aluminum Oxide
Particle Shape	Spherical	Angular	Angular	Spherical		Angular
Abrasive Media nominal diameter as provided by manufacturer (µm)	50	50	50	50	35	25
Mask opening width (µm)	500	500	600	600	500	500
Thickness of the Mask (µm)	910	910	910	910	910	910
Blasting Pressure (kPa)	300	300	250	250	250	300

Table 3.3: Process parameters for measurements in mask openings

As shown in Fig. 3.1, in order to protect the shadowgraphy equipment from dust, the nozzle was placed inside a clear test chamber, open on one end, and with a vacuum tube fed to a dust collector on the other end. The vacuum was sufficiently weak, and the distance from the measurement area sufficiently large, that the measurements were not affected by its presence. For the measurements through the mask openings, two 0.91 mm thick hardened steel strips of the type typically used in AJM experiments [3, 4] were placed at prescribed distances apart and parallel to each other, in order to define the mask opening. The steel strips were milled to give sharp 90° edges to sharply define the unmasked region. The masks were clamped to the mask holder shown in Fig. 3.2, which consisted of a steel support attached to a linear stage, allowing for the mask opening to be set with a precision of 2.5 µm. The mask holder had a rectangular opening allowing for a line of sight into the region between the mask edges.

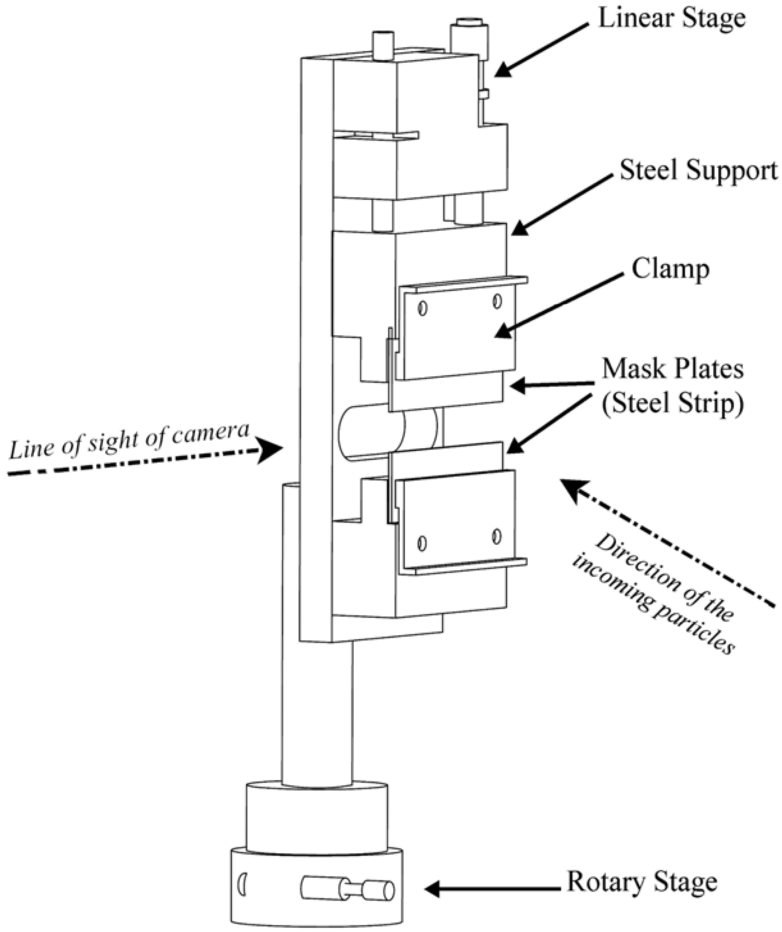

Figure 3.2: Schematic of the mask holder

The nozzle was installed on a series of linear stages with 3 degrees of freedom that allowed precise alignment of the nozzle centerline to the mask opening in micron scale, and varying the nozzle to mask stand-off distance. The rotary stage at the bottom of the mask holder had a rotation range of 360° and a resolution of 1 arcmin, allowing for varying the angle of incidence of the nozzle with respect to the mask. The nozzle was always oriented such that the particle jet was incident perpendicular to the mask opening at a constant standoff distance of 20 mm in this work.

3.2. Measurement of powder velocity, spatial and size distribution using shadowgraphy

Shadowgraphy measurements of particle velocity, spatial and size distribution were performed using a double pulsed frequency-doubled Nd: YAG (neodymium: yttrium aluminum garnet) laser, producing up to 0.3 joules/pulse pair, for a repetition rate of 1000 Hz, which was passed through a high efficiency diffuser (diffuser with dye plate, Item No.: 1108417, Lavision GmbH, Goettingen, Germany), and placed directly opposite a high speed CCD camera (Imager Pro PlusX, Lavision GmbH, Goettingen, Germany) with a high magnification zoom lens (Navitar zoom 12x, Navitar Inc., Rochester, New York, USA), as shown in Fig. 3.1. Resolution of the camera was 1600x1200 pixels with the pixel size of 7.4x7.4 μm^2. The abrasive jet was incident in a plane parallel to the camera lens. The optics of the camera were such that the depth of focus defined the plane of particles on which the measurement were made. Using the highest lens magnification for the masked cases, the depth of focus was 0.05 mm within the mask opening, and this value was slightly larger due to the lower magnification of the lens in the free jet case (Appendix B). This focal plane was aligned to the centerline of the abrasive jet, so that measurements were made on a plane of particles across the jet (free jet measurements) or mask opening width (measurements through mask), as indicated in Fig. 3.3.

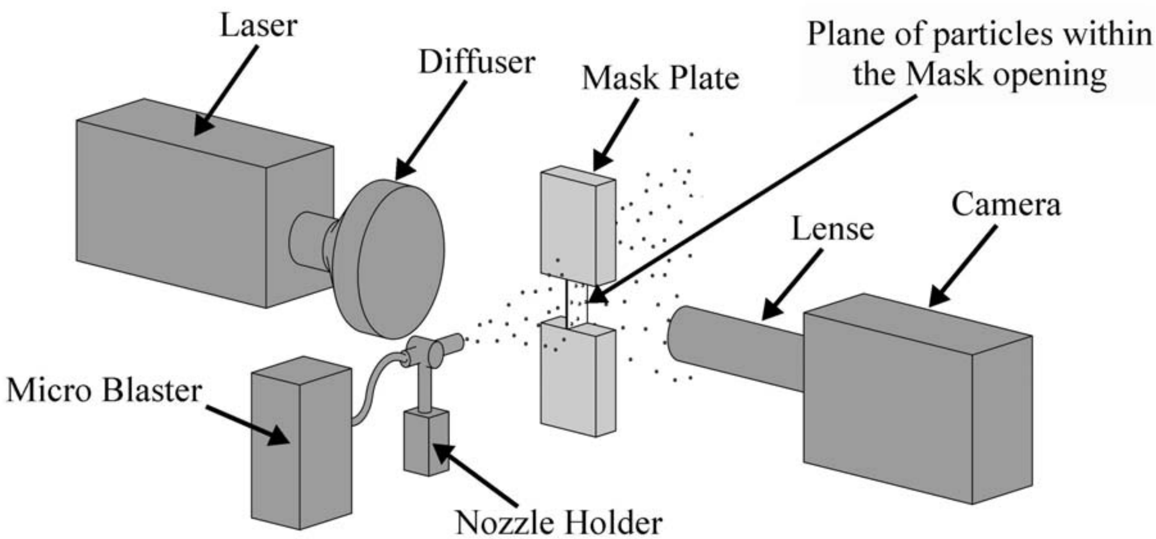

Figure 3.3: Setup for shadowgraphy experiments through masks. Plane on which measurements were made is indicated. For the free jet experiments, the setup was identical, but without the mask plates.

In this configuration, the particles in the focal plane blocked the light incident to the camera, and thus appeared dark against the light background of the source, as shown, for example, in Fig. 3.4. The laser was capable of producing two pulses of 1 ns duration, so that two successive images of the particles in flight could be obtained by the double-frame CCD camera which was synchronized to the laser pulses. Depending on the flow velocity and the factor of magnification of the camera lens, the delay between the two pulses was chosen to be between 1 to 3 μs. Computer software (Davis software, Lavision GmbH, Goettingen, Germany) was used to process and analyze the images and subsequently evaluate the sizes and velocities of the individual particles.

(a)

(b)

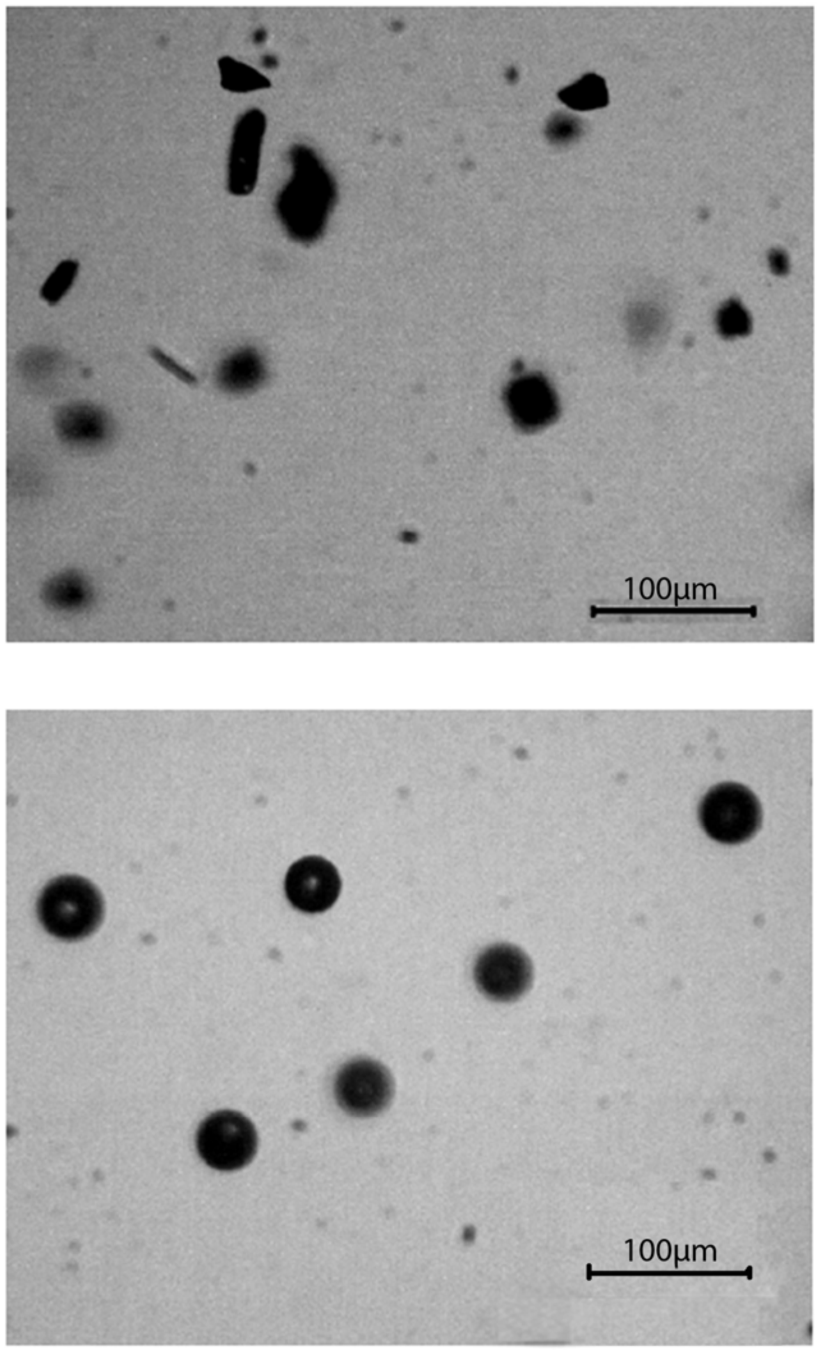

Figure 3.4: Typical shadowgraphy pictures of particles in flight: (a) 50µm aluminum oxide particles and (b) 50µm glass beads

To size the particles, a thresholding two step segmentation algorithm was applied to the images. The first segmentation located the particles in a so-called bounding box, and in the second step these segmentations were analyzed separately for size, shape and position. After all source images were analyzed, the velocity was calculated based on the two result lists. To identify pairs of particles, the algorithm had two conditions, i.e. the size and the allowed shift. As shown in Figure 3.5, the initial shift defined the centre position of the window in which particles were accepted. Particles were only accepted if the diameter deviation was within a preset range. This range was set to be +/- 15% for all experiments in Davis software. As a rule of thumb, the shift was at least 3 pixel and about half the size of the smallest particle to avoid ambiguities during the velocity calculation [46].

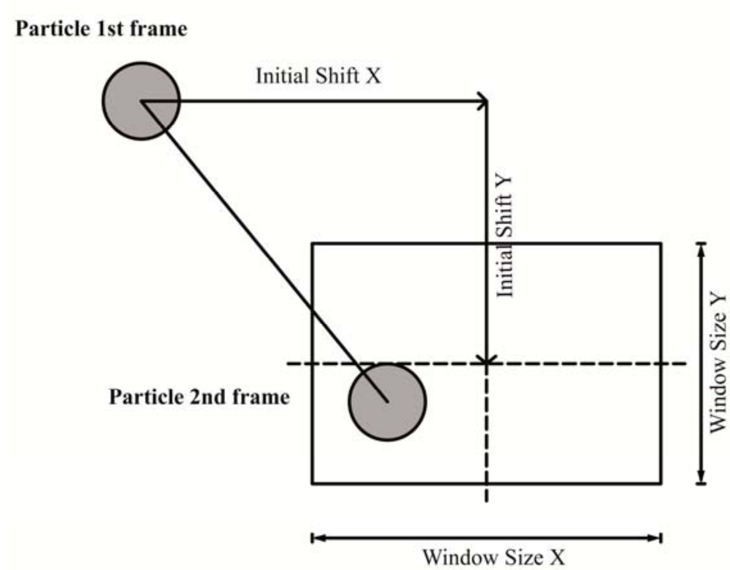

Figure 3.5: Illustration of interrogation window for determination of particle velocities

The number of particles passing through the mask opening depended on the particle size, the particle mass flow rate, and mask opening width. For conditions typical of AJM, there are relatively few particles in the opening at any given time. Nevertheless, it was very important to have a sufficiently large number of sampled images of particles in the focal plane of the shadowgraphy system in order to obtain a statistically reliable and repeatable particle size and velocity distribution. This was also complicated by the possibility of abrasive particles eroding the mask sidewalls and potentially affecting the particles' positions near the mask edges during the measurement period. For very thin masks that can rapidly wear all the way though their thickness, this might also change the effective mask opening width. The solid particle erosion of the steel mask depends on many factors such as material hardness, particle velocity, material, size and shape etc. For example, the erosion rate using angular particles is much higher than for spherical particles having a similar size [47]. Since in the present work, the variation in size distribution for angular particles was much broader than for spherical particles (Section 4.2), this further complicates matters. For these reasons, it was very important to experimentally determine the largest number of images that could be captured before the plates were significantly eroded.

By trial-and-error, it was found that approximately 3000 and 6000 double-frame images could be taken when using angular and spherical particles, respectively, before the mask erosion became significant. The average number of particles detected in the focal plane within the mask opening for each experiment was approximately 32500, or an average of approximately 5 particles per image. The average particle velocities measured from 1500 and 3000 shadowgraphy images of the angular aluminum oxide particles in flight inside the mask opening were within 5% of each other. This confirmed that the repeatability of the measurements was adequate using this number of frames. After analyzing a sufficient number of images, averages of the values such as particle velocity, size and mass were calculated in each particular bin. The bin sizes were varied for free jet and masked experiments based on the lens magnification and the number of the particles detected at certain positions in front of the camera.

CHAPTER 4

Measurements of particle spatial, velocity and size distributions

4.1. Velocity distribution of abrasive particles

Surface evolution models of abrasive jet machining require the distribution of particle velocities across the abrasive jet, or mask opening. This is because the erosion rates (i.e., mass of target material removed per mass of incident abrasive) of materials have a power law dependency on the particle impact velocity, with a velocity exponent that is often greater than 2 [48]. As mentioned in Section 2.3, Li et al [5] developed a mathematical free jet model to determine the particle velocity in a given axial and radial location within an abrasive air jet flow. However, the velocity of the particles inside the mask opening has never been measured before. In the present work, particle velocity distribution measurements were made in both the free jet and through the mask opening, for the same flow conditions (Tables 3.2 and 3.3), so that the disturbance in particle velocity brought about by the mask could be determined.

4.1.1. Velocity in Free Jet Incident to Mask and Comparison to Model of Li et al. [5]

The particle velocities across the free jet at a distance of 20 mm from the nozzle exit were measured and compared to the model of Li et al [5], which required knowledge of the nozzle diameter and length, particle mean diameter, particle density, air density, air flow velocity and particle drag coefficient. A Maple code was written to be able to calculate the air and particle velocities along the radial axis of the free jet model presented by Ref. [5] (Appendix C).

The process parameters for the free jet experiments are provided in Table 3.2. The model predicted a Gaussian or bell shape velocity profile across the jet with a maximum particle velocity at the jet center. Figs. 4.1 and 4.2 show that the predictions of Li et al.'s model [5], using the nominal diameters quoted by the manufacturer given in Table 3.1, fit the measured velocity distributions quite well for spherical particles

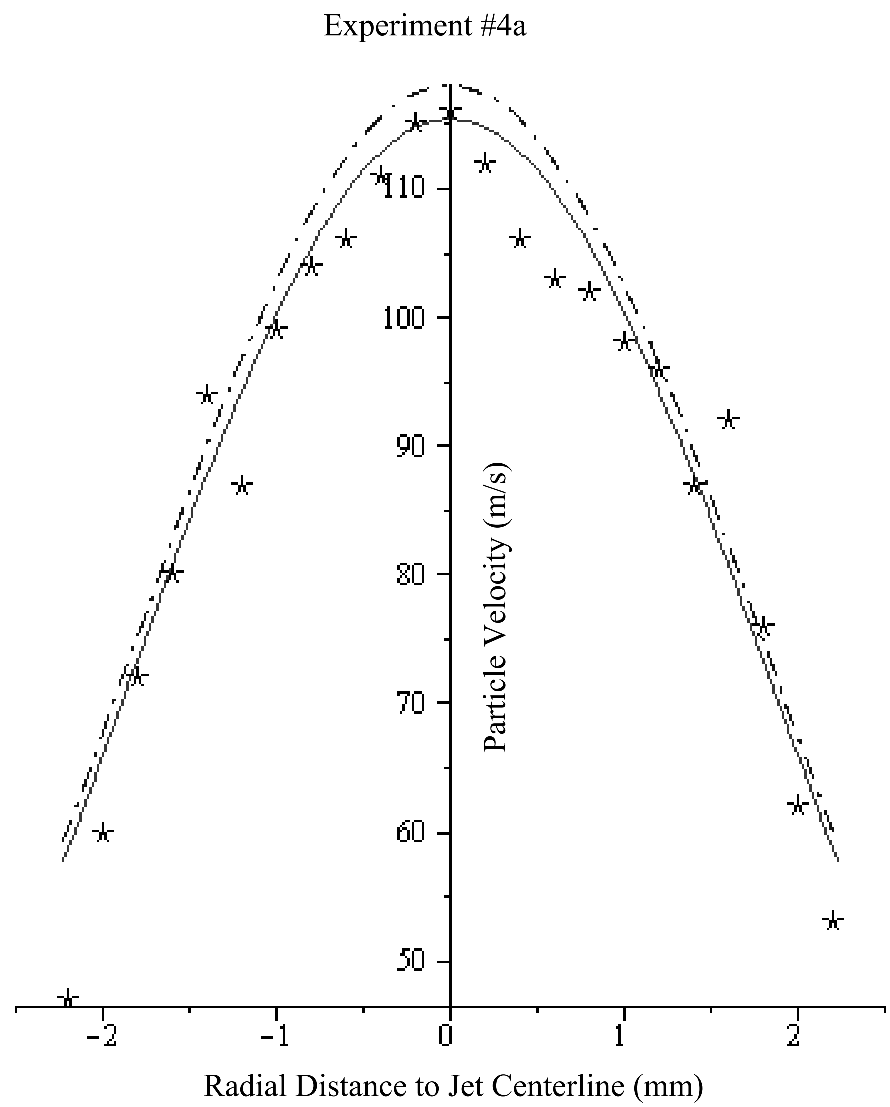

Figure 4.1: Plot of 50 μm glass bead velocities across the jet at a 20 mm standoff from the nozzle tip. Star symbols indicate particle velocity measured using shadowgraphy. The dashed line indicates predicted velocity using original model of [5], and solid line indicates model of [5] incorporating equation (4.1). The size of the averaging bins was 100 μm.

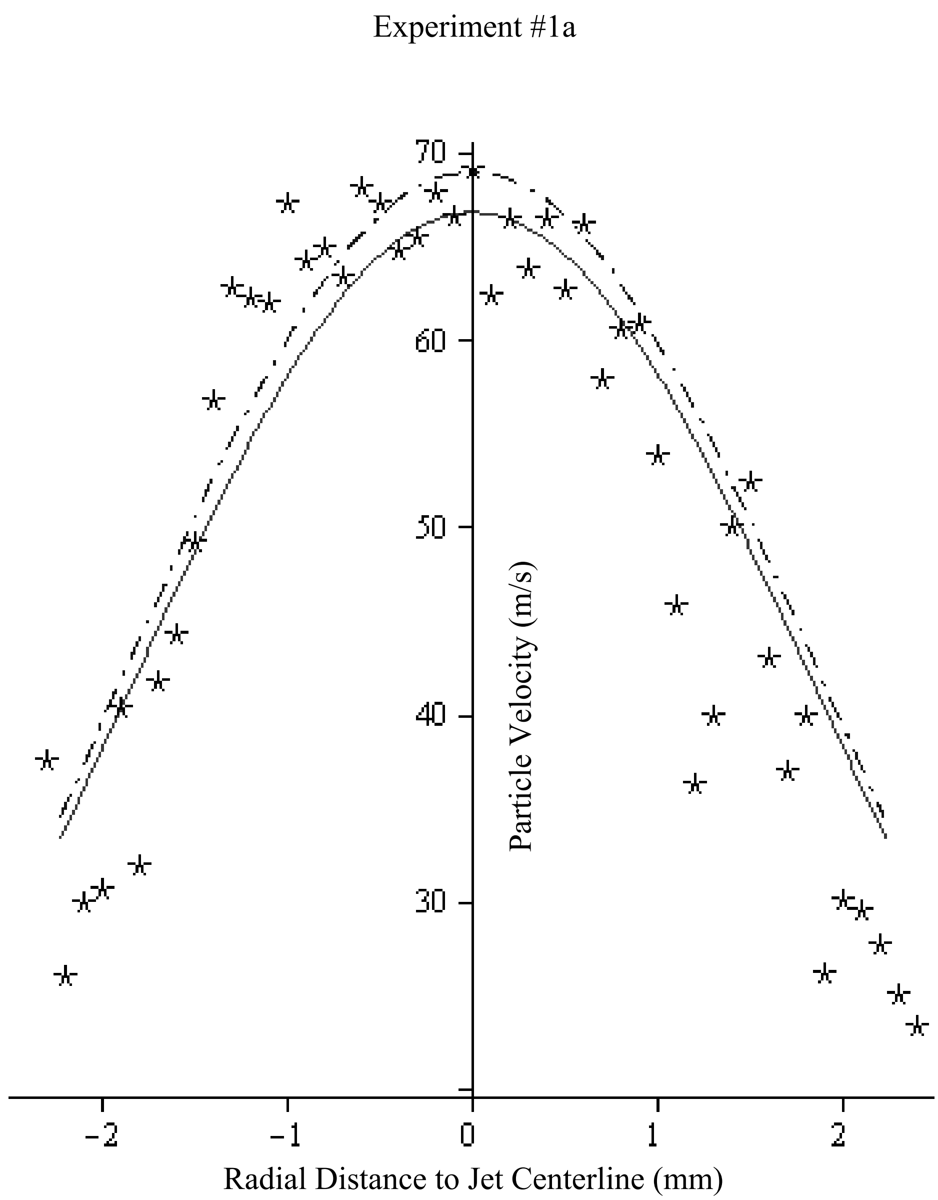

Figure 4.2: Plot of 50 μm chronital stainless steel velocities across the jet at a 20 mm standoff from the nozzle tip. Star symbols indicate particle velocity measured using shadowgraphy. The dashed line indicates predicted velocity using original model of [5], and solid line indicates model of [5] incorporating equation (4.1). The size of the averaging bins was 100 μm.

Use of the average diameters measured by shadowgraphy (Section 4.2) in the model resulted in very similar results. For the angular particles, the model of Li et al. [5] significantly under-predicted the measured particle velocity distribution, as shown in Figs. 4.3 to 4.6. The reason for this is that the particle drag coefficient that Li et al. assumed was for spherical particles. The changes in momentum and velocity of the particles depend strongly on their drag coefficients, which themselves, if the particles are non-spherical, strongly depend on the particle shape and orientation. Therefore, the following relationship for the drag coefficient, C_D, suggested by Haider and Levenspiel [14], was introduced into the model of Li et al.:

$$C_D = \frac{24}{\mathrm{Re}}[1+[8.1716\exp(-4.0655\varphi)]\times \mathrm{Re}^{(0.0964+0.5565\varphi)}] + \frac{73.69\ \mathrm{Re}\ \exp(-5.0748\varphi)}{\mathrm{Re} + 5.378\ \exp(6.2122\varphi)} \quad (4.1)$$

where $\mathrm{Re} < 2.6\times10^5$ is the particle relative Reynolds number and φ is the sphericity of the particles. Since particles experience a higher drag force as they become less spherical, the particle velocity increases with decreasing φ. The particle relative Reynolds number is given by [49]

$$\mathrm{Re} = \frac{\rho_A d_P \Delta V}{\mu} \quad (4.2)$$

where ρ_A is the air density at a given nozzle cross-section, d_P is the mean particle diameter, μ is the viscosity of air at room temperature and ΔV is the relative air/particle velocity. The sphericity of a particle is given by [50]

$$\varphi = \frac{A_s}{A_p} = \frac{\pi^{\frac{1}{3}}(6V_p)^{\frac{2}{3}}}{A_p} \tag{4.3}$$

where A_p is the measured particle surface area, and A_s is the surface area of a sphere with the same volume as the particle. The average sphericities of the powders given in Table 3.1 were measured using the shadowgraphic images (see similar sizing procedure in Section 4.2) and used in equation (4.1) to modify the drag coefficient in the model of Li et al. With this modification of the drag coefficient, Figs. 4.1 to 4.6 show that there was excellent agreement with the measured velocities for the spherical and non-spherical particles.

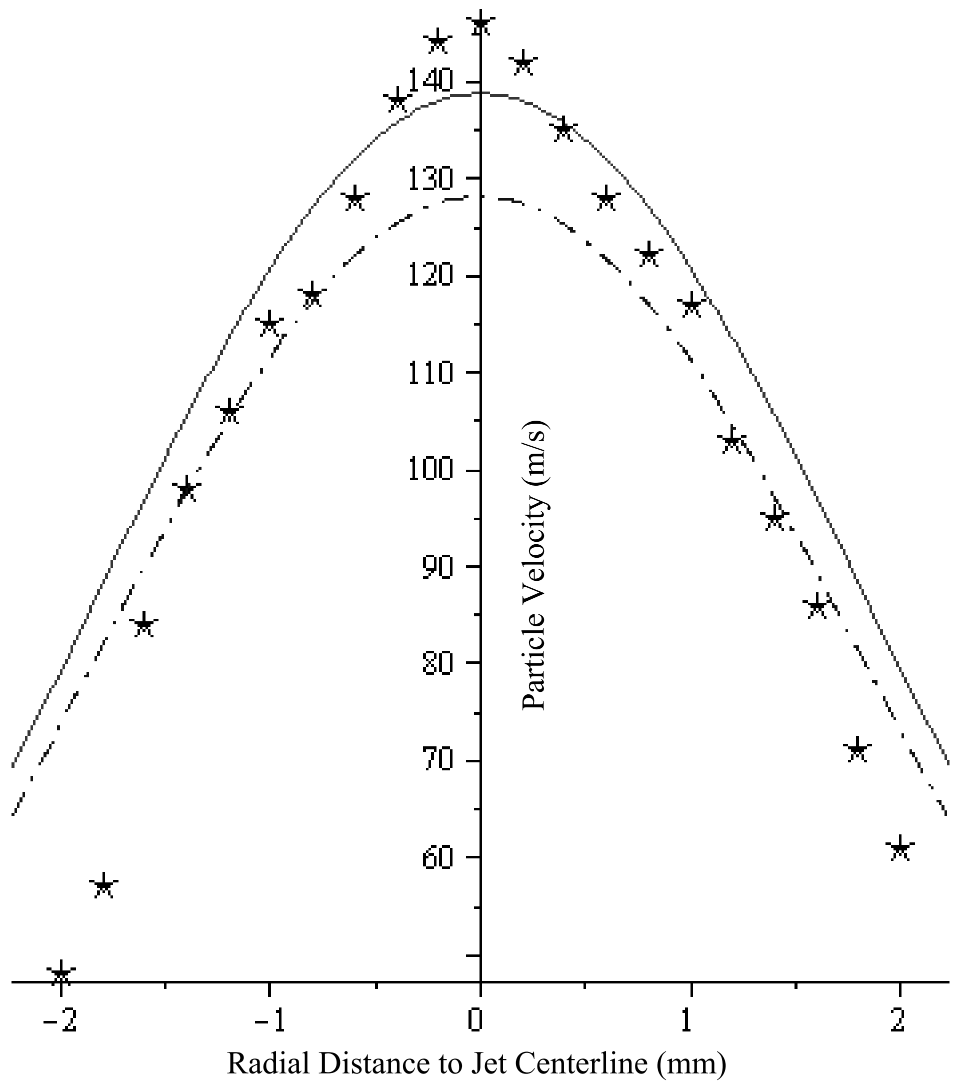

Figure 4.3: Plot of velocities of 50 µm crushed glass (Experiment #3a) across the jet at a 20 mm standoff from the nozzle tip. Star symbols indicate particle velocity measured using shadowgraphy. The dashed line indicates predicted velocity using original model of [5], and solid line indicates model of [5] incorporating equation (4.1). The size of the averaging bins was 100 µm.

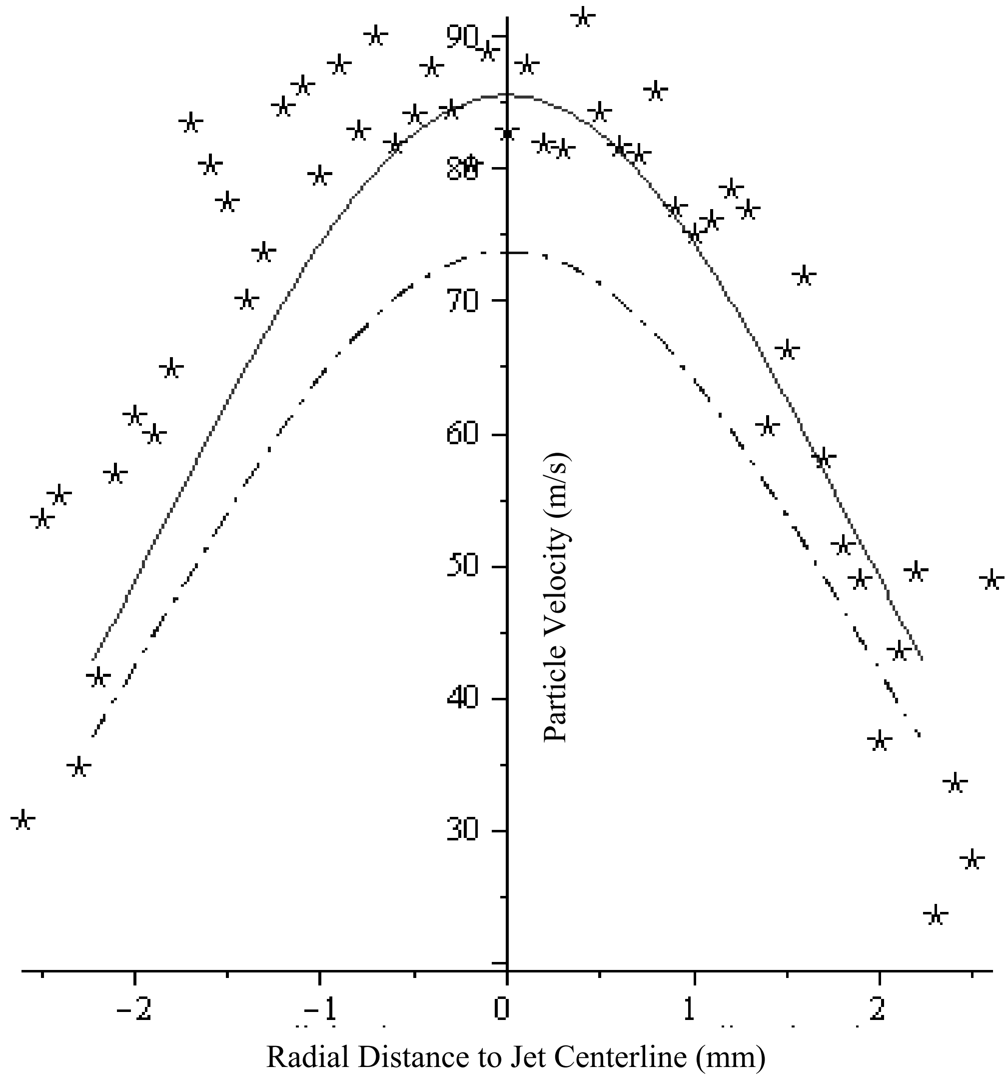

Figure 4.4: Plot of velocities of 50 µm grittal stainless steels (Experiment #2a) across the jet at a 20 mm standoff from the nozzle tip. Star symbols indicate particle velocity measured using shadowgraphy. The dashed line indicates predicted velocity using original model of [5], and solid line indicates model of [5] incorporating equation (4.1). The size of the averaging bins was 100 µm.

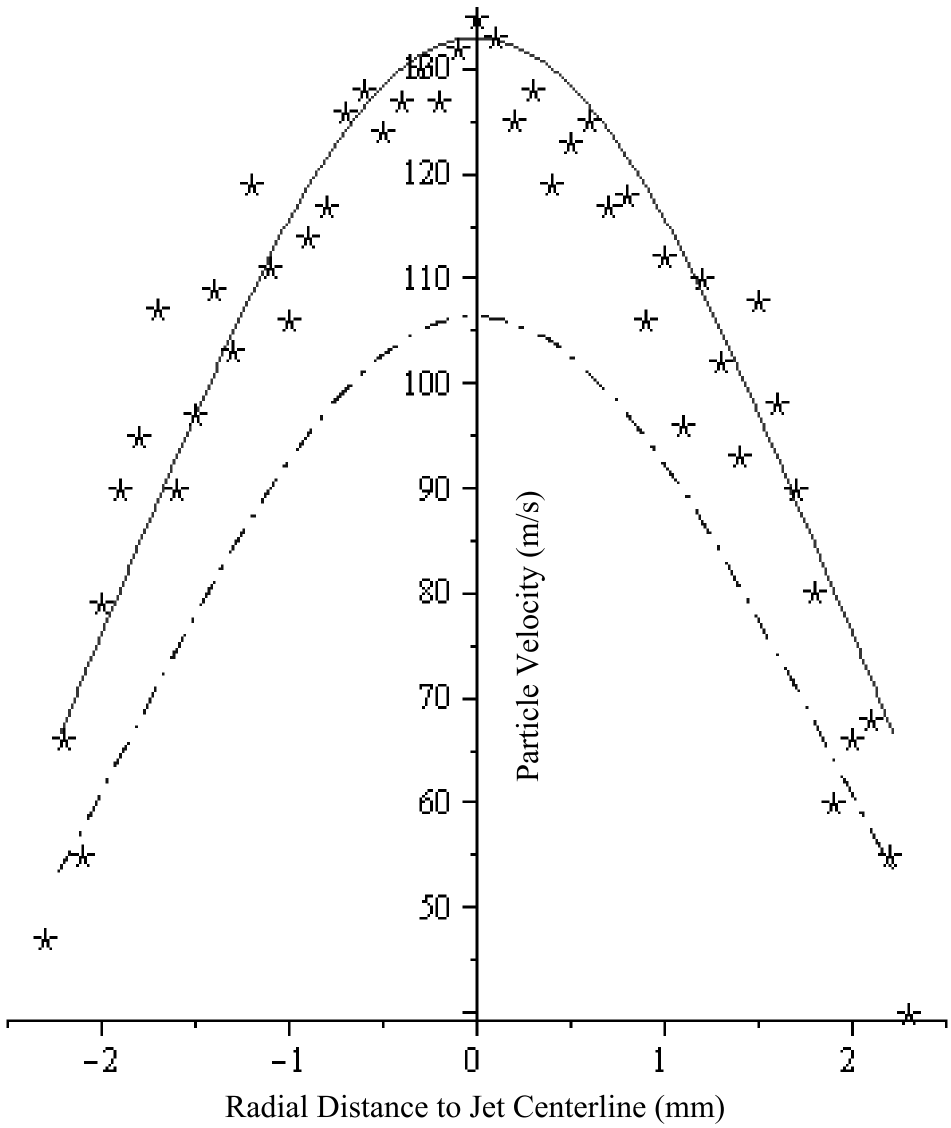

Figure 4.5: Plot of velocities of 50 μm Al_2O_3 (Experiment #6a) across the jet at a 20 mm standoff from the nozzle tip. Star symbols indicate particle velocity measured using shadowgraphy. The dashed line indicates predicted velocity using original model of [5], and solid line indicates model of [5] incorporating equation (4.1). The size of the averaging bins was 100 μm.

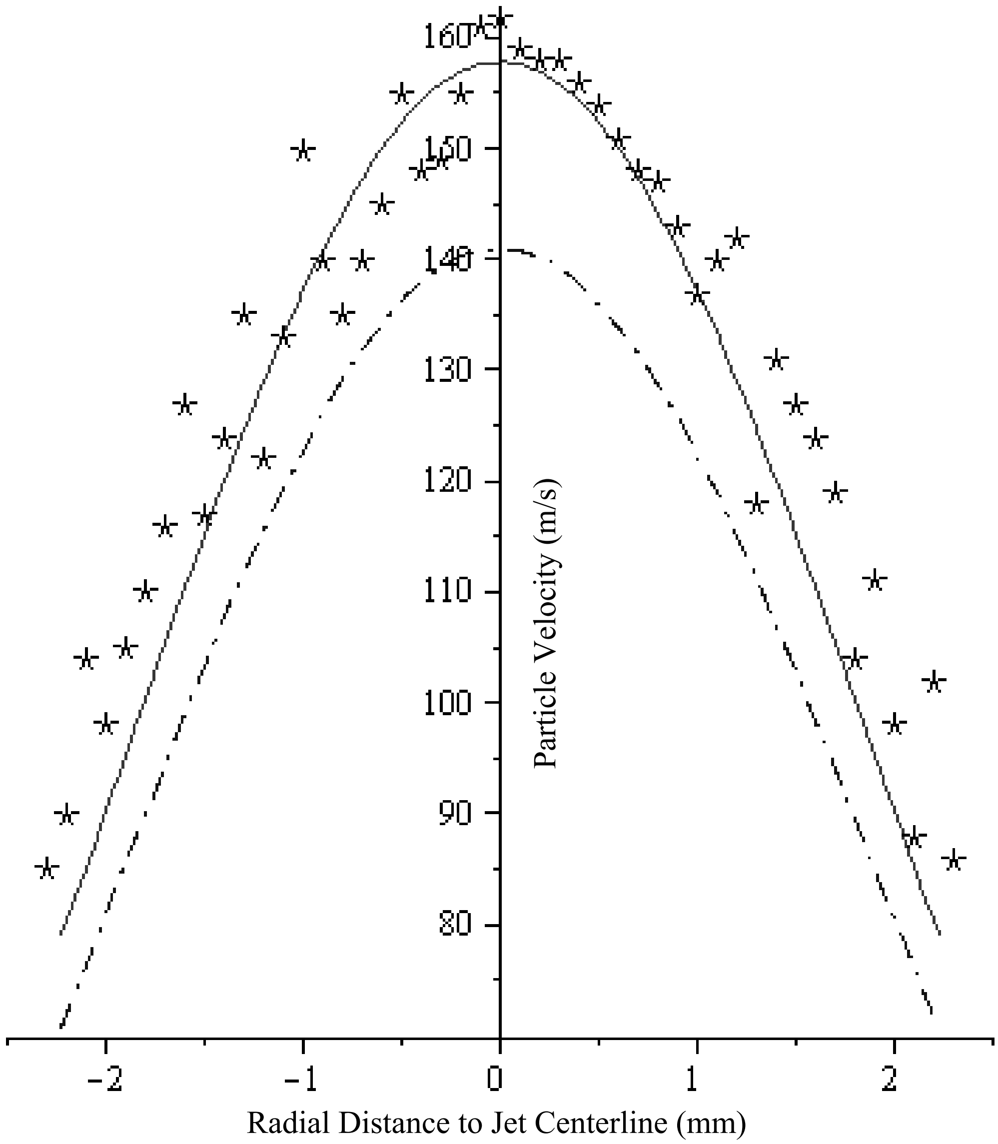

Figure 4.6: Plot of velocities of 25 µm Al_2O_3 (Experiment #5a) across the jet at a 20 mm standoff from the nozzle tip. Star symbols indicate particle velocity measured using shadowgraphy. The dashed line indicates predicted velocity using original model of [5], and solid line indicates model of [5] incorporating equation (4.1). The size of the averaging bins was 100 µm.

Comparing Figs. 4.1 and 4.3 for spherical and angular 50 µm glass media or Figs. 4.2 and 4.4 for spherical and angular 50µm stainless steel particles demonstrates that, as expected, the particle velocity was higher for angular than for spherical particles. For example, the magnitude of the particle velocity at the center of the jet for the 50 micron crushed glass with φ=0.80 was measured to be 140 m/s (Fig. 4.3), while the velocity of 50 micron glass beads with φ=1 was approximately 115m/s (Fig. 4.1).

4.1.2. Particle velocity distribution through the mask opening

The ratio of the mask opening width to the jet spot size in AJM applications is typically less than 0.1, as reflected in the mask opening width (0.5 mm) and the jet spot size at a 20 mm standoff from the nozzle tip (5-6 mm) used in the present experiments. Therefore, one would expect that the particle velocity across the narrow mask opening should be approximately uniform at its value at the jet centre in Figs. 4.1 to 4.6. However, the disturbance of the particle flow due to the presence of the mask and the particle ricochet from the mask edges and sidewalls has never been measured. All previously utilized AJM models have thus assumed these disturbances in particle velocity to be negligible. Figs. 4.7 to 4.10 show the measured velocity distributions inside the mask opening for the different abrasive particles, corresponding to the experiments in Table 3.3. For the relatively thick mask plates (i.e., ratio of the mask thickness to the mask opening ~0.5) used in the present study, the velocity distribution is approximately uniform inside the mask opening, consistent with what has been typically assumed in surface evolution models. However, as can be seen by comparing the free jet centerline velocities (Figs. 4.1 to 4.6) to the velocities through the mask (Fig. 4.7 to 4.10) under identical conditions, the velocities through the mask are significantly lower than those in the free jet. For example, for both spherical and non-spherical stainless steel particles of similar size, the average velocity through the masks (Figs. 4.7 and 4.8) was approximately 25m/s lower than the centerline velocities in the free jet (Figs. 4.2 and 4.4), under otherwise identical blasting conditions. Comparison of Figs. 4.6 and 4.10 shows that this effect was even more significant for the 25μm aluminum oxide.

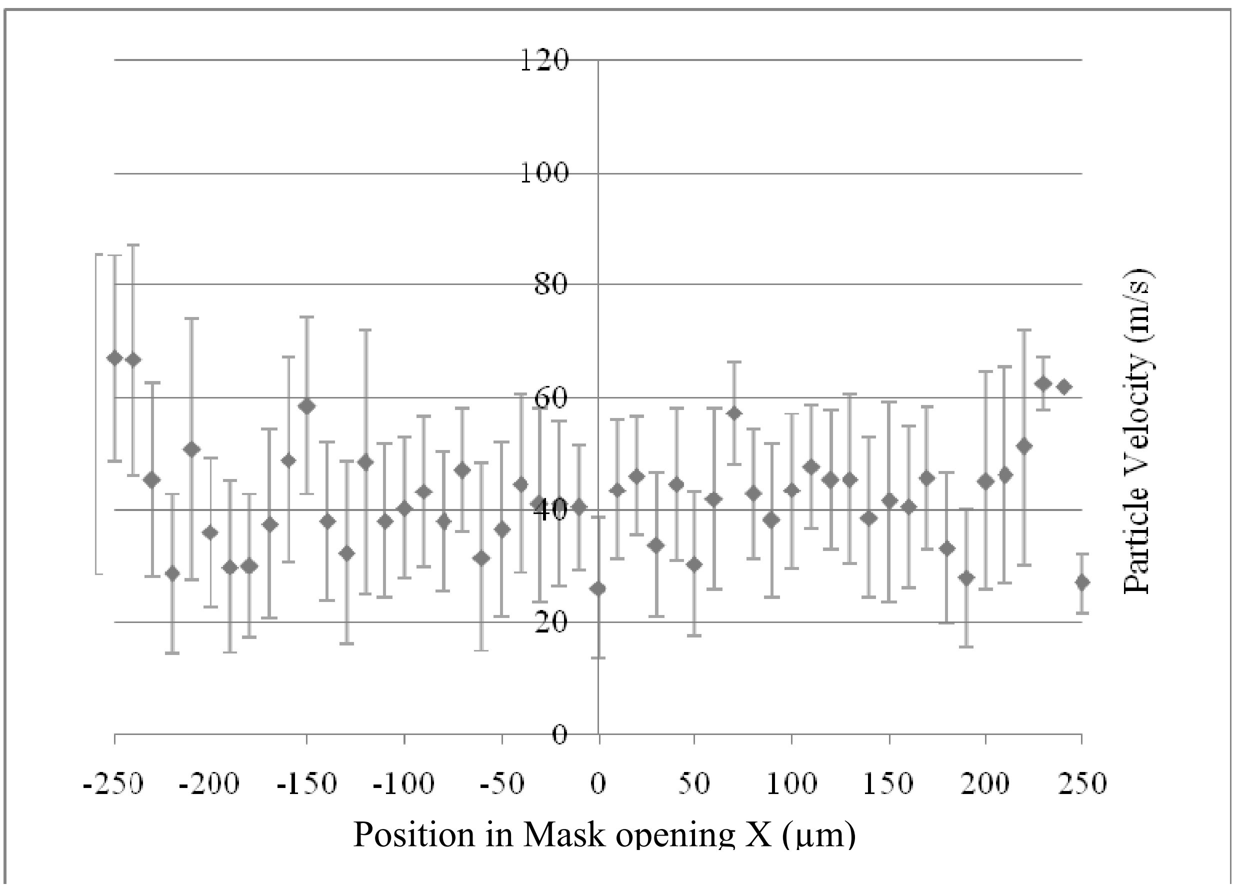

Figure 4.7: Measured velocity distributions of 50 μm chronital stainless steels in 500 μm mask opening (Experiment #1b). A zero position indicates the center of the mask opening (Fig. 4.14). Error bars represent the sample standard deviations in a bin of 10 μm width.

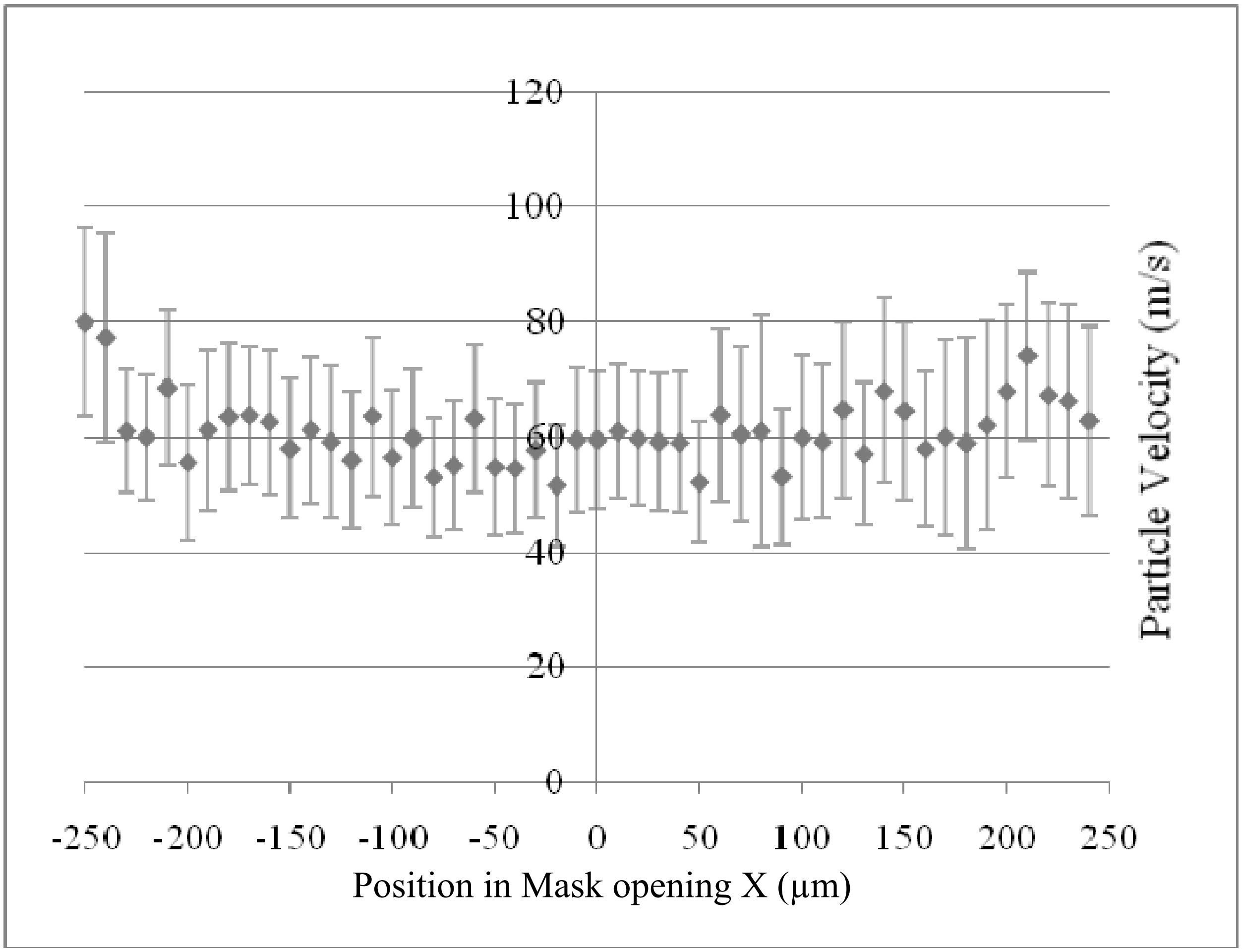

Figure 4.8: Measured velocity distributions of 50 μm grittal stainless steels in 500 μm mask opening (Experiment #2b). A zero position indicates the center of the mask opening (Fig. 4.14). Error bars represent the sample standard deviations in a bin of 10 μm width.

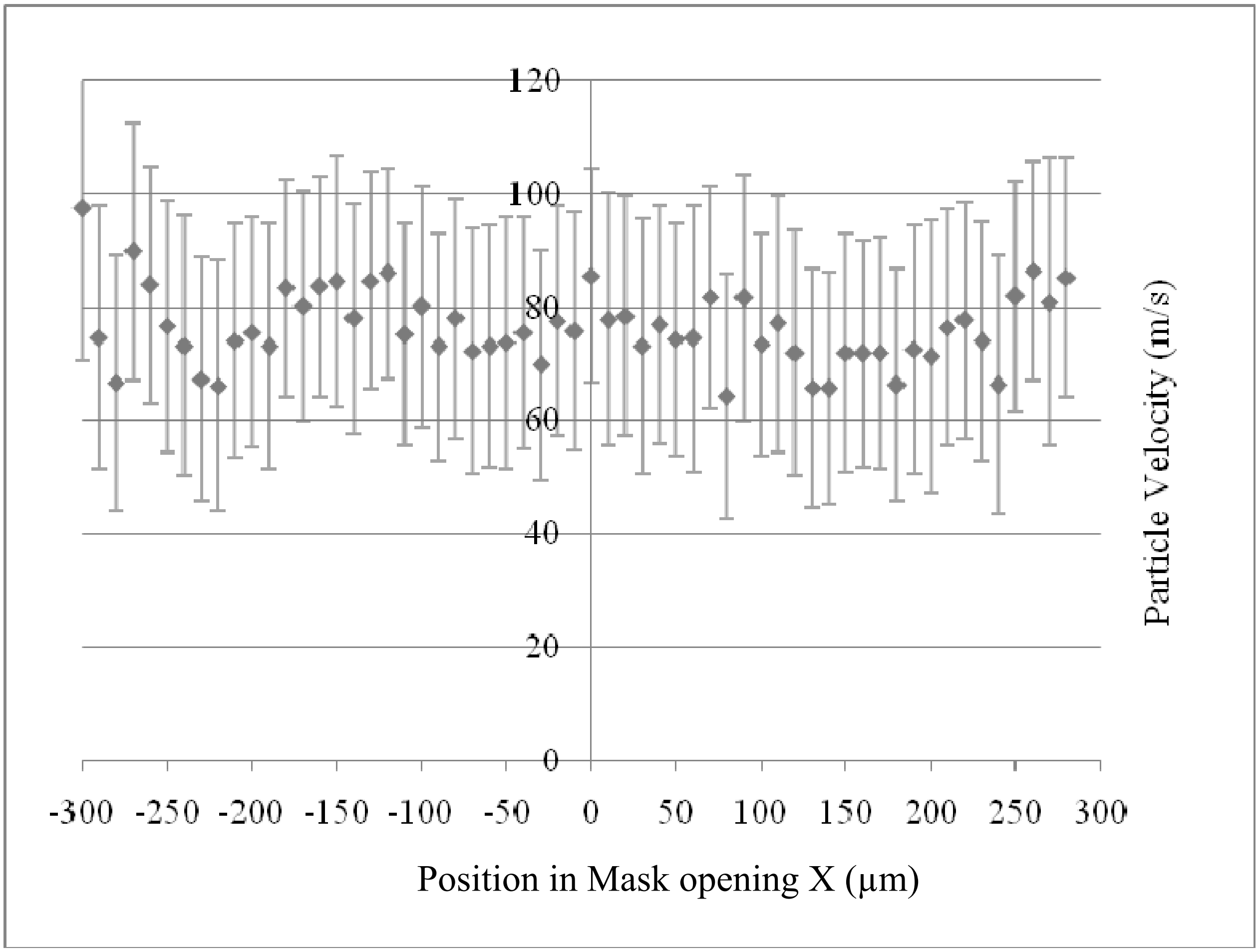

Figure 4.9: Measured velocity distributions of 50 µm glass bead in 600 µm mask opening (Experiment #4b). A zero position indicates the center of the mask opening (Fig. 4.14). Error bars represent the sample standard deviations in a bin of 10 µm width.

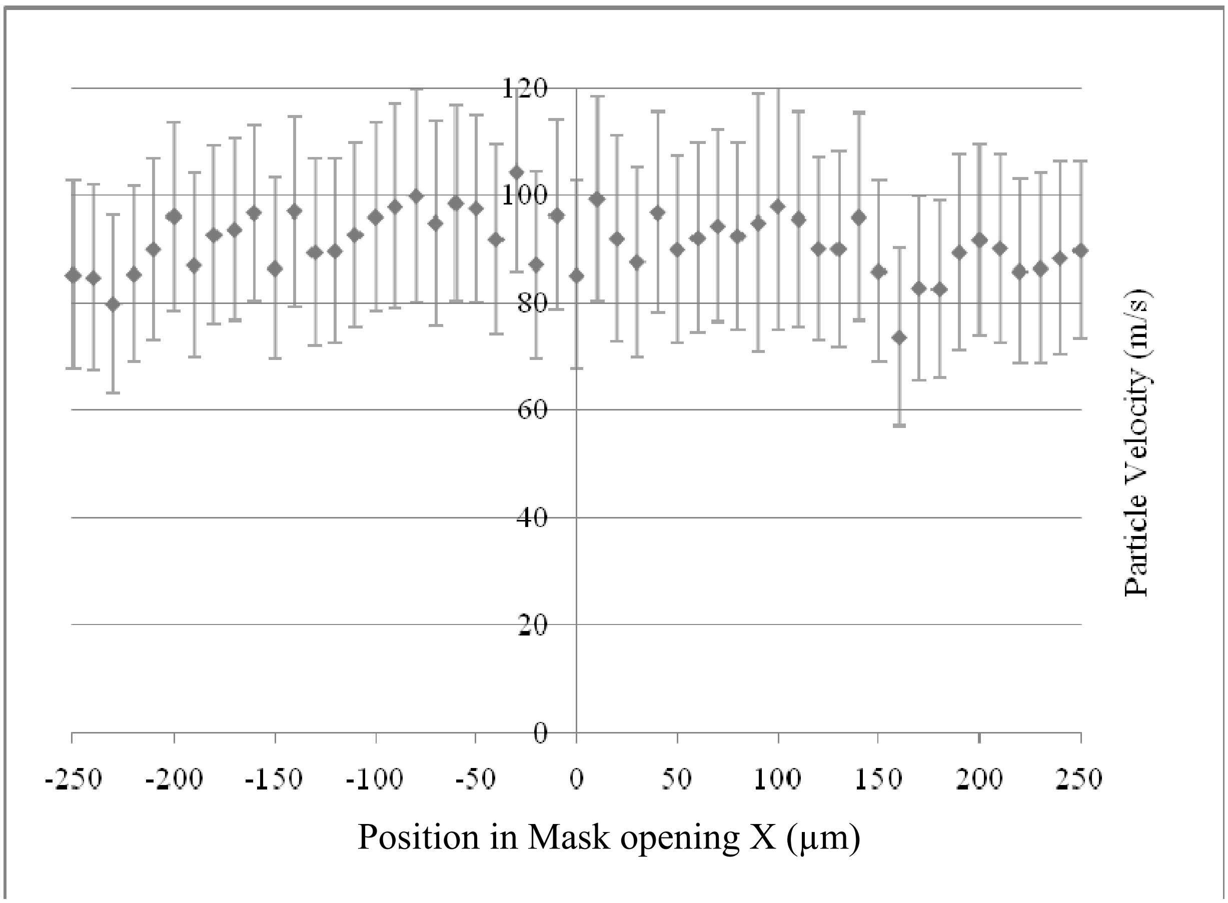

Figure 4.10: Measured velocity distributions of 25 μm Aluminum Oxide in 500 μm mask opening (Experiment #5b). A zero position indicates the center of the mask opening (Fig. 4.14). Error bars represent the sample standard deviations in a bin of 10 μm width.

Figure 4.11 shows the measured velocity vectors of the individual particles, where the vector length corresponds to the particle velocity magnitude at a certain position inside the mask opening. It is evident that the particle velocity magnitudes of most of the rebounding particles are much lower than those of the non-rebounding particles. Hence, the effect of particle ricochet from the mask edges and sidewalls was minimum, as was also demonstrated under similar conditions in the particle tracking simulations of Ref. [28].

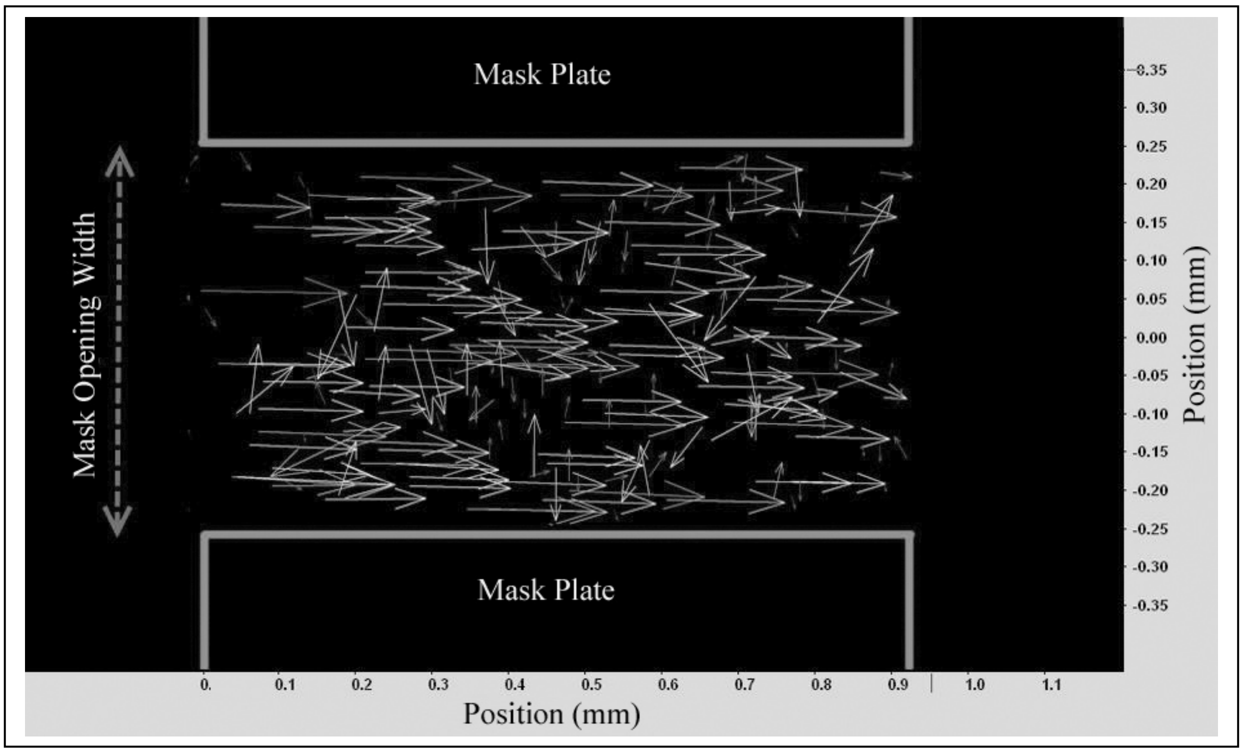

Figure 4.11: Particle velocity vectors inside the mask opening showing that most of particles ricocheting from the mask edge have a much lower velocity than those passing straight through the mask. Experiment #5b with 100 images processed for clarity.

4.2. *Particle size distribution in the free jet*

The abrasive size distribution generally affects the particle mass flux, and, in turn, the erosion rate during AJM. Earlier studies of masked AJM have demonstrated that the particle size distribution can also greatly affect the shape and depth of micro-channel profiles [6]. However, in these previous studies, a microscope and image analysis system was used to measure samples of abrasive particles lying stationary on a flat plate. Such a methodology may suffer from a bias related to the tendency of particles to lie with their shortest axis normal to the surface, thus skewing the sizing result. This is especially true for flaky particles that are much larger in one dimension than the other two. In the present work, the particle size distributions and parameters such as the mean size and equivalent spherical diameter of angular particles were measured using shadowgraphy while the particles were in flight, allowing for a more random orientation of particles, thus reducing this bias. Using the Lavision Davis 7.2.2 software, the equivalent area spherical diameters of the particles were measured from the shadowgraphy images. For each particle in the shadowgraphy images, the longest and shortest axes were measured. The corresponding equivalent area spherical diameter was computed assuming the particle to be a circle with an area equivalent to that from that in the shadowgraphy image, using [51]:

$$d_P = (l/\sqrt{2})\left[1+\left[s\sqrt{s^2-1}\right]^{-1}\ln\left[s+\sqrt{s^2-1}\right]\right]^{\frac{1}{2}} \tag{4.4}$$

where l is major (longest) axis, t is minor (shortest) axis and $s=l/t>1$ is the axial ratio for each cases.

Figs. 4.12 and 4.13 show that normal, and log-normal distributions best fit the measured equivalent particle radius distributions for spherical and angular particles, respectively. The size distributions of spherical particles were more uniform than those of the angular particles, and, in some cases, the average particle size calculated using shadowgraphy differed from the nominal particle size quoted by the manufacturer (Table 3.1). It should also be noted that no correlation of particle size with position in the free jet was found, i.e., all particle sizes had an equal probability of being found at a particular location within the jet.

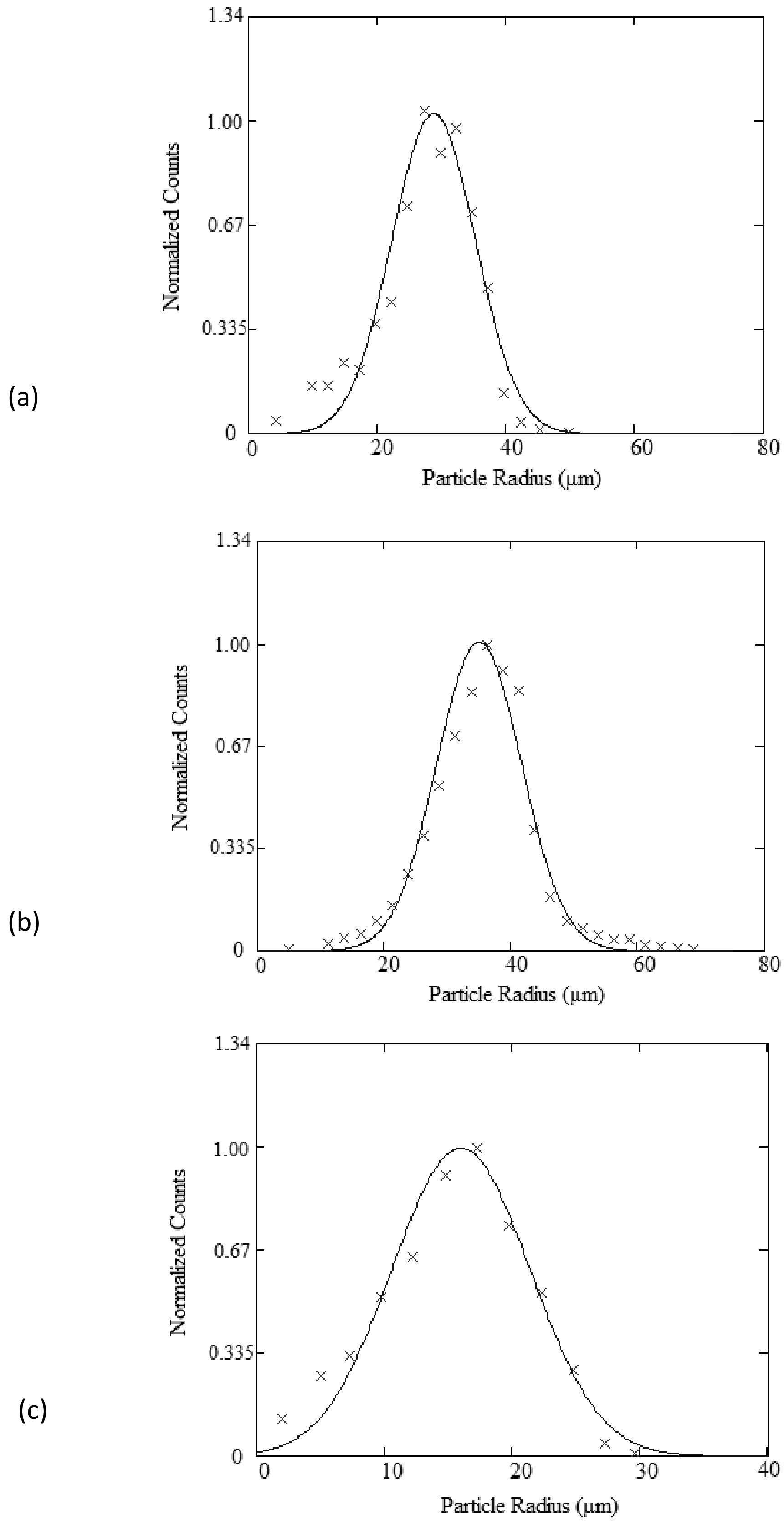

Figure 4.12: Particle size distribution of spherical particles incident to the mask opening for (a) 50 μm glass beads; (b) 50 μm stainless steel beads; (c) 35 μm glass beads. X symbols indicate shadowgraphy measurements, and solid lines indicate least square best fits to a normal distribution. The size of the averaging bins was 2.5 μm.

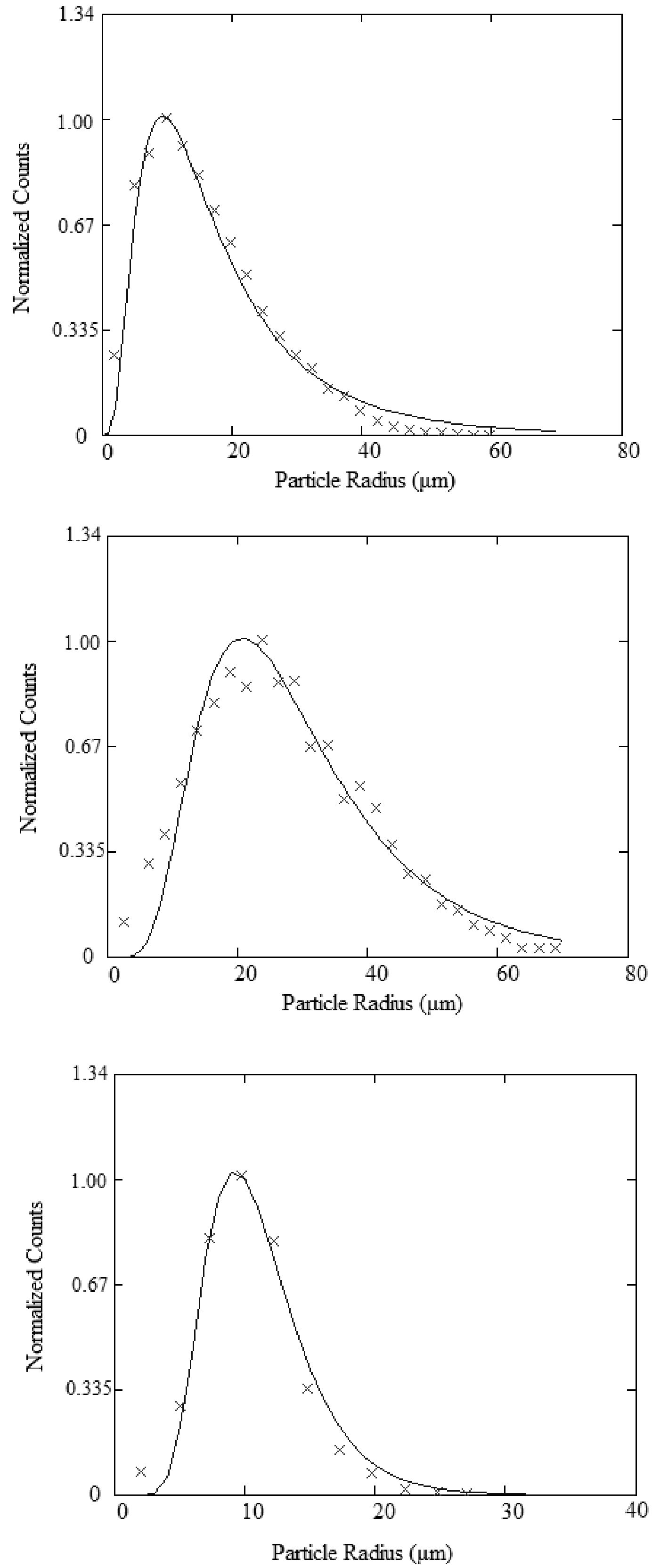

(a)

(b)

(c)

Figure 4.13: Equivalent spherical radius distribution of angular particles incident to the mask opening for: (a) 50 μm crushed glass; (b) 50 μm stainless steel grit ; (c) 25 μm aluminum oxide. X symbols indicate shadowgraphy measurements, and solid lines indicate least square best fits to a log-normal distribution. The

4.3.   Particle size distribution within the mask opening

The distribution of the particle sizes inside the mask opening is very important to study since it directly affects the mass flux and, consequently, the resulting surface erosion. It has previously been hypothesized by a number of authors (e.g., [1], [6]) that the decrease in mask flux beside the mask edges occurs because, as the edges are approached (i.e., $x_1 \rightarrow w/2$ in Fig. 4.14), the maximum particle size than can pass through the mask without striking it decreases. In other words, at the center of the mask opening ($x_1=0$), particles of all sizes can pass, whereas at the mask edge only the small particles in the powder size distribution can pass. Figs. 4.15 - 4.20 show   the measured particles size distributions inside the mask opening, which confirm that only the smallest particles indeed reach the mask edge.

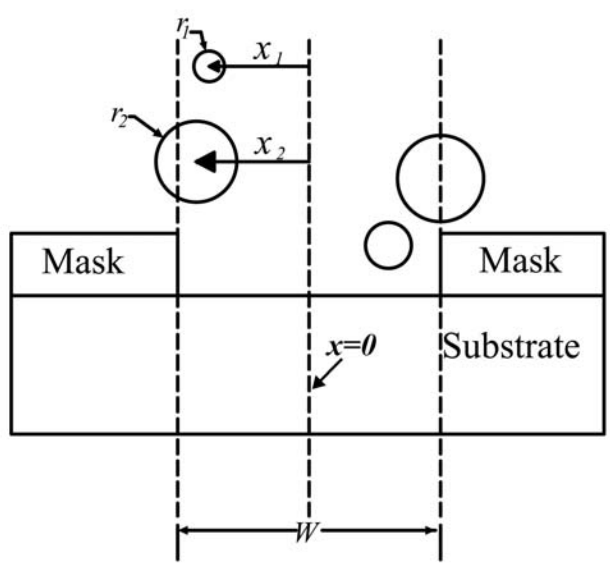

Figure 4.14: Schematic showing that smaller particles (r_1) can pass closer to the mask edge than larger ones (r_2).

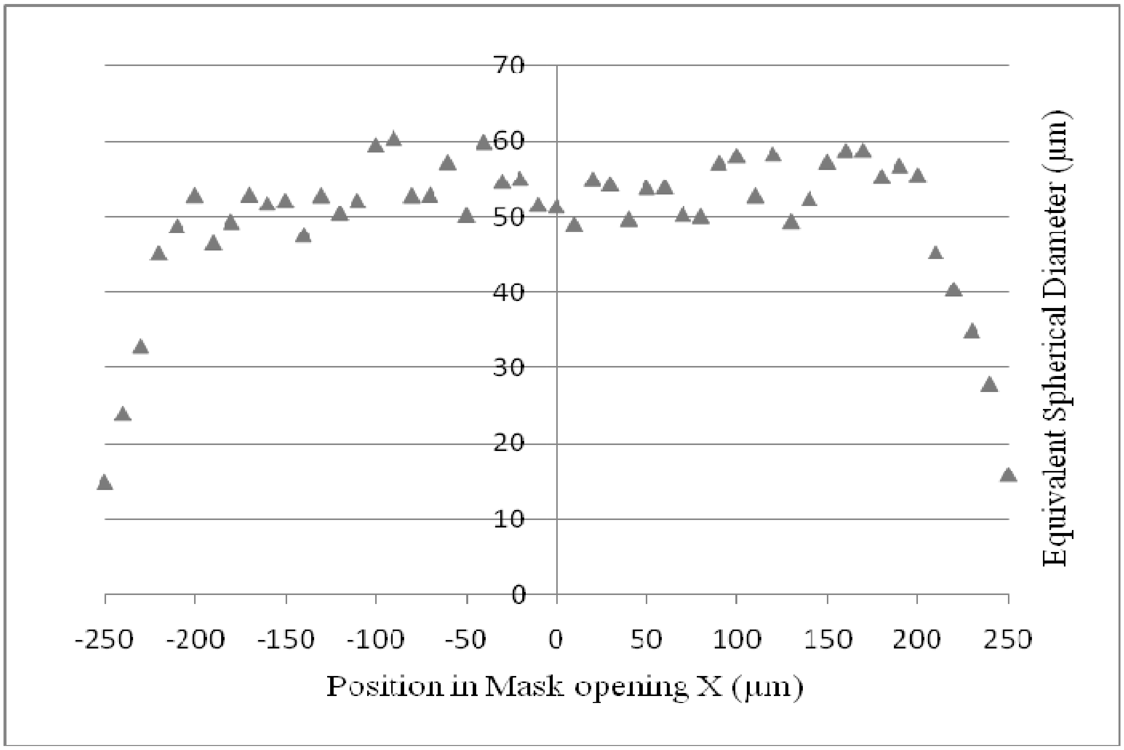

Figure 4.15: Particle size distribution measured in the mask opening for 50 µm spherical stainless steels (Experiment #1b)

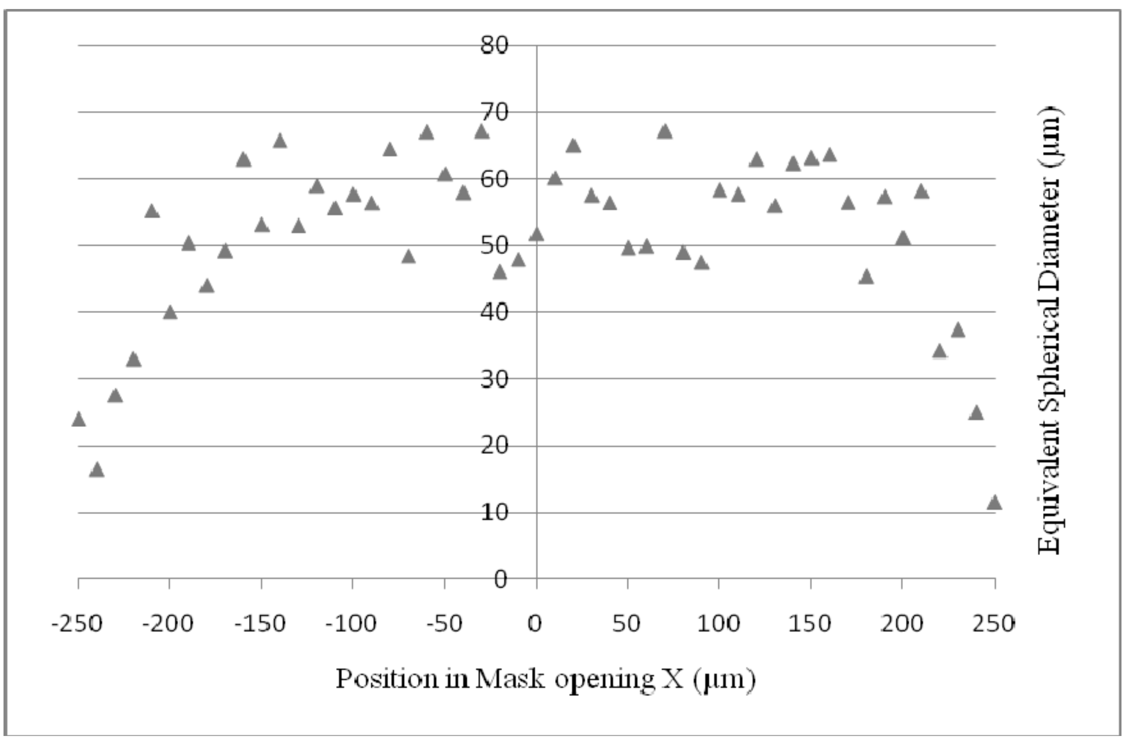

Figure 4.16: Particle size distribution measured in the mask opening for 50 µm grittal stainless steels (Experiment #2b)

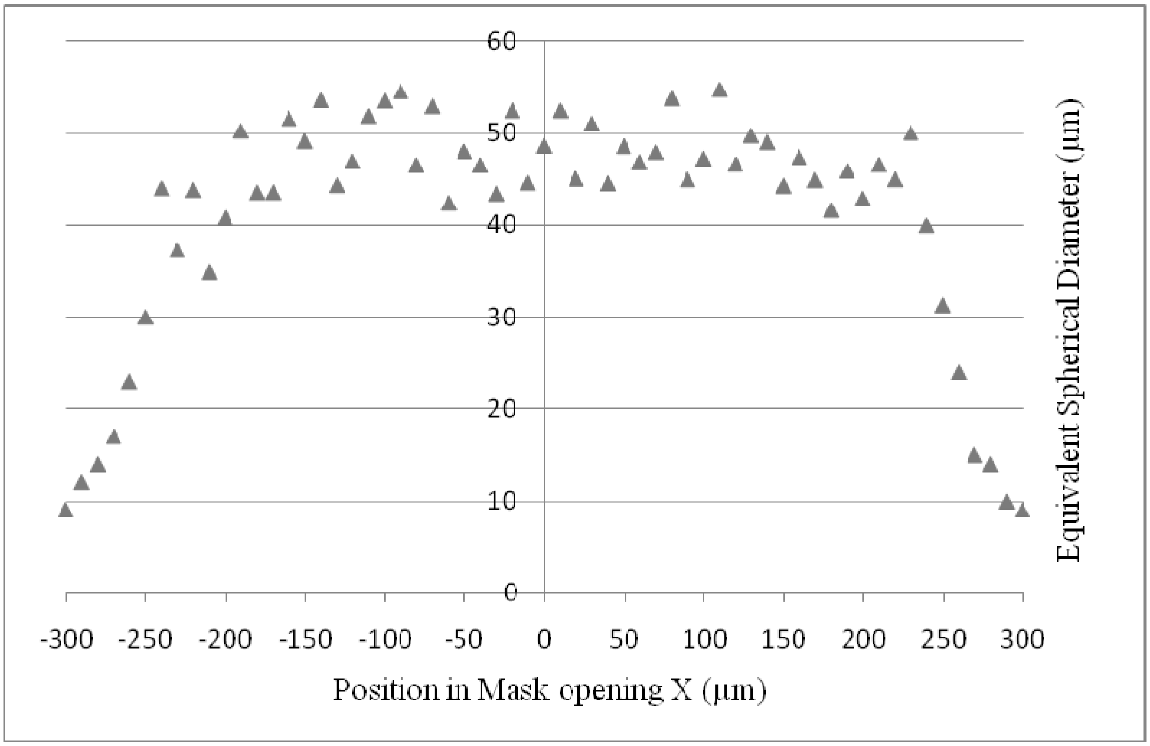

Figure 4.17: Particle size distribution measured in the mask opening for 50 µm crushed glass (Experiment #3b)

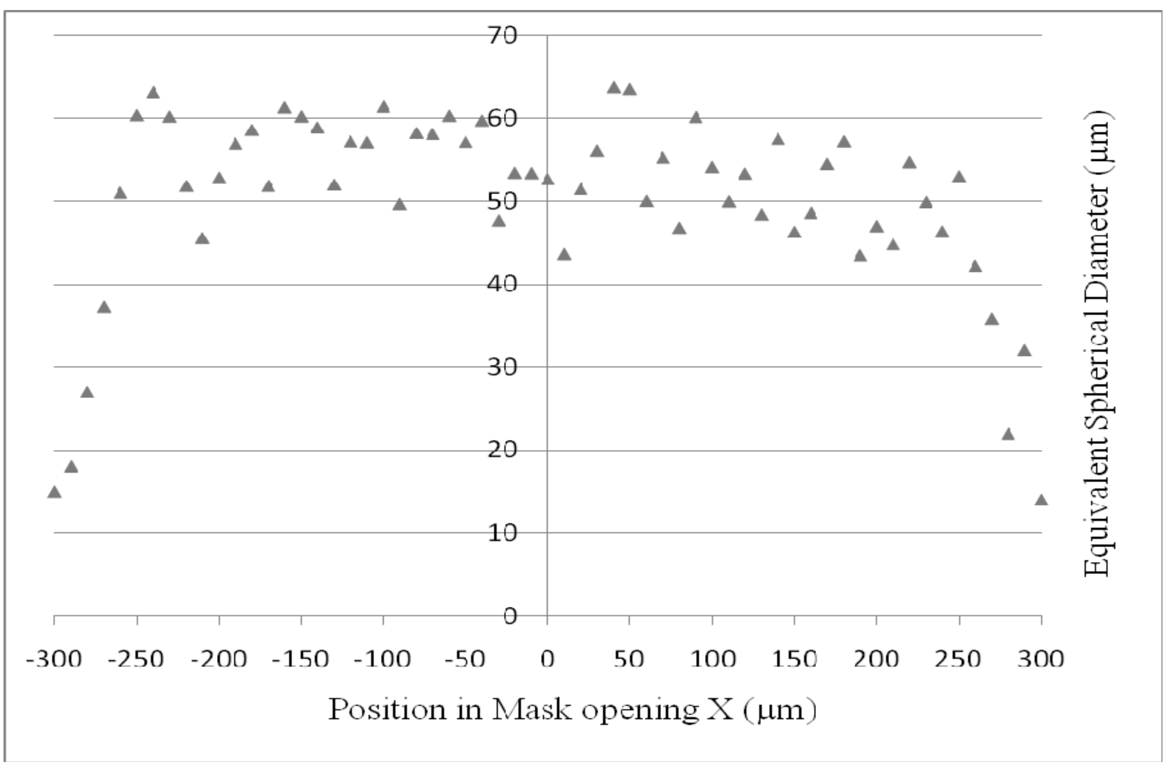

Figure 4.18: Particle size distribution measured in the mask opening for 50 µm glass beads (Experiment #4b)

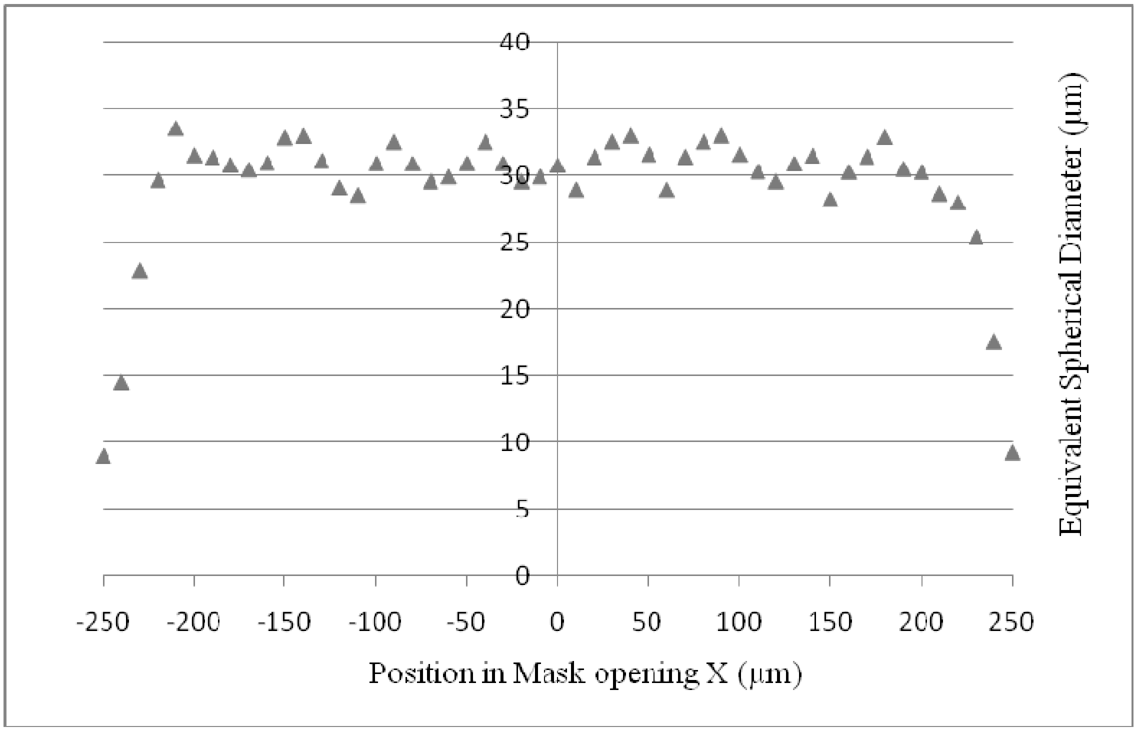

Figure 4.19: Particle size distribution measured in the mask opening for 35 µm glass beads (Experiment #4c)

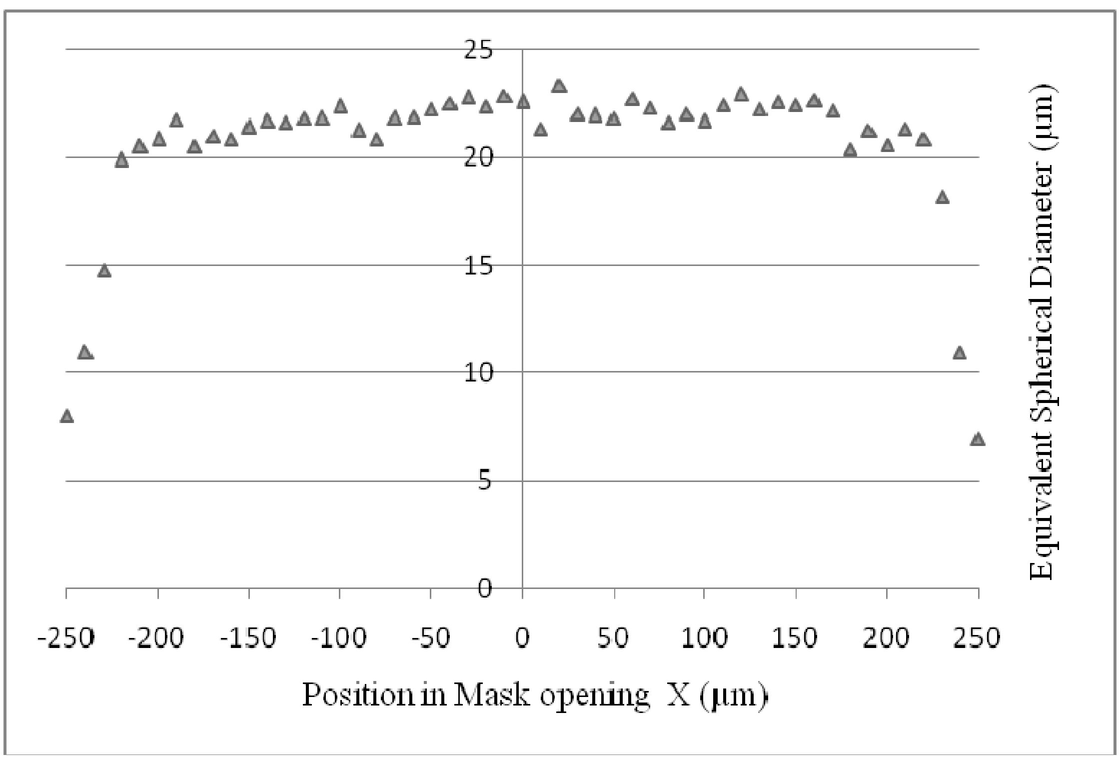

Figure 4.20: Particle size distribution measured in the mask for 25 µm Al_2O_3 (Experiment #5b)

Comparison of the size distributions of spherical and non-spherical particles inside the mask opening with approximately the same nominal diameters are presented in Figs. 4.21 and 4.22. Fig. 4.21 represents the size distribution of spherical versus angular stainless steels and Fig. 4.22 shows the relative values for 50μm glass media. The mask opening width was divided up into 10 μm wide bins and the average particle sizes in each bin were then normalized by the value at the center of the channel. The measurements from both sides of the mask opening were averaged. Since the spherical particles such as chronital stainless steels and glass beads are more uniform in size distribution (section 4.2), they have shown a sharper drop towards the mask edge. In contrast, the angular particles of the same material and similar diameter sizes resulted in a smoother drop beside the edges.

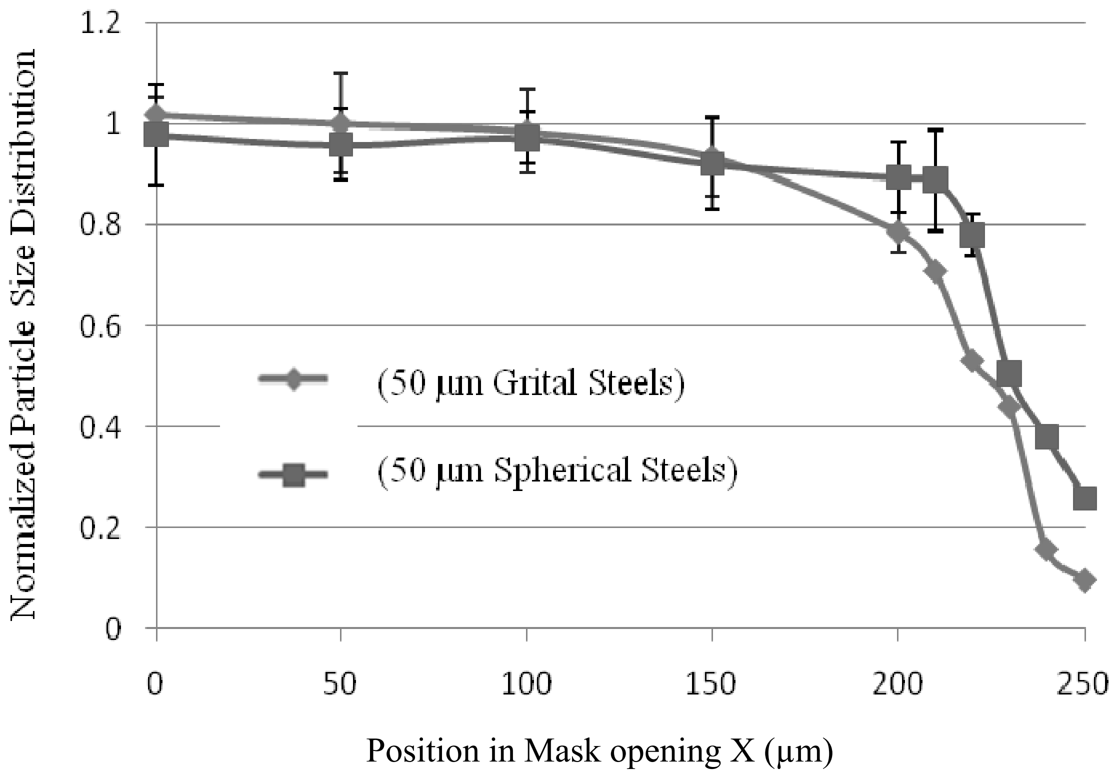

Figure 4.21: Normalized particle size distribution inside the mask opening using 50μm spherical and non-spherical stainless steels. The plot symbols are the measured quantities. Only half the symmetrical mask opening width is shown. A zero position indicates the center of the mask opening (Fig. 4.14). Error bars represent the sample standard deviations.

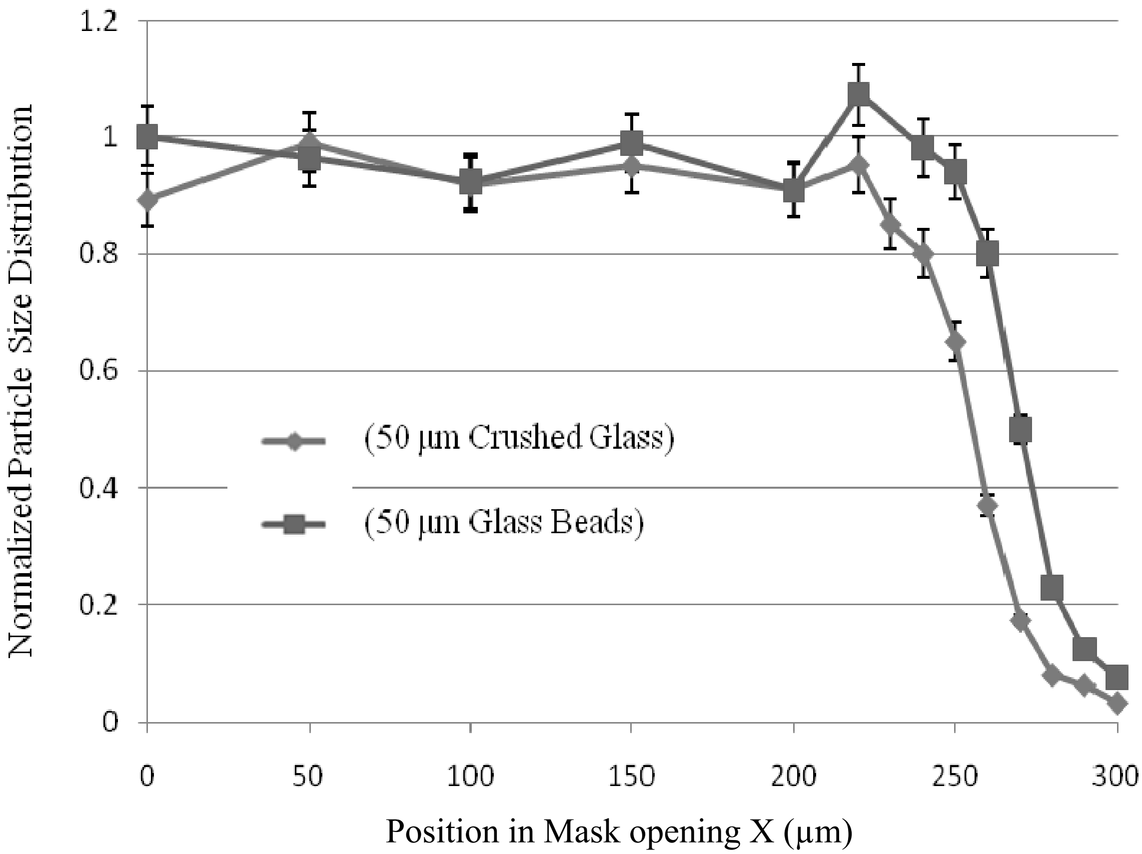

Figure 4.22: Normalized particle size distribution inside the mask opening using 50µm spherical and non-spherical glass media. The plot symbols are the measured quantities. Only half the symmetrical mask opening width is shown. A zero position indicates the center of the mask opening (Fig. 4.14). Error bars represent the sample standard deviations.

4.4. Particle mass distribution within the mask opening

4.4.1. Measured values

The normalized measured distributions of mass flux through the mask opening shown in Figs. 4.23 to 4.28 were determined using the following procedure: The mask opening width was divided up into 10 μm wide bins. The approximate mass of particles in a given bin was determined as the sum of the particle masses detected within the bin, based on the known particle material density, and the equivalent particle diameter, as measured by shadowgraphy for each individual particle. The particle mass in each bin across the opening width were then normalized by the mass at the center of the channel. Measurements from both sides of the symmetrical mask opening, i.e. at corresponding x_1 and x_2's in Fig. 4.14 were averaged to effectively double the sample size.

The distribution of particle mass flux for the masked experiments in Table 3.3 showed a relatively constant value at the center of the mask opening, and decreases of the mass flux near the mask edges.

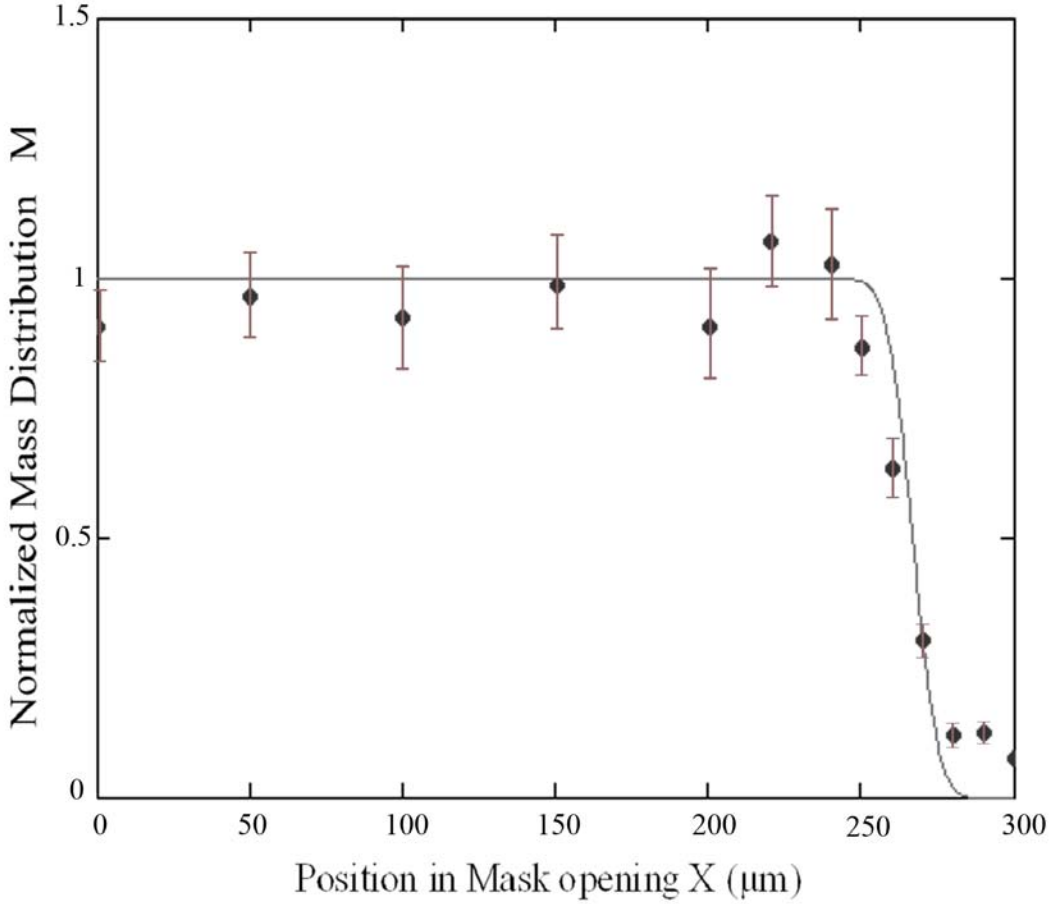

Figure 4.23: Particle mass distribution inside the mask opening, using 50 µm glass beads. Lines are the predictions of eq. (5.2), using the normal size distributions in Fig. 4.12. The plot symbols are the measured quantities. Only half the symmetrical mask opening width is shown. A zero position indicates the center of the mask opening (Fig. 4.14). Error bars represent the sample standard deviations.

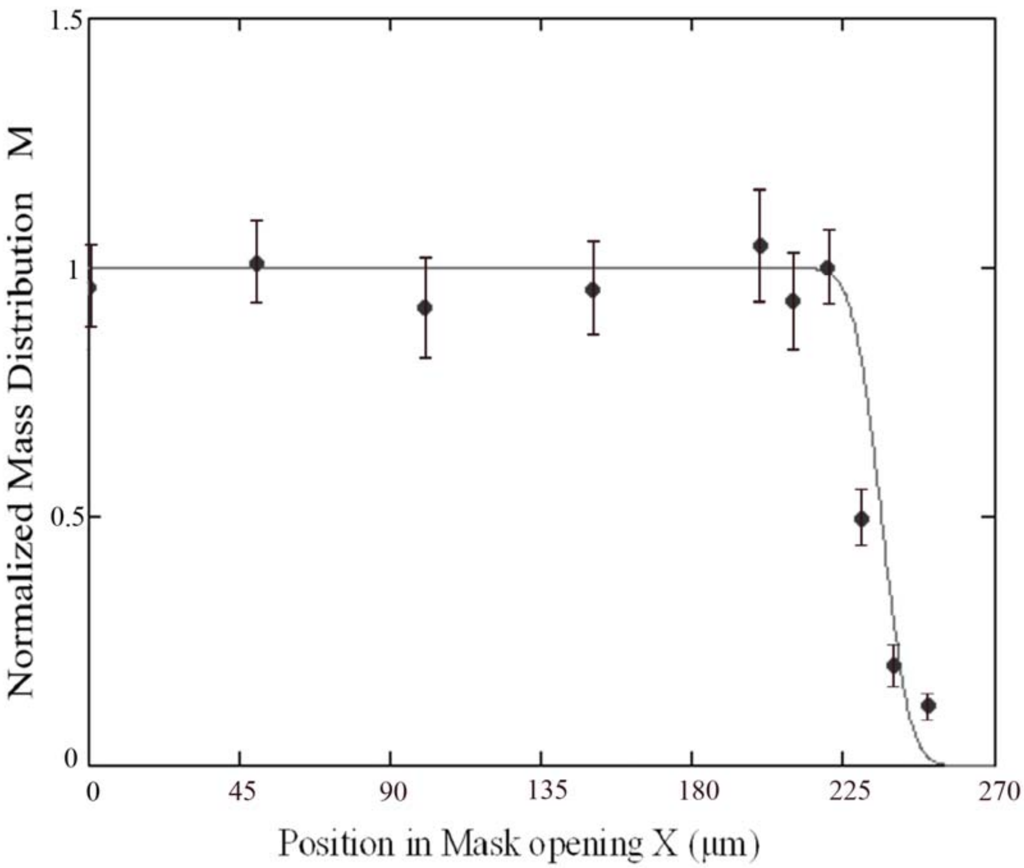

Figure 4.24: Particle mass distribution inside the mask opening, using 50μm stainless steel beads. Lines are the predictions of eq. (5.2), using the normal size distributions in Fig. 4.12. The plot symbols are the measured quantities. Only half the symmetrical mask opening width is shown. A zero position indicates the center of the mask opening (Fig. 4.14). Error bars represent the sample standard deviations.

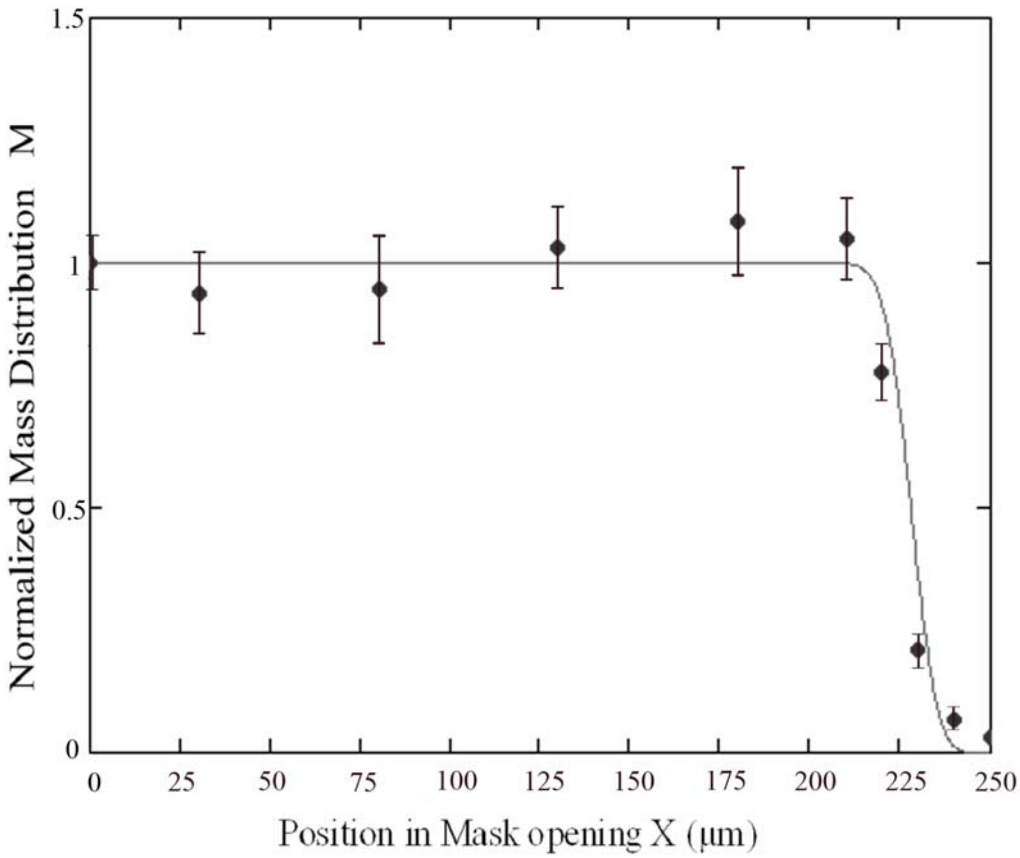

Figure 4.25: Particle mass distribution inside the mask opening, using 35 μm glass beads. Lines are the predictions of eq. (5.2), using the normal size distributions in Fig. 4.12. The plot symbols are the measured quantities. Only half the symmetrical mask opening width is shown. A zero position indicates the center of the mask opening (Fig. 4.14). Error bars represent the sample standard deviations.

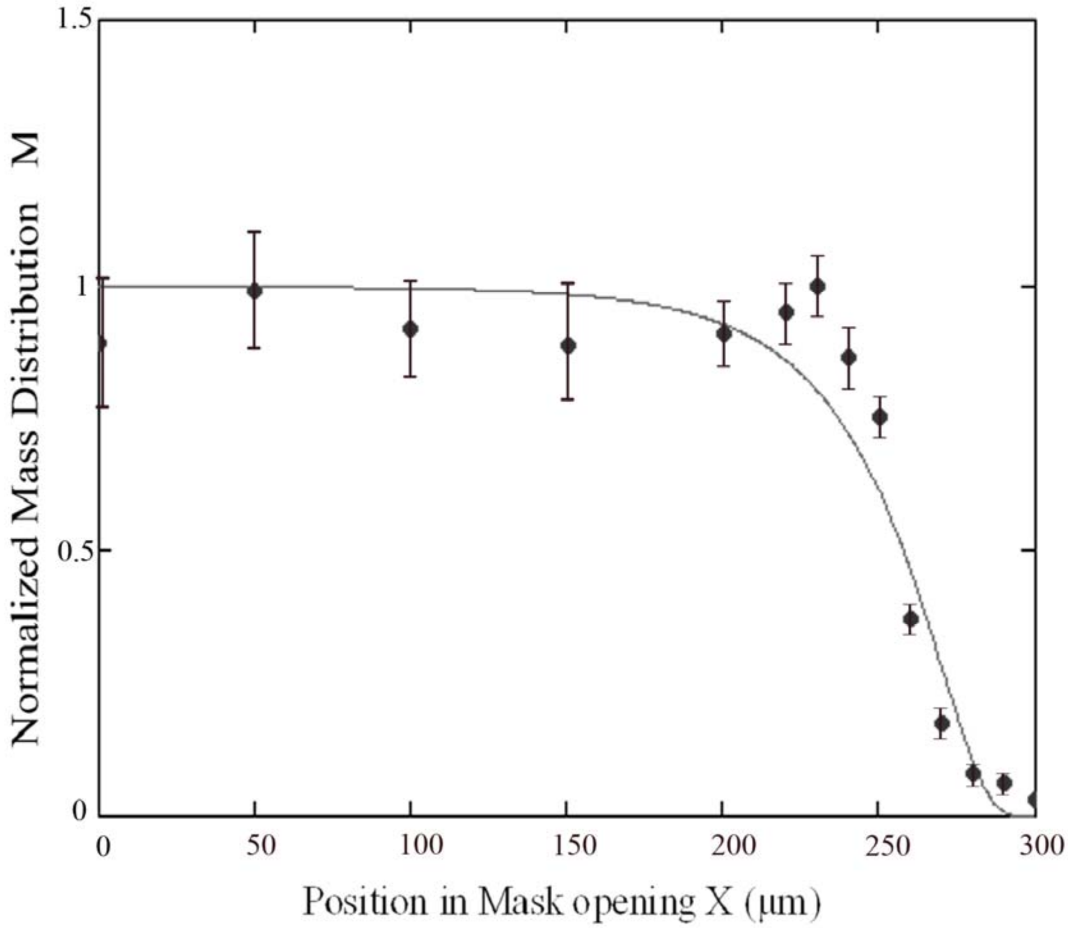

Figure 4.26: Particle mass distribution inside the mask opening using 50 μm crushed glass. Lines are the predictions of eq. (5.2), using the log-normal size distributions in Fig. 4.13. The plot symbols are the measured quantities. Only half the symmetrical mask opening width is shown. A zero position indicates the center of the mask opening (Fig. 4.14). Error bars represent the sample standard deviations.

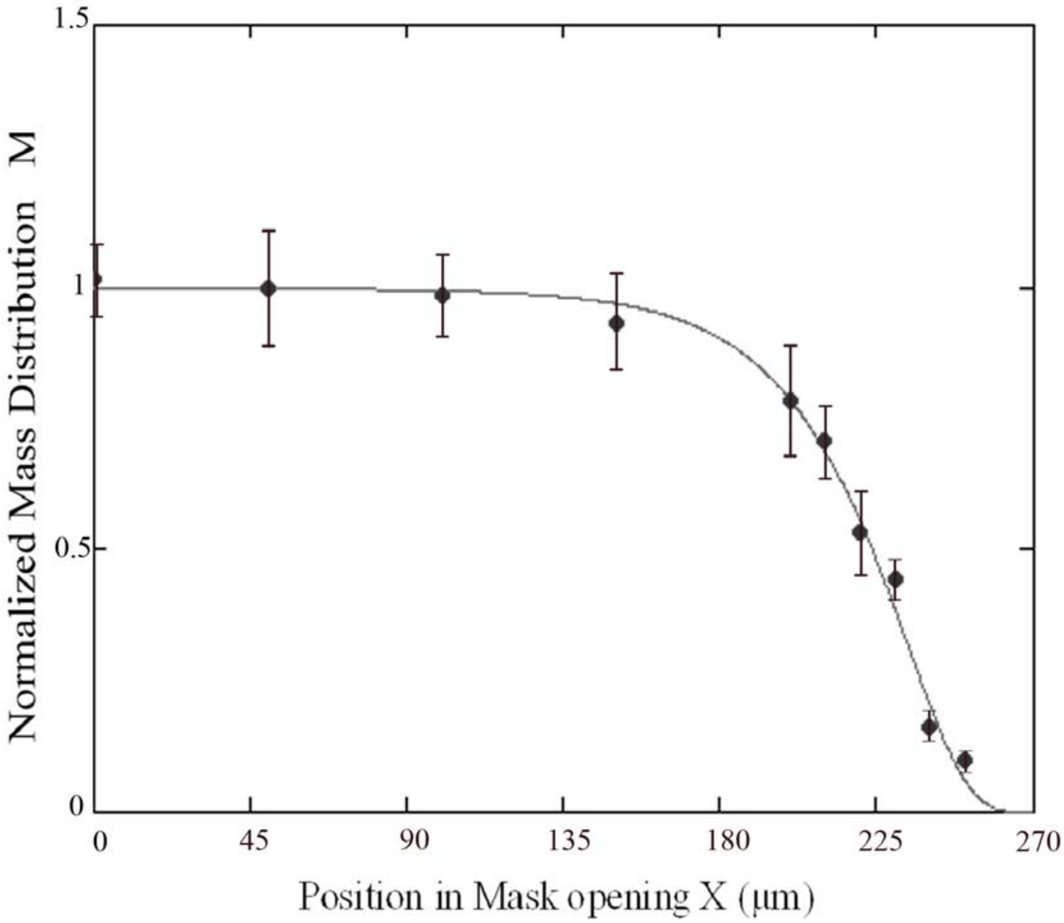

Figure 4.27: Particle mass distribution inside the mask opening using 50µm stainless steel grit. Lines are the predictions of eq. (5.2), using the log-normal size distributions in Fig. 4.13. The plot symbols are the measured quantities. Only half the symmetrical mask opening width is shown. A zero position indicates the center of the mask opening (Fig. 4.14). Error bars represent the sample standard deviations.

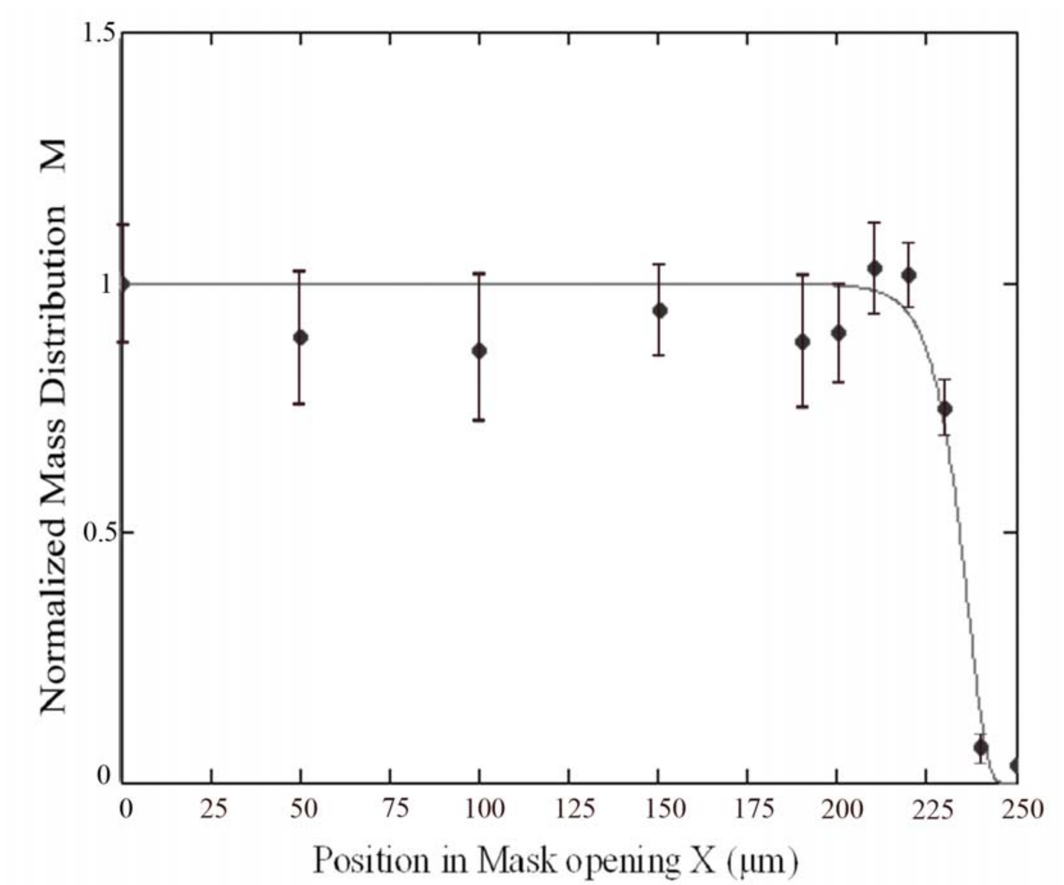

Figure 4.28: Particle mass distribution inside the mask opening using 25μm aluminum oxide. Lines are the predictions of eq. (5.2), using the log-normal size distributions in Fig. 4.13. The plot symbols are the measured quantities. Only half the symmetrical mask opening width is shown. A zero position indicates the center of the mask opening (Fig. 4.14). Error bars represent the sample standard deviations.

The slope of the mass flux distribution at the mask edge thus depends on the particle size distribution. The use of spherical particles (Figs. 4.23 and 4.24) that have a relatively uniform particle size distribution (Figs. 4.12a and 4.12b) near the mean with relatively few small particles will result in a mass flux that abruptly decreases approximately one particle radius from the mask edge. The use of angular particles of similar size (Figs. 4.26 and 4.27), which contain a wider range of particle sizes (Figs. 4.13a and 4.13b), results in a more gradual and smoother decrease in mass flux as the mask edge is approached, since the small particles in the powder can arrive close to the mask edge (Figs. 4.15 to 4.20). The effect of particle size distribution on mass flux distribution through the mask has been previously modeled by Ghobeity et al. [6].

4.4.2. Comparison to model of Ghobeity et al. [6]

The analytical model of Ghobeity et al. [6] predicts that the particle mass flux distribution through the mask opening is a function of the mask width and the particle size distribution. The present work is the first to attempt to assess the validity of this model through direct measurements within the mask opening. Since the particle shape was found to have a strong effect on size uniformity, the predictions of this model were compared to the measured particle sizes for spherical and non-spherical particles.

Ghobeity et al. [6] assumed that the probability of particles passing through the mask opening decreases dramatically as the mask edge is approached, since only progressively smaller particles can pass through the opening without striking the edge as it is approached (Fig. 4.14).

The analytical model they developed based on this assumption expresses the proportion of the total number of particles incident to the mask opening that pass through and arrive to the surface at a given location between x and $x + dx$, as:

$$P_s(x) = \int_0^{(W/2)-|x|} P(r)dr \tag{4.5}$$

where *P(r)* is the probability density function that describes the distribution of particle sizes (assumed spherical with radius, r) and W is the mask opening width [6]. Accordingly, the probability of the particles passing through the centre of the mask opening at x=0 is much higher than near the sides ($x \rightarrow W/2$). Based on this, Ghobeity et al. derived an expression for $M^*(r)$, the normalized distribution mass of particles through the mask opening, i.e. the mass of particles at a given x divided by the mass of particles at x=0, as:

$$M^*(x) = \frac{\int_0^{\frac{W}{2}-|x|} r^3 P(r)dr}{\int_0^{\frac{W}{2}} r^3 P(r)dr} \tag{4.6}$$

Figs. 4.12 and 4.13 show the measured particle size distributions incident to the mouth of the mask opening for the particles in Table 3.1, together with the appropriate curve fits. These measured size distributions were in equation (5.2) to predict the mass distribution, and the results are compared to the shadowgraphy measurements in Figs. 4.15 to 4.20. There is a very good agreement of the model-predicted and measured normalized mass flux distributions across the mask width in all cases, and even near the mask edges where the decreases in flux are expected to have the greatest effect on the surface evolution. The model is able to effectively capture the effect of particle size distribution discussed in Section 4.3.

It is interesting to note that, although the model of Ghobeity et al. [6] uses equivalent spherical diameter particles for angular particles, the predictions of the model are nevertheless in excellent agreement with experiments. This useful result implies that the particle mass distribution through the mask only depends on the size distribution, and not the shape of particles.

4.5. Limitations on applicability of results:

The results of the present study directly show that, if the particle size distribution is measured, under the present blasting conditions, the model of Ghobeity et al. [6] can be used with confidence in surface evolution models in order to predict the size and shape of features machined using AJM. However, there are some factors that should be considered when assessing the generality of the results.

The mask openings that were used in the present experiments were open, allowing particles to freely exit the mask opening. In an actual AJM application, the target substrate would be present at the exit, causing particles to ricochet from the surface back into the mask. However, using a particle tracking model [20], the mass flux used in typical AJM applications (between 2-4 g/min through a 0.76 mm nozzle), has been previously shown [26] to be sufficiently low that interference between incident and rebounding particles is highly unlikely even in the free jet case. At higher fluxes, where the interference becomes significant, the model of Ghobeity et al. [6] and the conclusions of the present study may not be applicable.

The presence of a surface at the exit of the mask opening might also be expected to affect the velocity and distribution of the particles through the mask opening due to aerodynamic effects. However, this is also not likely to be significant because of the relatively large distance from the nozzle exit (20 mm) where the air velocity is likely very small. For example, for the case of experiment # 5a, the model of Li et al. [5] predicts that the particle velocity is over twice the air velocity 20 mm away from the nozzle. The Stoke number is a dimensionless number which can be also used to study the behavior of particles floating in the air flow. However, for Stoke numbers smaller than 1 the particles follow fluid streamlines closely and for the value greater than 1, particles will detach from a flow especially where the flow velocity decreases rapidly. Previous analysis has shown that the Stokes number for typical AJM particles is on the order of 50-450 [26], i.e., much greater than 1, so that it is unlikely that any deflection in the air jet due to the presence of the surface at the exit would have significantly affected the particle trajectories. In situations where the Stokes number is less than 1 (e.g., using very small particles), these effects may become significant.

CHAPTER 5

Summary, Contributions and Recommendations for Future Work

5.1. Summary and contributions

A shadowgraphic method was used to measure the particle velocity and size distributions using both angular and spherical erosive media in both a free jet and through a mask opening typical of that used in AJM applications. To the knowledge of the author, this is the first time that shadowgraphic methods have been used to measure particle velocities in a free jet typical of that used in AJM. It is also the first time that any technique has been used to measure particle size and velocity through a mask opening. Such measurements are important for determining the inputs to surface evolution models that can be used to predict the size and shape of micro-channels and micro-holes machined using AJM. The important findings and contributions can be summarized as follows:

(i) The free jet experiments demonstrated that the particle shape (sphericity) strongly affects the particle velocities. Using an improved drag coefficient correlation that accounted for the particle sphericity in the analytical model of Ref. [5] resulted in quite accurate predictions of measured velocity distributions across a free jet for both angular and spherical particles.

(ii) The velocity through narrow mask openings was found to be constant across the opening width but significantly lower than that in the free jet. A reduced etched rate from that found when machining with free jets can thus be expected when micro-machining through masks.

(iii) No correlation was found between the particle size and position within the free jet.

(iv) The powder size distributions measured using shadowgraphy in the free jet were used as inputs to the analytical model of Ghobeity et al. [6] to determine the mass flux distribution through the mask opening. The resulting predictions of the model were in excellent agreement with the shadowgraphy measured particle mass flux distribution profiles through the mask opening. It can thus be concluded that the analytical model of Ref. [6] can be used effectively in surface evolution models to predict the mass flux incident to the surface through the mask. Experimental results for both spherical and non-spherical particles also demonstrated that the size distribution and uniformity of particles can greatly affect the mass distribution profile.

(v) Very few particles were found to ricochet from the edge of the mask, and the ones that did carried very low kinetic energies, and are thus unlikely to significantly contribute to erosion. Under the present conditions, the particle mass flux due to the ricochet of particles from the edge of the mask can thus be considered negligible for the purposes of modeling surface evolution in AJM.

5.2. Recommendations for future work

The presented work only considered jets incident perpendicular to the mask opening at a constant standoff distance of 20 mm. The mask openings that were used in all experiments were open at the exit. However, in an actual AJM application, the target substrate would be present at the exit and this will cause the particles to ricochet from the surface back into the mask. The following points may be regarded as first steps towards continuation of the present work.

(i) Add a target substrate at the exit of the mask opening and investigate the influence of the particle ricochet from the surface back into the mask opening. Subsequently, study the effect of the target surface on the velocity and mass flux distribution of the particles inside the mask opening.

(ii) Investigate the influence of different angles of incidence (other than 90º) on the resulting velocity, size and spatial distribution of the particles inside the mask opening. This would be useful to provide inputs for AJM surface evolution models that would be used to predict the shape of micro-features machined with inclined abrasive jets. Such configurations are useful to sculpt three dimensional suspended micro-features.

(iii) Investigate the effect of different mask plate thicknesses and its possible influence on the particle size and, consequently, mass distribution inside the mask opening.

(iv) Study the coefficients of restitution for ricocheting particles and their influences on the mass distribution profile of abrasive powders within the mask opening area and particularly near the sidewalls.

(v) Examine the interference between incident and rebounding particles by applying the higher particle mass fluxes through the air jet and study the effect of this factor in particle velocity and size distributions inside the mask opening.

Appendix A

MATERIAL SAFETY DATA SHEET

FLAMMABILITY 0
HEALTH 1
REACTIVITY 0
HAZARD RATING (NFPA)

SECTION I IDENTIFICATION

Manufacturer: Comco Inc.
2151 N. Lincoln St., Burbank, CA 91504
Chemical Name: Aluminum Oxide
Chemical Family: Metal Oxide (refractory)
Part Numbers: PD1001, PD1009, PD1012, PD1014, PD1034 (plus dash no's of each)

Emergency Telephone No: (818) 841-5500
Document No.: SD1001, Rev E Issue Date: March 2011
Trade Name: A, J, N, SB, V
Formula: Al_2O_3

SECTION II COMPOSITION

Component	%	CAS#	OSHA Exp	TLV	Carcinogen
Aluminum Oxide	94.2	1344-28-1	15 mg/m^3	10 mg/m^3	No
Titanium Oxide	4.0	13463-67-7	Same	Same	No
Impurities (Oxides)	Balance				

SECTION III PHYSICAL AND CHEMICAL DATA

Boiling Pt.: N/A	Softening Pt: 1900°C	Specific Gravity: 3.9
Vapor Pressure: N/A	Percent Volatile: N/A	Vapor Density: N/A
Evap. Rate: N/A	Sol. in Water: N/A	Sol. in Alcohol: N/A

Solubility in other Solvent: N/A
Appearance and Odor: Granular powder, brownish color, odorless

SECTION IV FIRE AND EXPLOSION HAZARD DATA

Flash Point: N/A	Method Used: N/A
Explosion Potential: N/A	Flammable Limits: LEL: N/A UEL: N/A
Extinguishing Media: N/A	Special Fire Fighting Procedures: N/A

SECTION V HEALTH, FIRST AID, AND MEDICAL DATA

Risk:	Inhalation of dust, dust in eyes
Acute Health Effects:	May cause coughing, shortness of breath
Chronic Health Effects:	May affect breathing capacity
First Aid Procedures:	Remove to fresh air. Apply artificial respiration if needed. Wash eyes with warm water if required. Obtain medical help

SECTION VI CORROSIVITY AND REACTIVITY DATA

Stability: Stable	Polymerization: N/A	Incompatibility: N/A
Decomposition Products: N/A	Conditions to be Avoided: N/A	

SECTION VII STORAGE, HANDLING, AND USE PROCEDURES

Normal Storage and Handling:	Use adequate ventilation for nuisance dust
Normal Use:	Same as above; avoid excessive dusting
In Case of Spills:	Same as above; use dust masks
Waste Disposal:	Standard landfill methods, when in pure (as supplied) state

SECTION VIII PERSONAL PROTECTION INFORMATION

Respiratory Protection:	Approved NIOSH dust mask if recommended exposure limits are exceeded
Ventilation:	Local exhaust
Eye Protection:	NIOSH goggles recommended
Gloves:	If desired by user
Other:	N/A

SECTION IX SPECIAL PRECAUTIONS

No special precautions required

Comco Inc. 2151 N. Lincoln Street / Burbank CA 91504-3344, USA / 818-841-5500
E-mail: tech@COMCOinc.com / Fax: 818-955-8365 / www.COMCOinc.com

COMCO INC. 800-796-6626

Figure A 1: Material safety data sheets (MSDS) for Aluminum Oxide type of A, SB, J, N and V provided by Comco Inc. typically used for 25µm Al_2O_3

MATERIAL SAFETY DATA SHEET

FLAMMABILITY 0
HEALTH 1
REACTIVITY 0
HAZARD RATING (NFPA)

SECTION I IDENTIFICATION

Manufacturer: Comco Inc.
2151 N. Lincoln St., Burbank, CA 91504
Chemical Name: Aluminum Oxide
Chemical Family: Metal Oxide (refractory)
Part Numbers: PD1003, PD1029 (plus dash no's of each)

Emergency Telephone No: (818) 841-5500
Document No.: SD1003, Rev D Issue Date: March 2011
Trade Name: C, S
Formula: Al_2O_3

SECTION II COMPOSITION

Component	%	CAS#	OSHA Exp	TLV	Carcinogen
Aluminum Oxide	99+	1344-28-1	15 mg/m^3	10 mg/m^3	No
Impurities (Oxides)	Balance				

SECTION III PHYSICAL AND CHEMICAL DATA

Boiling Pt.: N/A
Vapor Pressure: N/A
Evap. Rate: N/A
Softening Pt: 2072°C
Percent Volatile: N/A
Sol. in Water: N/A
Specific Gravity: 3.95
Vapor Density: N/A
Sol. in Alcohol: N/A
Solubility in other Solvent: N/A
Appearance and Odor: Granular powder, white color, odorless

SECTION IV FIRE AND EXPLOSION HAZARD DATA

Flash Point: N/A
Explosion Potential: N/A
Extinguishing Media: N/A
Method Used: N/A
Flammable Limits: LEL: N/A UEL: N/A
Special Fire Fighting Procedures: N/A

SECTION V HEALTH, FIRST AID, AND MEDICAL DATA

Risk: Inhalation of dust, dust in eyes
Acute Health Effects: May cause coughing, shortness of breath
Chronic Health Effects: May affect breathing capacity
First Aid Procedures: Remove to fresh air. Apply artificial respiration if needed. Wash eyes with warm water if required. Obtain medical help

SECTION VI CORROSIVITY AND REACTIVITY DATA

Stability: Stable
Decomposition Products: N/A
Polymerization: N/A
Conditions to be Avoided: N/A
Incompatibility: N/A

SECTION VII STORAGE, HANDLING, AND USE PROCEDURES

Normal Storage and Handling: Use adequate ventilation for nuisance dust
Normal Use: Same as above; avoid excessive dusting
In Case of Spills: Same as above; use dust masks
Waste Disposal: Standard landfill methods, when in pure (as supplied) state

SECTION VIII PERSONAL PROTECTION INFORMATION

Respiratory Protection: Approved NIOSH dust mask if recommended exposure limits are exceeded
Ventilation: Local exhaust
Eye Protection: NIOSH goggles recommended
Gloves: If desired by user
Other: N/A

SECTION IX SPECIAL PRECAUTIONS

No special precautions required

Comco Inc. 2151 N. Lincoln Street / Burbank CA 91504-3344, USA / 818-841-5500
E-mail: tech@COMCOinc.com / Fax: 818-955-8365 / www.COMCOinc.com

COMCO INC. 800-796-6626

Figure A 2: Material safety data sheets (MSDS) for Aluminum Oxide type of C or S provided by Comco Inc. typically used for 50µm Al_2O_3

MATERIAL SAFETY DATA SHEET

FLAMMABILITY
HEALTH REACTIVITY
HAZARD RATING (NFPA)

SECTION I IDENTIFICATION

Manufacturer: Comco Inc.
2151 N. Lincoln St., Burbank, CA 91504
Chemical Name: Soda-Lime Glass
Chemical Family: Glass Oxide
Part Numbers: PD1004, PD1030, PD1033 (plus dash no's of each)

Emergency Telephone No: (818) 841-5500
Document No.: SD1004, Rev D Issue Date: Nov. 2007
Trade Name: D, T, X
Formula: SiO_2

SECTION II COMPOSITION

Component	%	CAS#	OSHA Exp	TLV	Carcinogen
Glass Oxide	100	65997-17-3			
Nuisance Dust			15 mg/m^3	10 mg/m^3	Not Listed
Nuisance Dust, Respirable Fraction			5 mg/m^3	5 mg/m^3	Not Listed

SECTION III PHYSICAL AND CHEMICAL DATA

Boiling Pt.: N/A
Vapor Pressure: N/A
Evap. Rate: N/A

Softening Pt: 730°C
Percent Volatile: N/A
Sol. in Water: N/A

Specific Gravity: 2.46-2.49 g/cc
Vapor Density: N/A
Sol. in Alcohol: N/A

Solubility in other Solvent: Soluble in Hydrofluoric Acid
Appearance and Odor: Granular powder, white color, odorless

SECTION IV FIRE AND EXPLOSION HAZARD DATA

Flash Point: N/A — Method Used: N/A
Explosion Potential: N/A — Flammable Limits: LEL: N/A UEL: N/A
Extinguishing Media: N/A — Special Fire Fighting Procedures: N/A

SECTION V HEALTH, FIRST AID, AND MEDICAL DATA

Risk: Inhalation of dust, dust in eyes
Acute Health Effects: May cause coughing, shortness of breath
Chronic Health Effects: May affect breathing capacity
First Aid Procedures: Remove to fresh air. Apply artificial respiration if needed. Wash eyes with warm water if required. Obtain medical help

SECTION VI CORROSIVITY AND REACTIVITY DATA

Stability: Stable
Decomposition Products: N/A

Polymerization: N/A
Conditions to be Avoided: N/A

Incompatibility: Hydrofluoric Acid

SECTION VII STORAGE, HANDLING, AND USE PROCEDURES

Normal Storage and Handling: Use adequate ventilation for nuisance dust
Normal Use: Same as above; avoid excessive dusting
In Case of Spills: Same as above; use dust masks
Waste Disposal: Standard landfill methods, when in pure (as supplied) state

SECTION VIII PERSONAL PROTECTION INFORMATION

Respiratory Protection: Approved NIOSH dust mask if recommended exposure limits are exceeded
Ventilation: Local exhaust
Eye Protection: NIOSH goggles recommended
Gloves: If desired by user
Other: N/A

SECTION IX SPECIAL PRECAUTIONS

No special precautions required

Comco Inc. 2151 N. Lincoln Street / Burbank CA 91504-3344, USA / 818-841-5500
E-mail: tech@COMCOinc.com / Fax: 818-955-8365 / www.COMCOinc.com
COMCO INC. 800-796-6626

Figure A 3: Material safety data sheets (MSDS) for glass beads provided by Comco Inc.

MATERIAL SAFETY DATA SHEET

FLAMMABILITY
HEALTH REACTIVITY
HAZARD RATING (NFPA)

SECTION I IDENTIFICATION

Manufacturer: Comco Inc.
2151 N. Lincoln St., Burbank, CA 91504
Chemical Name: Crushed Soda-Lime Glass
Chemical Family: Glass, Oxide
Part Numbers: PD1027 (plus dash no's of each)

Emergency Telephone No: (818) 841-5500
Document: SD1002, Rev D Issue Date: Nov. 2007
Trade Name: K
Formula: SiO_2

SECTION II COMPOSITION

Component		%	CAS#	OSHA Exp	TLV	Carcinogen
Glass, Oxide		100	65997-17-3	15 mg/m^3	10 mg/m^3	No
Consisting of:	Silicon Dioxide	72.5	7631-86-9			
	Calcium Oxide	9.8	1305-78-8			
	Sodium Oxide	13.7	1313-59-3			
	Free Silica	None (all components are amorphous/non-crystalline)				

SECTION III PHYSICAL AND CHEMICAL DATA

Boiling Pt.: N/A
Vapor Pressure: N/A
Evap. Rate: N/A

Softening Pt: 730°C
Percent Volatile: N/A
Sol. in Water: N/A

Specific Gravity: 2.46-2.49 g/cc
Vapor Density: N/A
Sol. in Alcohol: N/A

Solubility in other Solvent: Soluble in Hydrofluoric Acid
Appearance and Odor: Fine granular powder, white color, odorless

SECTION IV FIRE AND EXPLOSION HAZARD DATA

Flash Point: N/A
Explosion Potential: N/A
Extinguishing Media: N/A

Method Used: N/A
Flammable Limits: LEL: N/A UEL: N/A
Special Fire Fighting Procedures: N/A

SECTION V HEALTH, FIRST AID, AND MEDICAL DATA

Risk: Inhalation of dust, dust in eyes
Acute Health Effects: May cause coughing, shortness of breath
Chronic Health Effects: May affect breathing capacity
First Aid Procedures: Remove to fresh air. Apply artificial respiration if needed. Wash eyes with warm water if required. Obtain medical help

SECTION VI CORROSIVITY AND REACTIVITY DATA

Stability: Stable
Decomposition Products: N/A

Polymerization: N/A
Conditions to be Avoided: N/A

Incompatibility: Hydrofluoric Acid

SECTION VII STORAGE, HANDLING, AND USE PROCEDURES

Normal Storage and Handling: Use adequate ventilation for nuisance dust
Normal Use: Same as above; avoid excessive dusting
In Case of Spills: Same as above; use dust masks
Waste Disposal: Standard landfill methods, when in pure (as supplied) state

SECTION VIII PERSONAL PROTECTION INFORMATION

Respiratory Protection: Approved NIOSH dust mask if recommended exposure limits are exceeded
Ventilation: Local exhaust
Eye Protection: NIOSH goggles recommended
Gloves: If desired by user
Other: N/A

SECTION IX SPECIAL PRECAUTIONS

No special precautions required

Comco Inc. 2151 N. Lincoln Street / Burbank CA 91504-3344, USA / 818-841-5500
E-mail: tech@COMCOinc.com / Fax: 818-955-8365 / www.COMCOinc.com
COMCO INC.
800-796-6626

Figure A 4: Material safety data sheets (MSDS) for crushed glass provided by Comco Inc.

VULKAN BLAST SHOT TECHNOLOGY
10 Plant Farm Blvd., Unit 2
Brantford, Ontario N3S 7W3
Phone: (519) 753-2226 Fax (519) 759-8472
www.vulkanshot.com e-mail: vulkan@vulkanshot.com

Material Safety Data Sheet CHRONITAL

Revision Date: February 1, 2011

1 Material / Preparation and Company Name

1.1 Specifications of the material / preparation

1.1.1 Type of Product
Alloyed Chrome-Nickel-Steel

1.1.2 Product name
CHRONITAL, rust-resistant, cast stainless steel abrasive

1.1.3 Trade name
CHRONITAL

1.2 Specifications of the manufacturer / importer / supplier

1.2.1 manufacturer / importer / supplier
Vulkan Blast Shot Technology

1.2.2 Company address
10 Plant Farm Blvd., Unit 2, Brantford, Ontario Canada N3S 7W3

1.2.3. Place of business / postal address / country code / ZIP code / city
10 Plant Farm Blvd., Unit 2
Brantford, Ontario Canada N3S 7W3

1.2.4 Telephone
519-753-2226 or 1-800-263-7674 (U.S. and Canada)

1.2.5 Facsimile
519-759-8472

1.2.6 For further information, please contact
Quality Assurance Department

1.2.7 Emergency number
519-753-2226

2 Composition / Indication of Constituents

2.1 Chemical characterisation of the preparation
Iron-chromium-nickel-carbon alloy
Approx. main components:

Fe:	69 %
Cr:	16-20 % (metallic Chrome)
Cr^{6+}:	0,00 % (Chrome (VI), Hexavalent Chrome)
Ni:	8-10 %
C:	0.2 %
Mn:	1.2 %
Si:	2 %

Figure A 5: Material safety data sheets (MSDS) for Chronital stainless steels provided by Vulkan Blast Shot Technology

2.2 Specifications with regard to the preparation

CAS – No.	Name of material	Percentage Value	Danger Code	„R" clauses	„S" Clauses
7440-02-0	Nickel	Approx. 10 %	Xn	11;40;43	2,22;36

2.3 Additional Notes concerning item 2.2

The product exists in the form of a solid metallic bond ensuring that nickel, as a possible hazardous material, does not have any effect. In the form in which it enters into circulation and is used, it does not present any health hazard.

3 Possible Risks

3.1 Designation of risks

During mechanical application (i.e in blasting plants) dust and vapour may occur. The usual precautions should be taken. The statutory limit values for dust and vapour have to be adhered to.

4 First - Aid Measures

4.1 General Notes

First - aid measures only refer to dust.

4.1.1 Measures in case of inhaling

Ensure sufficient fresh air supply, and consult and physician, if necessary.

4.1.2 Measures in case of eye contact

Rinse your eyes with plenty of water; consult and physician, if necessary.

5 Fire - Fighting Measures

not applicable (n.a.)

6 Measures to be taken in case of unintended release

not applicable (n.a.)

7 Handling and Storage

7.1 Handling

no danger

7.2 Storage

no danger

8 Restriction of Exposure and Personal Protective Equipment

8.1 Additional notes regarding the configuration of technical plants

cf. Item 3.1

8.2 Constituents with workplace - specific limiting values to be controlled

Limiting values are only defined for the elements contained in steel, e.g. for Ni, Cr, Mn, whereas no such limits have been established for steel, as such.

Figure A 6 (continued): Material safety data sheets (MSDS) for Chronital stainless steels provided by Vulkan Blast Shot Technology

8.3	**Personal protective equipment** Standard equipment for processing of metals. Dust and vapour have to be maintained below the statutory limits by providing adequate suction facilities.	

9 Physical and Chemical Properties

9.1	**Appearance**	
9.1.1	**State**	solid
9.1.2	**Colour**	silver-grey, metallic
9.1.3	**Odour**	odourless
9.2	**Safety-relevant data**	n.a.
9.2.1	**pH - value**	n.a.
9.2.2	**Change of state**	n.a.
9.2.2.1	**Boiling point**	n.a.
9.2.2.2	**Melting point**	1.400 - 1.550 °C
9.2.3	**Flash point**	n.a.
9.2.4	**Inflammability**	n.a.
9.2.5	**Ignition temperature**	n.a.
9.2.6	**Self-inflammability**	n.a.
9.2.7	**Fire promoting properties**	n.a.
9.2.8	**Explosion limits**	n.a.
9.2.9	**Vapour pressure at.... °C**	n.a.
9.2.10	**Density at 20°C**	7,7 - 8,1 g/cm^3
9.2.11	**Solubilizing properties and distribution**	
9.2.11.1	**Water-Solubility**	insoluble
9.2.11.2	**Fat-Solubility**	n.a.
9.2.11.3	**Distribution coefficient**	n.a.

10 Stability and Reactivity

stable and non-reactive

11 Indications Concerning Toxicology

The steel contains nickel (classified as a hazardous material), chromium and manganese (with limited values to be controlled). In its usual solid state, and on condition of a usual industrial application, the steel can neither be inhaled nor be in permanent or long lasting contact with the skin.

11.1	**Results of toxicological tests**	
11.1.1	**Acute toxicity**	n.a.
11.1.1.1	**Acute toxicity oral**	n.a.
11.1.1.2	**Acute toxicity, when inhaled**	none
11.1.1.3	**Acute toxicity, dermal**	none
11.1.2.	**Irritant – caustic effect**	none
11.1.2.1	**Irritant – caustic effect on skin**	none
11.1.2.2	**Irritant – caustic effect on eyes**	n.a.
11.1.3	**Sensitization**	none
11.1.4	**Effects after repeated or extended exposure**	

Figure A 7 (continued): Material safety data sheets (MSDS) for Chronital stainless steels provided by Vulkan Blast Shot Technology

11.1.5	**Subacute effects**	none
11.1.5.1	**Subchronic effects**	none
11.1.5.2	**Chronic effects**	none
11.1.5.3	**Specific effects**	none
11.1.5.3.1	**Carcinogenic effects**	none

11.2 Experience from practical application

11.2.1 Classification-relevant observations

A carcinogenic effect by manufacture, use, processing or machining of special steel could neither be proved in epidemiologic studies nor in the scope of experiments on animals.

11.2.2 Other Observations

The experience made for decades in the scope of a variety of applications has shown that this steel, in particular stainless steel is to be regarded as an extremely resistant and perfectly hygienic material.

11.3 General Notes

none

12 Notes Regarding Ecology

not water-soluble, no precautions required.

13 Notes Regarding Utilization and Disposal

Waste and scrap constitute valuable materials, which can easily be disposed, since new products of high value can be produced by means of recycling.

14 Notes Regarding Transport

not classified as hazardous material in the sense of transport regulations.

15 Regulations

15.1 Identification according to Ri67/548/EWG

15.1.1 Code (cf. items 2,3 and 4)

Xn for nickel

15.1.2 Danger designation for nickel (cf. items 2,3 and 4)

Slightly toxious

15.1.3 R clauses for nickel (cf. items 2,3 and 4)

11 easy inflammability
40 irreversible injury possible
43 potential sensitization by skin contact

15.1.4 S clauses for nickel (cf. items 2, 3 and 4)

2 not for children's hands
22 do not inhale dust
36 always wear adequate protective clothing during processing

Figure A 8 (continued): Material safety data sheets (MSDS) for Chronital stainless steels provided by Vulkan Blast Shot Technology

15.1.5	**Special marking** n.a.	
15.1.6	**Remarks** Transmission of marking pursuant to Ri67/548/EWG	
15.2	**National Regulations**	
15.2.1	**Regulations** German Chemicals Law, German Ordinance on Hazardous Materials, Federal German Act on Protection against Immissions	
15.2.2	**Additional Notes and Shortcuts** n.a = not applicable	

Declaration: **The indications made in this Safety Data Sheet are based on the present state of our know-how and experience. The Safety Data Sheet describes the products in view of safety requirements. The indications do not constitute any guarantee with regard to product properties and do not create a contractual legal relationship.**

Figure A 9 (continued): Material safety data sheets (MSDS) for Chronital stainless steels provided by Vulkan Blast Shot Technology

VULKAN BLAST SHOT TECHNOLOGY
10 Plant Farm Blvd., Unit 2
Brantford, Ontario N3S 7W3
Phone: (519) 753-2226 Fax (519) 759-8472
www.vulkanshot.com e-mail: vulkan@vulkanshot.com

Material Safety Data Sheet GRITTAL

Revision Date: February 1, 2011

1 Material / Preparation and Company Name

1.1 **Specifications of the material / preparation**

1.1.1 **Type of Product**
Chromium casting alloy

1.1.2 **Product name**
GRITTAL, rust-resistant, cast chromium casting abrasives

1.1.3 **Trade name**
GRITTAL

1.2 **Specifications of the manufacturer / importer / supplier**

1.2.1 **manufacturer / importer / supplier**
Vulkan Blast Shot Technology

1.2.2 **Company address**
10 Plant Farm Blvd., Unit 2, Brantford, Ontario Canada N3S 7W3

1.2.3. **Place of business / postal address / country code / ZIP code / city**
10 Plant Farm Blvd., Unit 2
Brantford, Ontario Canada N3S 7W3

1.2.4 **Telephone**
519-753-2226 or 1-800-263-7674 (U.S. and Canada)

1.2.5 **Facsimile**
519-759-8472

1.2.6 **For further information, pls. contact**
Quality Assurance Department

1.2.7 **Emergency number**
519-753-2226

2 Composition / Indication of Ingredients

2.1 **Chemical characterisation of the preparation**
Iron-chromium-carbon alloy
Main components:

Cr:	30 %	(metallic Chrome)
Cr^{6+}:	0,00 %	(Chrome (VI), Hexavalent Chrome)
Si:	< 2 %	
Mn:	< 2 %	
C:	< 3 %	
Mo:	< 4 %	

Figure A 10: Material safety data sheets (MSDS) for Grittal stainless steels provided by Vulkan Blast Shot Technology

2.2 Hazardous ingredients

This product does not contain any components in concentrations which require a classification as a hazardous substance in accordance with the CE directive.

Carcinogenicity: Not classifiable as to its carcinogenicity to humans

3 Possible Hazards

	Designation of hazards	During mechanical application (i.e in blasting plants) dust and vapour may occur. The usual precautions should be taken. The statutory limit values for dust and vapour have to be adhered to.

4 First - Aid Measures

4.1	**General Notes**	First - aid measures only refer to dust.
4.1.1	**Measures in case of inhaling**	Ensure sufficient fresh air supply, and consult a physician, if necessary.
4.1.2	**Measures in case of eye contact**	Rinse your eyes with plenty of water; consult a physician, if necessary.

5 Fire - Fighting Measures

not applicable (n.a.)

6 Measures to be taken in case of unintended release

not applicable (n.a.)

7 Handling and storage

7.1 Handling

no hazard

7.2 Storage

no hazard

8 Restriction of exposure and personal protective equipment

8.1 Additional notes regarding the configuration of technical plants

see. Item 3.1

8.2 Components with workplace - specific limiting values to be controlled

Limiting values are only defined for pure Chromium and pure Manganese, whereas no such limits exist for steel alloys containing such elements.

8.3 Personal protective equipment

Standard equipment for processing of metals. Dust and vapour have to be maintained below the statutory limits by providing adequate suction facilities.

9 Physical and chemical properties

9.1 Appearance

9.1.1	**State**	solid
9.1.2	**Colour**	dark grey, metallic
9.1.3	**Odour**	odourless

Figure A 11 (continued): Material safety data sheets (MSDS) for Grittal stainless steels provided by Vulkan Blast Shot Technology

9.2	**Safety-relevant data**	n.a.
9.2.1	**pH - value**	n.a.
9.2.2	**Change of state**	
9.2.2.1	**Boiling point**	n.a.
9.2.2.2	**Melting point**	1.400 - 1.550 °C (depending on the alloy)
9.2.3	**Flash point**	n.a.
9.2.4	**Inflammability**	n.a.
9.2.5	**Ignition temperature**	n.a.
9.2.6	**Self-inflammability**	n.a.
9.2.7	**Fire promoting properties**	n.a.
9.2.8	**Explosion limits**	n.a.
9.2.9	**Vapour pressure at.... °C**	n.a.
9.2.10	**Density at 20°C**	481 - 506 lbs/ft^3
9.2.11	**Solubilizing properties and distribution**	
9.2.11.1	**Water-Solubility**	insoluble
9.2.11.2	**Fat-Solubility**	n.a.
9.2.11.3	**Distribution coefficient**	n.a.

10 Stability and Reactivity

stable and non-reactive

11 Indications concerning toxicology

The abrasive bearing the product name GRITTAL has been examined by the BIA (institute of occupational safety affiliated to the German employers' liability insurance association) with regard to the content of silicogenic, toxic and carcinogenic components, and approved as a non-silicogenic material.

12 Notes regarding ecology

not water-soluble, no precautions required.

13 Notes regarding utilization and disposal

Waste and scrap constitute valuable materials, which can easily be disposed, since new products of high value can be produced by means of recycling.

14 Notes regarding transport

not classified as hazardous material in the sense of transport regulations.

15 Regulations

15.1 **identification according to Ri67/548/EWG**

15.1.1 **Code and hazard designation of the product**

n.a.

15.1.2 **R - clauses**

n.a.

15.1.3 **S - clauses**

n.a.

Figure A 12 (continued): Material safety data sheets (MSDS) for Grittal stainless steels provided by Vulkan Blast Shot Technology

16	Other Indications

16.1 References

1) **Abrasives test certificate no. 2002/21840/9311 of 05/23/2002 issued by the institute of occupational safety affiliated to the German employers' liability insurance association.**

Declaration: **The indications made in this Safety Data Sheet are based on the present state of our know-how and experience. The Safety Data Sheet describes the products in view of safety requirements. The indications do not constitute any guarantee with regard to product properties and do not create a contractual legal relationship.**

Figure A 13 (continued): Material safety data sheets (MSDS) for Grittal stainless steels provided by Vulkan Blast Shot Technology

Appendix B

12X Zoom

Performance Specifications

12X Zoom Combinations	W.D.	System Mag.		N.A. -obj-		Feature Size micron		Pixel Size microns		Depth of Field	
Lens Attach. + Prime Lens + Adapter		Low Mag.	High Mag.	Low Mag.	High Mag.	Low Mag.	High Mag.	Low Mag.	High Mag.	Low Mag.	High Mag.
0.25x + 12X Zoom + 0.5x	341	0.07	0.87	0.005	0.025	33.33	6.67	2.33	5.8	20.00	0.80
0.25x + 12X Zoom + 0.67x	341	0.10	1.17	0.005	0.025	33.33	6.67	3.33	7.80	20.00	0.80
0.25x + 12X Zoom + 1.0x	341	0.15	1.75	0.005	0.025	33.33	6.67	5.00	11.67	20.00	0.80
0.25x + 12X Zoom + 1.33x	341	0.19	2.33	0.005	0.025	33.33	6.67	6.33	15.54	20.00	0.80
0.25x + 12X Zoom + 2.0x	341	0.29	3.50	0.005	0.025	33.33	6.67	9.67	23.34	20.00	0.80
0.25x + 12X Zoom + 3.5x	341	0.51	6.13	0.005	0.025	33.33	6.67	16.99	40.88	20.00	0.80
0.5x + 12X Zoom + 0.5x	165	0.14	1.75	0.009	0.051	18.52	3.33	2.59	5.82	6.17	0.19
0.5x + 12X Zoom + 0.67x	165	0.19	2.35	0.009	0.051	18.52	3.33	3.60	7.68	6.17	0.19
0.5x + 12X Zoom + 1.0x	165	0.29	3.50	0.009	0.051	18.52	3.33	5.38	11.45	6.17	0.19
0.5x + 12X Zoom + 1.33x	165	0.39	4.66	0.009	0.051	18.52	3.33	7.22	15.51	6.17	0.19
0.5x + 12X Zoom + 2.0x	165	0.58	7.00	0.009	0.051	18.52	3.33	10.74	22.89	6.17	0.19
0.5x + 12X Zoom + 3.5x	165	1.02	12.30	0.009	0.051	18.52	3.33	18.89	40.95	6.17	0.19
0.75x + 12X Zoom + 0.5x	108	0.22	2.62	0.014	0.076	11.90	2.22	2.61	5.81	2.55	0.09
0.75x + 12X Zoom + 0.67x	108	0.29	3.52	0.014	0.076	11.90	2.22	3.45	7.73	2.55	0.09
0.75x + 12X Zoom + 1.0x	108	0.44	5.25	0.014	0.076	11.90	2.22	5.24	11.52	2.55	0.09
0.75x + 12X Zoom + 1.33x	108	0.58	6.98	0.014	0.076	11.90	2.22	6.90	15.49	2.55	0.09
0.75x + 12X Zoom + 2.0x	108	0.87	10.50	0.014	0.076	11.90	2.22	10.35	23.05	2.55	0.09
0.75x + 12X Zoom + 3.5x	108	1.53	18.40	0.014	0.076	11.90	2.22	18.20	40.84	2.55	0.09
None + 12X Zoom + 0.5x	86	0.29	3.49	0.019	0.101	9.26	1.67	2.68	5.82	1.39	0.05
None + 12X Zoom + 0.67x	86	0.39	4.69	0.019	0.101	9.26	1.67	3.42	7.74	1.39	0.05
None + 12X Zoom + 1.0x	86	0.58	7.00	0.019	0.101	9.26	1.67	5.09	11.55	1.39	0.05
None + 12X Zoom + 1.33x	86	0.77	9.31	0.019	0.101	9.26	1.67	7.13	15.54	1.39	0.05
None + 12X Zoom + 2.0x	86	1.16	14.00	0.019	0.101	9.26	1.67	10.17	23.10	1.39	0.05
None + 12X Zoom + 3.5x	86	2.03	24.50	0.019	0.101	9.26	1.67	18.79	40.91	1.39	0.05
1.5x + 12X Zoom + 0.5x	50	0.43	5.23	0.028	0.151	6.17	1.12	2.65	5.85	0.64	0.02
1.5x + 12X Zoom + 0.67x	50	0.58	7.04	0.028	0.151	6.17	1.12	3.45	7.78	0.64	0.02
1.5x + 12X Zoom + 1.0x	50	0.87	10.50	0.028	0.151	6.17	1.12	5.18	11.60	0.64	0.02
1.5x + 12X Zoom + 1.33x	50	1.16	14.00	0.028	0.151	6.17	1.12	7.15	15.68	0.64	0.02
1.5x + 12X Zoom + 2.0x	50	1.74	21.00	0.028	0.151	6.17	1.12	10.74	23.34	0.64	0.02
1.5x + 12X Zoom + 3.5x	50	3.05	36.80	0.028	0.151	6.17	1.12	18.81	41.21	0.64	0.02
2.0x + 12X Zoom + 0.5x	32	0.58	6.98	0.038	0.202	4.50	0.83	2.61	5.79	0.35	0.01
2.0x + 12X Zoom + 0.67x	32	0.78	9.38	0.038	0.202	4.50	0.83	3.42	7.79	0.35	0.01
2.0x + 12X Zoom + 1.0x	32	1.16	14.00	0.038	0.202	4.50	0.83	5.09	11.62	0.35	0.01
2.0x + 12X Zoom + 1.33x	32	1.54	18.60	0.038	0.202	4.50	0.83	6.93	15.43	0.35	0.01
2.0x + 12X Zoom + 2.0x	32	2.32	28.00	0.038	0.202	4.50	0.83	10.17	23.24	0.35	0.01
2.0x + 12X Zoom + 3.5x	32	4.06	49.00	0.038	0.202	4.50	0.83	18.27	40.67	0.35	0.01

Assumptions:

1. *Minimum resolvable feature size is half of the threshold line pair limit. Calculation = 1/(3000 x Lens N.A.)*
2. *Matching pixel size is that which will permit the minimum feature size to overlap two pixels. Calculation = 1/2(Feature Size x System Magnification)*
3. *If the matching pixel size is greater than the camera pixel size, the system is "lens limited."*
4. *If the matching pixel size is less than the camera pixel size, the system is "camera limited."*

200 Commerce Drive, Rochester, New York 14623
Phone: 585-359-4000, Toll Free: 800-828-6778
Fax: 585-359-4999, http://navitar.com, info@navitar.com

Table B 1: Lens performance specification for 12X Zoom used in shadowgraphy provided by Navitar Inc

Appendix C

Computer code written by Maple program for the model of Ref. [5]

```
> restart;
> the_function := proc(L, rho_p, dp, P, n, m, Nef_D, dn, x, y, Q)

  # L = Nozzle length
  # rho_p = Particle density
  # dp = Particle diameter
  # P = Absolute Air Pressure
  # n = number of cell_inside the nozzle
  # m = number of cell_free jet
  # Nef_D = Nozzle's Design efficiency
  # dn = Nozzle diameter
  # x = Distance from the nozzle tip
  # y = distance from jet centre line
  # Q = Sphericity

  local T, R, k, Po, Cd, mp, Ap, rho_a, k_nef, Nef, r, Va, Vp,
  Vp0, Vpi, i, j, f, vis, Rp, F, ap, dVp, dt, ra, rp, theta_a,
  Va_x, Va_xy, y1, y2, theta_p, Vpj, Vp_r, Ls, Va_t, Vp_t, Xc;
      T := 298.15;          # temperature of the whole system.
  This model assumes isothermal flow.
      R := 287.05;          # gas constant of normal air, = ideal
  gas constant / molar mass of air.
      k := 1.4;             # Adiabatic exponent
      Po := 101325;         # Atmospheric pressure(kpa)
      vis := 1.8616e-5;     # viscosity of normal air at room
  temperature
      theta_a := 0.2434;        # between (12.5_15), based on the
  paper
      theta_p := 0.1217 ;        # Particle expansion angle, based
  on the paper
      Ap := pi*dp^2/4;
      rho_a := P/R/T;                         # Air Density at a
  given nozzle cross section
      k_nef := k/(k-Nef_D*(k-1));             # The modified
  adiabatic exponent
      r := (2/(k+1))^(k_nef/(k_nef-1));       # The modified
  critical pressure ratio
      Va := evalf(sqrt(2*Nef*k*P*(1-(Po/P)^((k-1)/k))/rho_a/(k-1))
  );  # Air flow Velocity (average value in the nozzle cross-
  section)
      Xc := 6.2*dn*1000;
```

```
if (Po/P) >= r
    then
    Nef := Nef_D;     # Nozzle efficiency factor
    Va := evalf(sqrt(2*Nef*k*P*(1-(Po/P)^((k-1)/k))/rho_a/(k-1))
);
    else
    Nef := (k-1)/(k+1)/(1-(Po/P)^((k-1)/k));    # Nozzle
efficiency factor
    Va := evalf(sqrt(2*Nef*k*P*(1-(Po/P)^((k-1)/k))/rho_a/(k-1))
);
 end if;

   Vp := 0 ; # Vp0 (initial guess)
 for i from 1 to n do
     #dt := L/n/Vp;
     mp := pi*dp^3*rho_p/6;
     Rp := dp*rho_a*(Va-Vp)/vis;     # Reynolds Particle Number

  # Cd := 42*(Rp^(-1)+0.018*Rp^(-0.37)+0.00035*Rp^(0.4));   #
Particle Drag coefficient for spherical particles

    Cd := (24/Rp)*(1+(8.1716*exp(-4.0655*Q))*Rp^(0.0964+0.5565*
Q))+(73.69*Rp*exp(-5.748*Q))/(Rp+5.378*exp(6.2122*Q)); #
Particle Drag coefficient with sphericity

     F := Cd*rho_a*(Va-Vp)^2*Pi*dp^2/8;
     ap := F/mp;
     Vp := sqrt(Vp^2+3*L*Cd*rho_a*((Va-Vp)^2)/2/n/dp/rho_p);

  end do;

ra := evalf(dn/2+x*tan(theta_a/2));
if x > 6.2*dn
     then
     Va_x := (Va)*6.2*dn/x;
     else
     Va_x := Va;
end if;

Va_xy := evalf(Va_x*exp(-ln(2)*(y/ra)^2));

#for y1 from -ra by (2*ra/10) to ra do
```

```
     Va_t := Va_x*exp(-ln(2)*(y1/ra)^2);
#end do;

Vpj := Vp ;        # particle velocity at the  free jet centre
line (y=0)
for j from 1 to m do
     Ls := x/m;
     if Va_x  > Vp
       then
       Vpj := sqrt(Vpj^2+1.5*Ls*Cd*rho_a*(Va_x-Vpj)^2/dp/rho_p);

       else
       Vpj := sqrt(Vpj^2-1.5*Ls*Cd*rho_a*(Va_x-Vpj)^2/dp/rho_p);
     end if;
end do;


rp := evalf(dn/2+x*tan(theta_p/2)*1000);
     Vp_r := evalf(Vpj*exp(-ln(2)*(y/rp)^2));

#for y2 from -rp by (2*rp/10) to rp do
     Vp_t := Vpj*exp(-ln(2)*(y2/rp)^2);
#end do;

    printf("Air velocity at exit is %a m/s\n", Va);
    printf("Particle velocity at nozzle exit point is %a m/s\n",
Vp);
    printf("Air velocity at xy position in free jet flow is %a
m/s\n", Va_xy);
    printf("Particle Velocity at the free jet centre line after
x mm from nozzle tip is %a m/s\n", Vpj);
    printf("Particle velocity at xy position in free jet flow
is %a m/s\n", Vp_r);
    printf("The air flow radius at an axial distance x is %a
m\n", ra);
    printf("The particle jet flow radius at an axial distance x
is %a mm\n", rp);
    plot(Vp_t(y2), y2=-rp..rp);


end proc;
```

(1)

```
the_function := proc(L, rho_p, dp, P, n, m, Nef_D, dn, x, y, Q)                                   (1)
    local T, R, k, Po, Cd, mp, Ap, rho_a, k_nef, Nef, r, Va, Vp, Vp0, Vpi, i, j, f, vis, Rp, F, ap,
    dVp, dt, ra, rp, theta_a, Va_x, Va_xy, y1, y2, theta_p, Vpj, Vp_r, Ls, Va_t, Vp_t, Xc;
    T := 298.15;
    R := 287.05;
    k := 1.4;
    Po := 101325;
    vis := 0.000018616;
    theta_a := 0.2434;
    theta_p := 0.2217;
    Ap := 1/4*π*dp^2;
    rho_a := P/(R*T);
    k_nef := k/(k − Nef_D*(k − 1));
    r := (2/(k+1))^(k_nef/(k_nef − 1));
    Va := evalf(sqrt(2*Nef*k*P*(1 − (Po/P)^((k − 1)/k))/(rho_a*(k − 1))));
    Xc := 6.2*dn*1000;
    if r <= Po/P then
        Nef := Nef_D;
        Va := evalf(sqrt(2*Nef*k*P*(1 − (Po/P)^((k − 1)/k))/(rho_a*(k − 1))))
    else
        Nef := (k − 1)/((k+1)*(1 − (Po/P)^((k − 1)/k)));
        Va := evalf(sqrt(2*Nef*k*P*(1 − (Po/P)^((k − 1)/k))/(rho_a*(k − 1))))
    end if;
    Vp := 0;
    for i to n do
        mp := 1/6*π*dp^3*rho_p;
        Rp := dp*rho_a*(Va − Vp)/vis;
        Cd := 24*(1 + 8.1716*exp(−4.0655*Q)*Rp^(0.0964 + 0.5565*Q))/Rp
         + 73.69*Rp*exp(−5.748*Q)/(Rp + 5.378*exp(6.2122*Q));
        F := 1/8*Cd*rho_a*(Va − Vp)^2*π*dp^2;
        ap := F/mp;
        Vp := sqrt(Vp^2 + 3/2*L*Cd*rho_a*(Va − Vp)^2/(n*dp*rho_p))
    end do;
    ra := evalf(1/2*dn + x*tan(1/2*theta_a));
    if 6.2*dn < x then Va_x := Va*6.2*dn/x else Va_x := Va end if;
    Va_xy := evalf(Va_x*exp(−ln(2)*y^2/ra^2));
    Va_t := Va_x*exp(−ln(2)*y1^2/ra^2);
    Vpj := Vp;
    for j to m do
        Ls := x/m;
        if Vp < Va_x then
```

```
            Vpj := sqrt(Vpj^2 + 1.5 * Ls * Cd * rho_a * (Va_x - Vpj)^2 / (dp * rho_p))
        else
            Vpj := sqrt(Vpj^2 - 1.5 * Ls * Cd * rho_a * (Va_x - Vpj)^2 / (dp * rho_p))
        end if
    end do;
    rp := evalf(1/2 * dn + 1000 * x * tan(1/2 * theta_p));
    Vp_r := evalf(Vpj * exp(-ln(2) * y^2 / rp^2));
    Vp_t := Vpj * exp(-ln(2) * y2^2 / rp^2);
    printf("Air velocity at exit is %a m/s\n", Va);
    printf("Particle velocity at nozzle exit point is %a m/s\n", Vp);
    printf("Air velocity at xy position in free jet flow is %a m/s\n", Va_xy);
    printf("Particle Velocity at the free jet centre line after x mm from nozzle tip is %a m/s\n",
    Vpj);
    printf("Particle velocity at xy position in free jet flow is %a m/s\n", Vp_r);
    printf("The air flow radius at an axial distance x is %a m\n", ra);
    printf("The particle jet flow radius at an axial distance x is %a mm\n", rp);
    plot(Vp_t(y2), y2 = -rp..rp)
end proc
```

```
> # the_function := proc(L, rho_p, dp, P, n, m, Nef_D, dn, x, y,
  Q)
  # L = Nozzle length
  # rho_p = Particle density
  # dp = Particle diameter
  # P = Absolute Air Pressure
  # n = number of cell_inside the nozzle
  # m = number of cell_free jet
  # Nef_D = Nozzle's Design efficiency[21]
  # dn = Nozzle diameter
  # x = Distance from the nozzle tip
  # y = distance from jet centre line


  the_function(0.01, 3800, 25e-6, 300e3+101325 ,100, 100, 0.8,
  0.76e-3, 0.02, 0.002, 0.76); # 25um Al2o3 at 300 kpa after 20mm
```

```
Air velocity at exit is 315.9872631 m/s
Particle velocity at nozzle exit point is 198.1899310 m/s
Air velocity at xy position in free jet flow is 52.61149262 m/s
```

```
Particle Velocity at the free jet centre line after x mm from
nozzle tip is 157.9397558 m/s
Particle velocity at xy position in free jet flow is 157.9396675
m/s
The air flow radius at an axial distance x is .2826088188e-2 m
The particle jet flow radius at an axial distance x is
2.226505482 mm
```

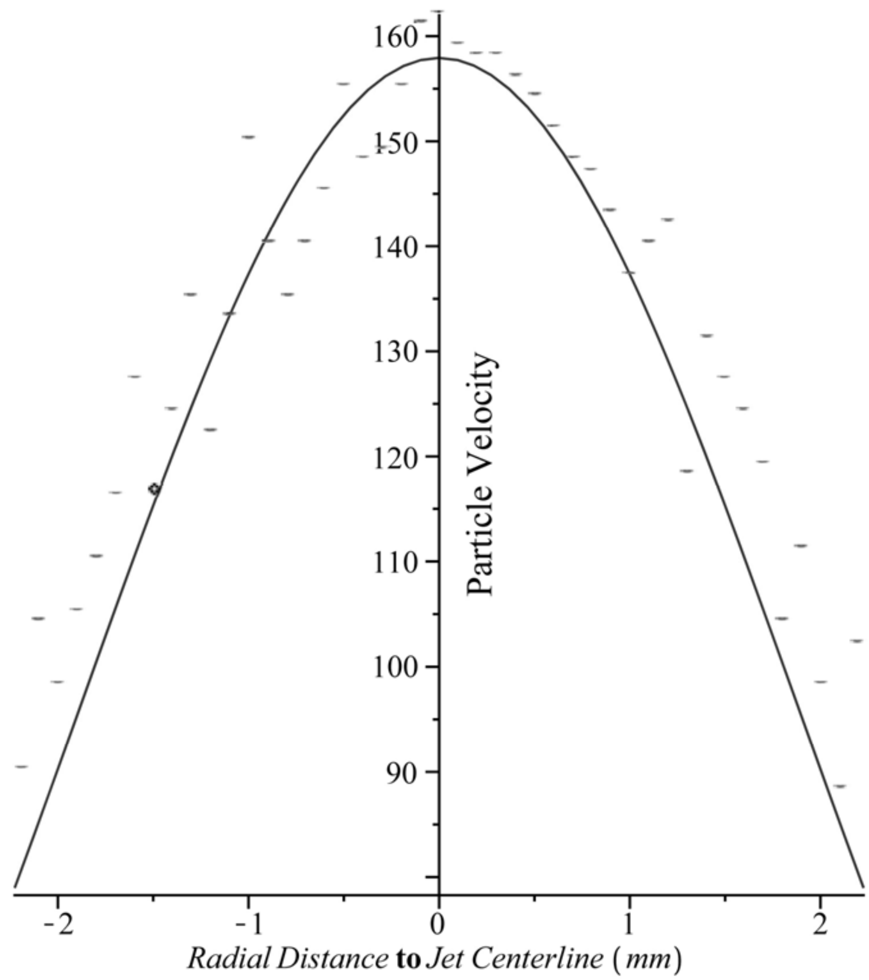

References

[1] J.H.M. ten Thije Boonkkamp, J.K.M. Jansen, An analytical solution for mechanical etching of glass by powder blasting, J. Eng. Math. 43 (2002) 385–399

[2] P. J. Slikkerveer and F. H. in't Veld, Model for patterned erosion. *Wear* 233 (1999) 377-386

[3] A. Ghobeity, T. Krajac, T. Burzynski, M. Papini, J.K. Spelt, Surface evolution models in abrasive jet micromachining, Wear 264 (2008) 185–198

[4] H. Getu a, A. Ghobeity, J.K. Spelt, M. Papini, Abrasive jet micromachining of acrylic and polycarbonate polymers at oblique angles of attack, Wear 265 (2008) 888–901

[5] H.Z. Li, J. Wang, J.M. Fan, Analysis and modeling of particle velocities in micro-abrasive air jet, International Journal of Machine Tools & Manufacture 49 (2009) 850–858

[6] A. Ghobeity, D. Ciampini, M. Papini, An analytical model of the effect of particle size distribution on the surface profile evolution in abrasive jet micromachining, Journal of Materials Processing Technology, v 209, n 20, (2009) 6067-6077

[7] M. Dundar , O.T. Inal, J. Stringer, The effect of particle size on the erosion of a ductile material at the low particle size limit, Wear 233–235 (1999) 727–736

[8] A. B. Prochaska, P. M. Santi, D. Higgins, Relationships between size and velocity for particle within debris flows, Canadian Geotechnical Journal 45 (2008) 1778-1783

[9] I. Hutchings and R. Winter, Particle Erosion of Ductile Metals: A Mechanism of Material Removal, Wear 27, (1974) 121-128

[10] M. Liebhard and A. Levy, The effect of erodent particle characteristics on the erosion of metals, Wear 151 (1991) 381-390

[11] R. Clift, J. R. Grace and M. E. Weber, Bubbles, Drops and Particles, Academic Press, New York, (1978)

[12] A. R. Khan and J. F. Richardson, The resistance to motion of a solid sphere in a fluid, Chemical Engineering Communications 62 (1987) 135-150

[13] A. M. Haider, M.S. Project, Oregon State University (1987)

[14] Haider and O. Levenspiel, Drag Coefficient and Terminal Velocity of Spherical and Nonspherical Particles, Powder Technology 58 (1989) 63-70

[15] A. W. Ruff, Analysis of interlaboratory test results of solid particle impingement erosion, Wear 108 (1986) 323-335

[16] Conducting Erosion Test by Solid Particle Impingement Using Gas Jets, ASTM Stand. G-76, 1983 (ASTM, Philadelphia, PA)

[17] L. Lapides and A. Levy, The halo effect in jet impingement solid particle erosion testing of ductile metals, Wear 58 (1980) 301-311

[18] P.H. Shipway, I.M. Hutchings, Influence of nozzle roughness on conditions in a gas blast erosion rig, Wear 162–164 (1993) 148–158.

[19] D. Ciampini, J.K. Spelt, M. Papini, Simulation of interference effects in particle streams following impact with a flat surface, Part I. Theory and analysis, Wear 254 (2003) 237-249

[20] D. Ciampini and M. Papini, A cellular automata and particle-tracking simulation of abrasive jet micromachining that accounts for particle spatial hindering and second strikes, Journal of Micromechanics and Microengineering 20 (2010) 1-16

[21] C.M. Preece, N.H. Macmillan, Ed. R.A. Huggins, Erosion, Annual Review of Materials Science 7 (1977)

[22] R. Balasubramaniam, J. Krishnan, N. Ramakrishnan, A study on the shape of the surface generated by abrasive jet machining, Journal of Materials Processing Technology 121 (2002) 102-106

[23] A.N.J Stevenson, I.M. Hutchings, Scaling laws for particle velocity in gas-blast erosion test, Wear 181-183 (1995) 56-62

[24] A.W. Ruff and L. K. Ives, Measurement of solid particle velocity in erosive wear, Wear 35 (1975) 195-199

[25] T. H. Kosel and K. Anand, An optoelectronic erodent particle velocimeter, in V. Srinivasan and K. Vedula (ads.), Corrosion and Particle Erosion at High Temperature, The Minerals, Metals and Materials Society (1989) 349-368

[26] T. Burzynski and M. Papini, Measurement of the particle spatial and velocity distributions in micro-abrasive jets, Measurement Science and Technology 22 (2011) 025104

[27] M. Achtsnick, P.F. Geelhoed, A.M. Hoogstrate, B. Karpuschewski, Modelling and evaluation of the micro abrasive blasting process, Wear 259 (2005) 84-94

[28] A. Ghobeity, M. Papini, J.K. Spelt, Computer simulation of particle interference in abrasive jet micromachining, Wear 263 (2007) 265–269

[29] T. Burzynski and M. Papini, Level set methods for the modelling of surface evolution in the abrasive jet micromachining of features used in MEMS and microfluidic devices, Journal of Microelectronics and Microengineering 20 (2010) 085004

[30] H. Yagyu and O. Tabata, Three-dimensional simulation of powder blasting with a polymer mask using a cellular automaton, Journal of Micromechanics and Microengineering 18 (2008) 055010

[31] K. Inaba and K. Matsumoto, The development of the measurement of particle concentration using a commercial laser diffraction particle size analyzer, Advanced Powder Technology (1999) 89-103

[32] P. Kippax, Appraisal of the Laser Diffraction Particle-Sizing Technique, Pharmaceutical Technology 29 (2005)

[33] R. Goldman, Advanced Imaging Technologies, Clemex Technologies Longueuil, Quebec, Advanced Materials & Processes magazine (2004)

[34] J. Czarske, Laser-Doppler velocity profile sensor using a chromatic coding, Measurement Science and Technology 12 (2001) 52–57

[35] J. Czarske, L. Büttner and T. Razik, Boundary layer velocity measurements by a laser-Doppler profile sensor with micrometer spatial resolution, Measurement Science and Technology 13 (2002) 1979–1989

[36] L. Büttner and J. Czarske, A multimode-fibre laser-Doppler anemometer for highly spatially resolved velocity measurements using low-coherence, light Measurement Science and Technology 12 (2001) 1891–1903

[37] L. Büttner and J. Czarske, Spatial resolving laser-Doppler velocity profile sensor using slightly tilted fringe systems and phase evaluation, Measurement Science and Technology 14 (2003) 2111–2120

[38] T. Pfister, L. Büttner and J. Czarske, Laser-Doppler profile sensor with sub-micrometre position resolution for velocity and absolute radius measurements of rotating objects, Measurement Science and Technology 16 (2005) 627–641

[39] K. Shirai, T. Pfister, L. Büttner, J. Czarske, H. Müller, S. Becker, H. Lienhart and F. Durst, Highly spatially resolved velocity measurements of a turbulent channel flow by a fiber-optic heterodyne laser-Doppler velocity-profile sensor Exp. Fluids 40 (2006) 473–81

[40] K. T. Lowe and R. L. Simpson, An advanced laser-Doppler velocimeter for full-vector particle position and velocity measurements, Measurement Science and Technology 20 (2009) 045402

[41] S. W. Lee and Y. Liu, The unique phase Doppler particle analyzer application and analysis of solid particle flow in fluidized bed combustor (FBC) cold model, Particulate Science and Technology 22 (2004) 65-73

[42] A. P. Verma and G. K. Lai, A theoretical study of erosion phenomenon in abrasive jet machining, Journal of Manufacturing Science and Engineering (1996) 564–570

[43] C. D. Meinhart, S. T. Wereley, and M. H. B. Gray, Volume illumination for two dimensional particle image velocimetry, Measurement Science and Technology 11 (2000) 809-814

[44] K. Ohmi and H. Y. Li, Particle-tracking velocimetry with new algorithms, Measurement Science and Technology 11 (2000) 603–616

[45] M. J. Sathe, H. Thaker, T. E. Strand, B. Joshi, Advanced PIV/LIF and shadowgraphy system to visualize flow structure in two-phase bubbly flows, Chemical Engineering Science 65 (2010) 2431-2442

[46] Sizing Master Shadow, product manual for Davis 7.2, 2007. http://www.lavision.de/download/manuals/index.php

[47] M. Liebhard and A. Levy, The effect of erodent particle characteristics on the erosion of metals, Wear 151 (1991) 381- 390

[48] I. Finnie and D. H. McFadden, On the velocity dependence of the erosion of ductile metals by solid particles at low angles of incidence, Wear 48 (1978) 181–190

[49] A. J. Ninham and I. M. Hutchings, A computer model for velocity calculation in erosion testing, University of Cambridge, Cavendish Lab (1983) 1-50

[50] H. Wadell, Volume Shape and Roundness of Quartz Particles, Journal of Geology 43 (1935) 250–280

[51] B. R. Jennings and K. Parslow, Particle size measurement: the equivalent spherical diameter, Royal Society of London. Series A, Mathematical and Physical Sciences 419 (1988) 137-149